Doctoral Dissertation

Formation of spatial perturbation on diamond foils due to nonuniform laser irradiation on direct-drive inertial confinement fusion

慣性核融合における非一様レーザー照射による ダイヤモンド表面擾乱の形成

Hiroki KATO

Graduate School of Science, Department of Physics
Osaka University

Supervisor: Professor Shinsuke Fujioka

December 2018

Abstract

This dissertation presents a comprehensive study on generation of surface perturbations by non-uniform laser irradiation which degrades stable compression of inertial confinement fusion (ICF) capsules. Also, the results on development of the ICF target capsules with diamond are shown in this dissertation. These studies were conducted at Osaka University Graduate School, Graduate School of Science and Doctor's Course.

ICF is a method of initiating nuclear fusion reaction by fuel implosion using energy driver. It is expected as a new energy source in electric power plants. A capsule containing fusion fuels is compressed and heated by intense laser beams ($\leq 10^{15}\,\mathrm{W/cm^2}$). When a hot ($\sim$ 50 million degrees) and dense ($\sim$ 1000 times the solid density) plasma is realized by this method (direct-drive ICF), explosive nuclear fusion reaction becomes possible within a short time of 10-100 ps. This reaction requires highly symmetric implosion of the target capsule. However, actually, laser imprinting occurs on the capsule surface due to irradiation non-uniformity. Spatial perturbation due to laser imprinting is amplified by the Rayleigh-Taylor instability during the shell acceleration. The grown perturbation could disrupt the shell and cause mixing of fuel. Laser imprinting is one of factors preventing the compression and heating of the fuel. Therefore, suppressing imprint perturbation even under nonuniform laser irradiation is the important subject for direct-drive ICF.

To date, it has been demonstrated that laser imprinting is mitigated by the diffusive thermal conduction of the laser produced plasma on the material surface. On the other hand, this thermal smoothing effect has a disadvantage that formation of laser-produced plasma is insufficient at the initial stage of irradiation and it is not effective for smoothing nonuniformity.

In this study, in order to elucidate the imprinting mitigation mechanism, comprehensive study of how the equation of state affects laser imprinting of an inertial fusion target was conducted. It has been suggested that a stiffer and denser material would reduce laser imprinting based on the equation of motion with plasma pressure perturbation (or irradiation nonuniformity). Therefore, while the conventional material of ICF capsule is polystyrene, author investigated the detailed temporal evolution of the imprint perturbation in the diamond foil which is a candidate of the stiff-ablator material by using radiation hydrodynamic simulation. The simulated perturbation is compared with experimental measurements of areal-density perturbations obtained by using x-ray shadowgraphy for diamond and polystyrene. The experimental results are well reproduced by the results of the radiation hydrodynamic simulations, which indicate that the imprinting amplitude due to nonuniform irradiation (nonuniformity=intensity perturbation/average intensity $\sim$10%, average intensity, 4.0×10^{12} to $5.0 \times 10^{13}\,\mathrm{W/cm^2}$) differs by a factor of two to three between diamond and polystyrene. It was demonstrated for the first time that the material density and compressibility during laser irradiation

relate to the imprinting mitigation.

On the other hand, experiments have suggested that influence of solid strength including local fracture is induced to the diamond foils by large irradiation nonuniformity, which do not be reproduced by the two-dimensional radiation hydrodynamic simulation. The experimental and simulation results suggest that the large irradiation nonuniformity (or pressure perturbation) partially exceed the elastic limit of dynamic stress and this structure affects the perturbation. Irradiation conditions under which solid strength becomes issues were found.

As mentioned above, diamond capsule is considered to be a candidate as a direct-drive ICF targets because material stiffness is the effective parameter for mitigation of laser imprinting. Furthermore, in order to realize ICF, highly precise capsules with film thickness uniformity at the nano order level are required. Therefore, author carried out synthesis and development of diamond capsules (diameter about $500\,\text{or}\,2000\,\mu\text{m}$, film thickness $\leq 10\,\mu\text{m}$) by using chemical vapor deposition (CVD) method through collaborative research with National Institute of Advanced Industrial Science and Technology (AIST) and Institute of Laser Engineering, Osaka University. In the synthesis experiments, high precision diamond capsules with sphericity $\sim$99.7 % and the surface smoothness of several tens nanometer or less were obtained without mechanical-polishing. Consequently, the author confirms experimentally and numerically that diamond is superior to conventional material (polystyrene) as a direct-drive ICF capsule material, and shows that spherical diamond foils can be fabricated by the method which can expect mass production of capsules.

This dissertation consists of seven chapters. Chapter 1 introduces the scenario and some important issues on direct-drive ICF. In particular, it is pointed out that laser imprinting and hydrodynamic instability are important issues in the direct-drive scheme. The Chapter 2 shows a model of laser imprinting. It is described that material stiffness and density are important parameters to mitigate the laser imprinting by nonuniform irradiation. Chapter 3 explains equation of state in the radiation hydrodynamic simulation code for comparison with the experimental studies of laser imprinting. Equation of state is related to material stiffness (compressibility) and density. Chapter 4 shows the experimental and simulation studies of laser imprinting with diamond foils. The perturbation generated by irradiation nonuniformity was observed by amplifying its perturbation with hydrodynamic instability growth. The areal-density perturbations for single-crystal diamond and polystyrene foils were measured. Experimental results are compared with numerical calculations. The effects of material stiffness and density on laser imprinting are quantitatively evaluated. In Chapter 5, in addition, perturbation structure on diamond foils due to laser irradiation nonuniformity has been investigated and the solid strength issues in non-uniform irradiation is discussed. Chapter 6 describes the fabrication and development of diamond capsules for ICF targets using a chemical vapor deposition method. Chapter 7 is devoted to conclude this study with the summary of the obtained results.

Acknowledgments

Special thanks are due to my dissertation supervisor Professor Keisuke Shigemori and Professor Shinsuke Fujioka for their invaluable support and guidance through the hard moments of graduate school. I am also grateful to my dissertation committee: Professor Shinsuke Fujioka, Professor Keisuke Shigemori, Professor Mitsuo Nakai, Professor Yasuhiko Sentoku, Professor Tadashi Kondo, and Professor Setsuko Tajima for their support, valuable feedback, and insightful ideas to this research.

I would like to thank Associate Professor Hideo Nagatomo for teaching the skills of radiation hydrodynamic simulation and thank you for much discussion about the experiment data. Special thanks are due to Assistant Professor Tatsuhiro Sakaiya for teaching the know-how of X-ray measurements in this research. I would like to thank Associate Professor Hidenori Terasaki, Researcher Yoichirou Hironaka, Researcher Kohei Miyanishi for discussing and supporting the experiments of this research. I would like to thank Ms. Hosokawa and Mr. Nagata who prepared highly accurate experimantal targets in the GEKKO- XII Nd: glass laser facility at the Institute of Laser Engineering, Osaka University. I would like to thank Mr. Maekawa and Mr. Kubota for supporting the experiments of this research. Special thanks are due to National Institute of Advanced Industrial Science and Technology (AIST)'s Dr.Hideaki Yamada, Dr.Shinya Ohmagari, Dr.Akiyoshi Chayahara, Dr.Yoshiaki Mokuno, and Dr.Daisuke Takeuchi for teaching diamond synthesis techniques and know-how on the fabrication of diamond foils and thanks for doing a lot of discussions in this research.

This work was performed under a joint research project of the Institute of Laser Engineering, Osaka University. This work was also performed with the support and under the auspices of the NIFS Collaboration Research program (NIFS10KUGK044). The authors would like to acknowledge the dedicated technical support of the staff at the GEKKOXII facility for laser operation, target fabrication, and plasma diagnostics. This work was partly supported by the Japan Society for Promotion of Science, KAKENHI Grant No. 23340175.

This study was carried out by collaborative investigation with AIST and Institute of Laser Engineering, Osaka University.

Contents

List of Figures

List of Tables

Chapter 1

Introduction

1.1 Principle of laser fusion

A nuclear reaction in which the total mass of the final products $\sum_f m_f$ is smaller than that of the reacting nuclei $\sum_i m_i$ is exothermic, that is, releases an energy $(\sum_i m_i - \sum_f m_f)c^2$ proportional to such a mass difference Δm. Here the symbol m denotes mass, the subscripts i and f indicate, respectively, the initial and the final products, and c is the speed of light. The mass difference Δm between the final products and reacting nuclei has to provide an amount of energy equal to the difference between the final and initial binding energy in order to dissociate the nucleus into its component neutrons and protons. Exothermic reaction occurs for fission reactions, in which a heavy nucleus is split into lighter fragments, and for fusion reactions, in which two light nuclei merge to form a heavier nucleus. The reaction rate, that is, the number of reactions per unit time and per unit volume, is proportional to the square of nucleus density [1], indicating the role of the density of the fuel in achieving efficient release of fusion energy.

The largest fusion cross-section occurs for the deuterium-tritium reaction [D + T $\rightarrow$ n (14.1 MeV) + ^{4}He (3.5 MeV)], requiring temperatures of the order of several tens of million degrees or keV to overcome the Coulomb barrier between the fusing nuclei (Fig. 1.1). The collision cross section corresponds to the probability that the incident particle collides with the target particle. At a collision with energies of 5$-$300 keV, it has a cross section σ_{DT} of about $10^{-3}-5$ barn (1barn=10^{-28} m^2) and releases an energy of $Q_{\mathrm{DT}} = 17.6\,\mathrm{MeV}$ [1, 2]. Another

important quantity for nuclear reaction is the reactivity, defined as the probability of reaction per unit time per unit number density of target nuclei. The average reactivity is obtained by the collision cross section and the velocity distribution of the relative velocity between particles (Boltzmann distribution). As shown in Fig. 1.2, the deuterium-tritium reaction has by far the largest reactivity $< \sigma v >$ [2]. When the particle number density of ions for deuterium and tritium are n_{D} and n_{T} respectively, the reaction rate per unit volume and per unit time is expressed by reaction rate $= n_{\mathrm{D}} n_{\mathrm{T}} < \sigma v >$ [$\mathrm{cm}^{-3}\mathrm{s}^{-1}$], relate to the reactivity and total nuclei number densities. Deuterium is provided from water (37g of D per 1000 kg of water). Tritium is bred from Lithium by DT fusion neutrons ($^6\mathrm{Li} + \mathrm{n} \rightarrow \mathrm{T} + \alpha + 4.86\,\mathrm{MeV}$ or $^7\mathrm{Li} + \mathrm{n} \rightarrow \mathrm{T} + \alpha - 2.87\,\mathrm{MeV}$). Tritium of about 10^{11} t exists in the oceans. Primary fuel (deuterium and litium) is practically inexhaustible, well distributed on earth, at low cost.

The TT reaction (T + T $\rightarrow$ α + 2n + 11.3 MeV) is also important for the controlled fusion research. Due to atomic number=1, reactions between the hydrogen isotopes, deuterium and tritium, have relatively large tunnel penetrability. In advanced fusion fuels, the D^{3}He reaction (D + ^{3}He $\rightarrow$ α + p + 18.35 MeV) does not involve radioactive fuel and does not release neutrons, but a D^{3}He fuel would anyhow produce tritium and emit neutrons due to unavoidable DD reactions (D + D $\rightarrow$ T + p + 4.04 MeV, D + D $\rightarrow$ ^{3}He + n + 3.27 MeV)).

The method being advanced in nuclear fusion study with the goal of realizing nuclear fusion as an energy source is to generate high temperature ionized gas composed of nuclei of D and T (D-T plasma), and to sustain the nuclear fusion reaction by utilizing the collision caused by the thermal motion of the nuclei. For example, once D and T having an energy of 10 keV react, energy (17.58 MeV) of 1800 times as high as 10 keV is obtained. If we can increase the number of nuclear fusion reactions, then we could have a practical energy source. It is necessary for the practicality of energy source to maintain the temperature of the plasma at 10 keV or more to facilitate realization of the nuclear fusion reaction and maintain the density value for a certain period of time to increase the number of nuclear fusion reactions. The plasma inertia confines the plasma pressure long enough for the

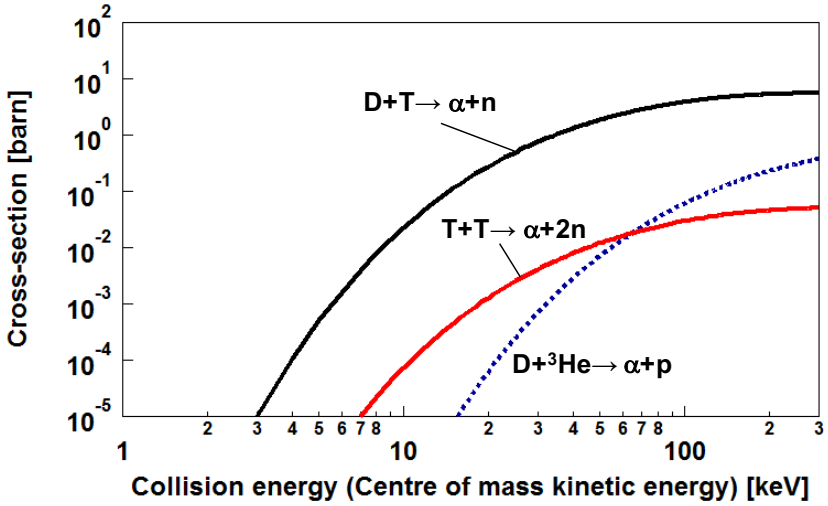

Figure 1.1: Fusion cross sections versus collision energy for reactions of interest to controlled fusion energy.

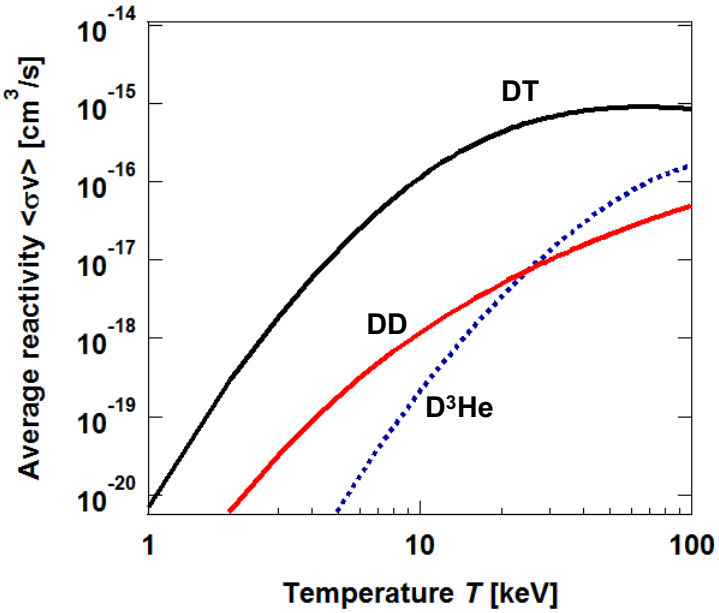

Figure 1.2: Reactivity as a function of the temperature for the reactions of interest to controlled fusion.

thermonuclear burn to produce copious amounts of fusion reactions in a process known as inertial confinement fusion (ICF). Inertial confinement fusion (ICF) is distinguished from magnetic confinement fusion (MCF [3]) in that the fusion fuel is compressed and maintained (briefly) at fusion densities and temperatures by its own inertia. There are two approaches to laser-driven ICF: direct drive, in which a spherical target containing fusion fuel is directly irradiated by laser beams [4], and indirect drive, in which the laser beams heat the inside of a typically cylindrical container known as a hohlraum, producing x rays that irradiate a spherical fuel-containing capsule [5, 6].

In nuclear fusion reactor, the fusion energy will be released, compensating for the energy losses due to emission of radiation and to thermal conduction and convection. In order for energy from nuclear fusion to exceed plasma heating or radiation loss, conditions in plasma density n and confinement time τ are imposed. The minimum value $n\tau$ of the required condition is about $10^{14}\,\mathrm{cm}^{-3}$s for the DT reaction and about $10^{16}\,\mathrm{cm}^{-3}$s for the DD reaction [1]. This required condition is called "Lawson creterion". In the MCF, it is required to hold the plasma for several seconds at the plasma density of about $10^{14}\,\mathrm{cm}^{-3}$. In laser-driven ICF, it is necessary to confine high density plasma of $10^{26}\,\mathrm{cm}^{-3}$ for about 10^{-12} s. This study is concerned solely with direct-drive ICF.

The concept of a direct-drive ICF are sketched in Fig. 1.3. The target capsule for ICF experiments consists of a cryogenic layer of deuterium and tritium (DT) frozen onto the inner surface of a spherical shell of ablator material. The interior of the DT ice layer contains low-density DT gas in thermal equilibrium with the ice. The density ρ_v of the DT gas, in pressure equilibrium with the cryogenic DT layer, is controlled by regulating the target temperature T_0. The value $\rho_\mathrm{v} = 0.3\,\mathrm{mg/cm}^3$ of DT gas density is achieved by keeping the target at $T_0 \approx 17.9\,\mathrm{K}$. The density ρ_DT for DT ice is about 0.2 g/cm^3. Typical ignition and high-gain target capsules for an fusion reactor have diameters from 3 to 5 mm and ice layer thicknesses from 160 to 600 μm. In direct-drive ICF, a fuel capsule is irradiated directly with intense laser light. The laser light is absorbed by the target, leading to the ablation of target material (at the “ablation surface”) to form a hot ablated

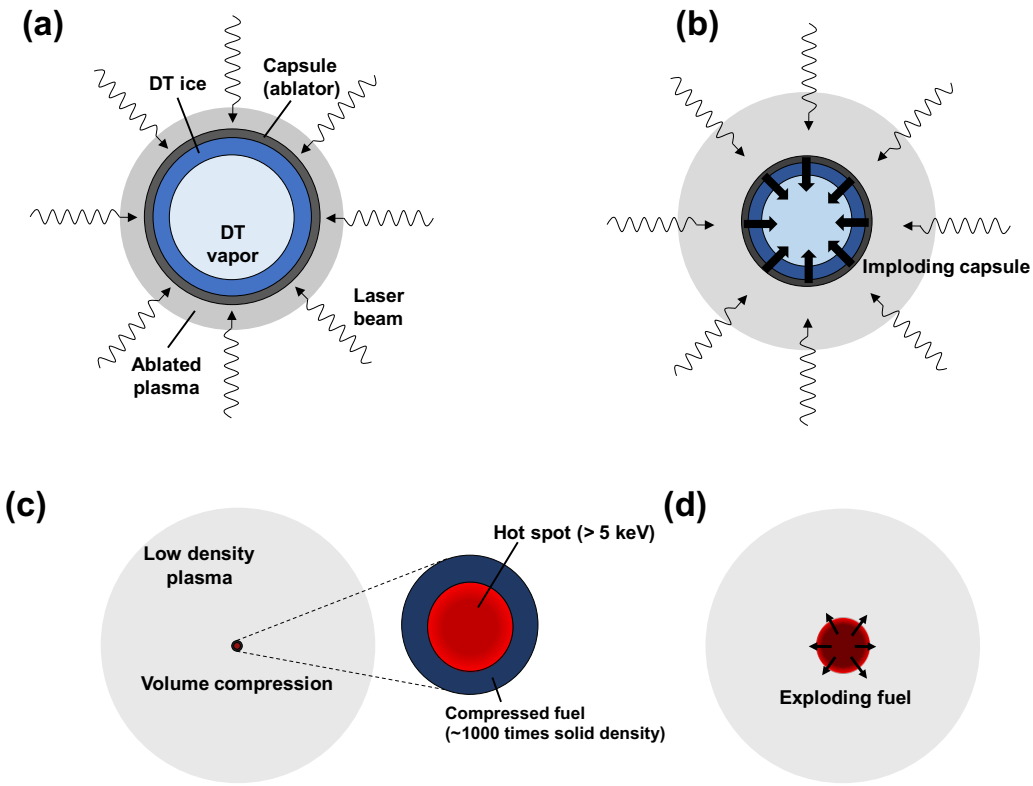

Figure 1.3: Principle of inertial confinement fusion by spherical implosion. (a) Irradiation on fuel capsule. (b) Implosion driven by ablation plasma. (c) Central ignition. (d) Burn propagation.

plasma (Fig. 1.3(a)). The plasma pressure on the surface drives the fuel implosion (Fig. 1.3(b)). As the imploding capsule stagnates in the centre its kinetic energy is converted into thermal energy. At this time (Fig. 1.3(c)), the fuel consists of a highly compressed shell enclosing a hot spot of igniting fuel in the centre. In these targets, the first fusion reactions occur in a central "hot spot"-a high-temperature, low-density region surrounded by a lower-temperature, higher-density DT shell. It is critical that the hot spot has sufficient energy production and areal density ρR (where ρ is the density and R is the radius) for significant alpha-particle energy deposition to occur in the hot spot.

For ICF, it is common to use the product of plasma density ρ and capsule radius R instead of nt. The time $t_{\rm d}$ until the spherical fuel of radius R thermally expands can be expressed as $t_{\rm d}$=$\alpha R/c_{\rm s}$. Here $c_{\rm s} = \sqrt{k_\beta T/m_{\rm i}}$ is the sound speed and α is a positive constant less than 1 and is a parameter characterizing the magnitude. This is the time when the burn wave propagates only around 1/4 of the radius from the periphery of the fuel sphere. This takes into consideration that about 50% of the total mass is included in the spherical shell of 1/5 the radius. The number density n of ions in the unit volume is ρ/m_i, therefore the Lawson parameter nt is

$$nt \approx \frac{\rho}{m_i}\frac{\alpha R}{c_s}. \tag{1.1}$$

Assigning the numerical values $nt = 10^{14}$ cm^{-3}s, $k_\beta T = 20$ keV, $m_i = 2.5 \times 1.67 \times 10^{-24}$g for the DT reaction into the mathematical expression leads to ρR = 0.2 g/cm^2. At 4.2 keV fusion alpha particle power exceeds bremsstrahlung power [1]. Therefore, even for deuterium-tritium the temperature must exceed 5 keV. The hot spot needs to self-heat for fuel burn propagation as in Fig. 1.3(d). In an ignited DT plasma, a fraction of the energy associated with the α-particles (3.5 MeV) from the DT reactions is deposited in the plasma itself, thereby increasing its temperature and, in turn, the fusion reaction rate. The hot spot temperature or internal energy rise when the power density $W_{\rm dep}$ deposited within the hot spot by fusion products must exceed the sum of all power losses (contribution due to

mechanical work W_{m}, power density loss by radiation W_{m}, and power density loss by thermal conduction W_{e}). That is, the self heating condition is expressed as $W_{\mathrm{dep}} > W_{\mathrm{e}} + W_{\mathrm{r}} + W_{\mathrm{m}}$. When the self-heating occurs sufficiently, the surrounding main fuel also becomes high temperature and nuclear fusion reactions are caused in a chain reaction by burn propagation (Fig. 1.3(d)). This is called "ignition". From Refs. [5] and [6], this typically requires an ion temperature of 10 keV and $\rho R \approx 0.3$ g/cm^2, although the ion temperature of 5 keV at the onset of ignition with a larger ρR is considered to be more realistic. Typical ICF ignition designs use a maximum implosion velocity in the range of 3.5-4.0 $\times$ 10^7 cm/s, corresponding to an ion temperature of 4 to 5 keV [11]. Another concern at maximum compression stage is mixing between the hot fuel in the core and the cooler shell material, reducing the temperature of the hot fuel (as described following Section). The controlled fusion requires the achievement of such extreme conditions.

1.2 Important phenomena for direct-drive inertial confinement fusion

Heren, taking laser implosion diagram as shown in Fig. 1.4, chasing the scenario of implosion with time, explain the physics in each process. The structure of the outer and inner surfaces of the target shell during laser implosion is also shown in Fig. 1.5. At early phase [Fig. 1.4(1)], an intense laser light is absorbed by multi-photon absorption at the target surface, leading to the ablation of target material (at the "ablation surface") to form a plasma. Electrons accelerated by the electric field of laser light collide with atoms and ions to form high temperature plasma. The electrons are heated by such classical absorption (inverse bremsstrahlung). The laser-heated electron carries energy to the ablation surface by heat conduction and maintains ablation. The ablation pressure generated in the plasma launch the shock waves that propagate into the target. The spatial perturbations occurs on the ablation surface due to spatial intensity nonunifor-

mity of the laser beam, which is called laser imprinting (see Fig. 1.5(a)). During this shock-transit stage [Fig. 1.4(2)], target perturbations (imperfections in fabrication or shell-inner perturbations by laser-beam non-uniformities) evolve as a result of a Richtmyer-Meshkov (RM) instability [7, 8]. The classical RM instability involves the interaction of a planar shock with a perturbed interface between two fluids. The transmitted shock and reflected shock (or reflected rarefaction) created after that interaction becomes distorted, producing a pressure perturbation in the shocked region. After the shock reaches the inner surface of a target shell, a rarefaction wave moves outward toward the ablation surface. The ablator and ice layer (collectively known as the shell) begin to accelerate inward toward the target center. Important issues during this initial stage include the development of ablation-surface perturbations as a result of laser imprint, the feedout of inner-surface perturbations carried by the rarefaction wave to the ablation surface, and laser-plasma interactions in the coronal plasma. Laser-plasma interactions can have undesirable effects including the production of energetic electrons (also known as fast, hot, or suprathermal electrons), leading to fuel preheat. X rays from the hot plasma surrounding the target can also lead to preheat.

The laser intensity increases during the acceleration phase. Ablation-surface perturbations grow exponentially because of the Rayleigh-taylor (RT) instability [Fig. 1.5(b)], while the main shock within the DT gas converges toward the target center (Fig. 1.4(3)). Exponential growth continues until the perturbation amplitude reaches 10% of the perturbation wavelength, when the instability growth becomes nonlinear [9]. The greatest concern during the acceleration phase is the integrity of the shell. The ablation-surface perturbations grow at a rate that depends in part on the shell adiabat a, defined as the electron pressure divided by the Fermi-degenerate pressure that the shell would have at absolute zero temperature. Larger adiabats result in thicker, lower-density imploding shells, larger ablation velocities, and better overall stability, but at the cost of lower overall performance. (The ablation velocity is the rate at which the ablation surface moves through the shell.)

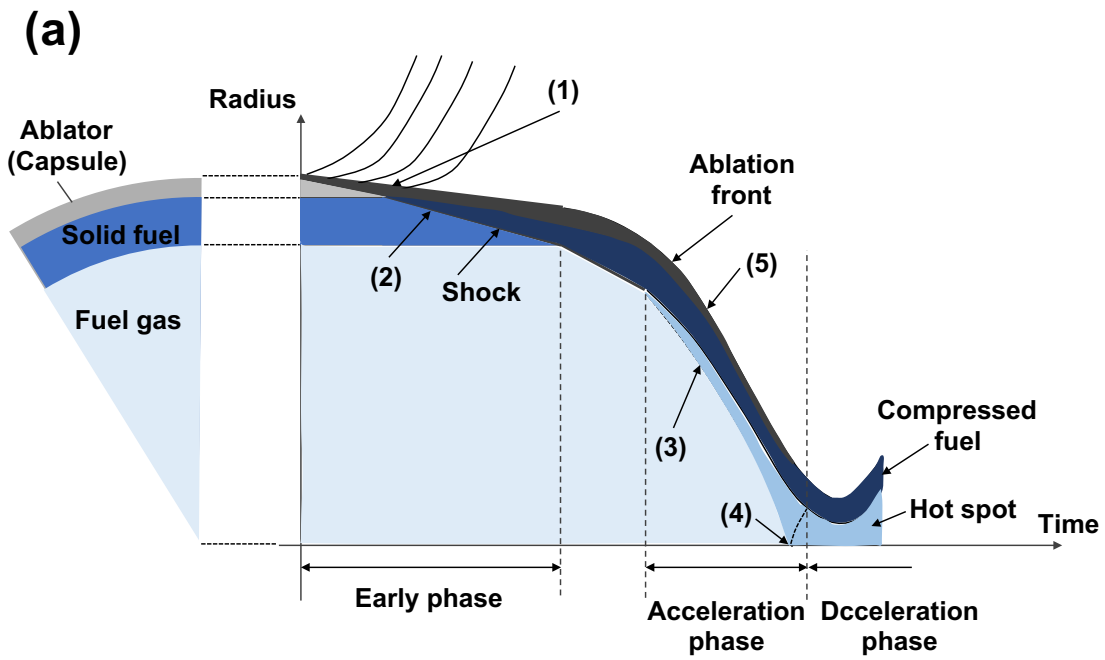

Figure 1.4: Implosion diagram of the capsule.

The strong shock by ablation pressure moves ahead of the accelerating shell and is reflected at the target center (Fig. 1.4(4)). When the reflected shock wave reaches the converging shell again, the target shell is decelerated. The stage from the start of this deceleration is called the deceleration phase. As the shell decelerates, its kinetic energy is converted into thermal energy and then the DT gas is heated. The shell compression depends on the temperature of the DT at the start of the deceleration phase, and the maximum temperature depends on the kinetic energy of the shell. In deceleration phase, hot spot and a high density main fuel region are formed, self heating occurs in the hot spot, and the detonation wave propagates through the main fuel part. The most significant issue during the deceleration phase is the hydrodynamic instability of the inner surface of the shell. The deceleration instability is seeded by the feedthrough [1] of ablation-surface perturbations to the inner surface combined with the original inner-surface perturbations. Perturbation of the inner surface of the target shell grows due to RT instability, because acceleration gravity acts from high density plasma towards low density plasma (Fig. 1.5(c)). Another concern at this phase is mixing between the hot spot fuel in the core and the cooler shell, reducing the temperature of the hot

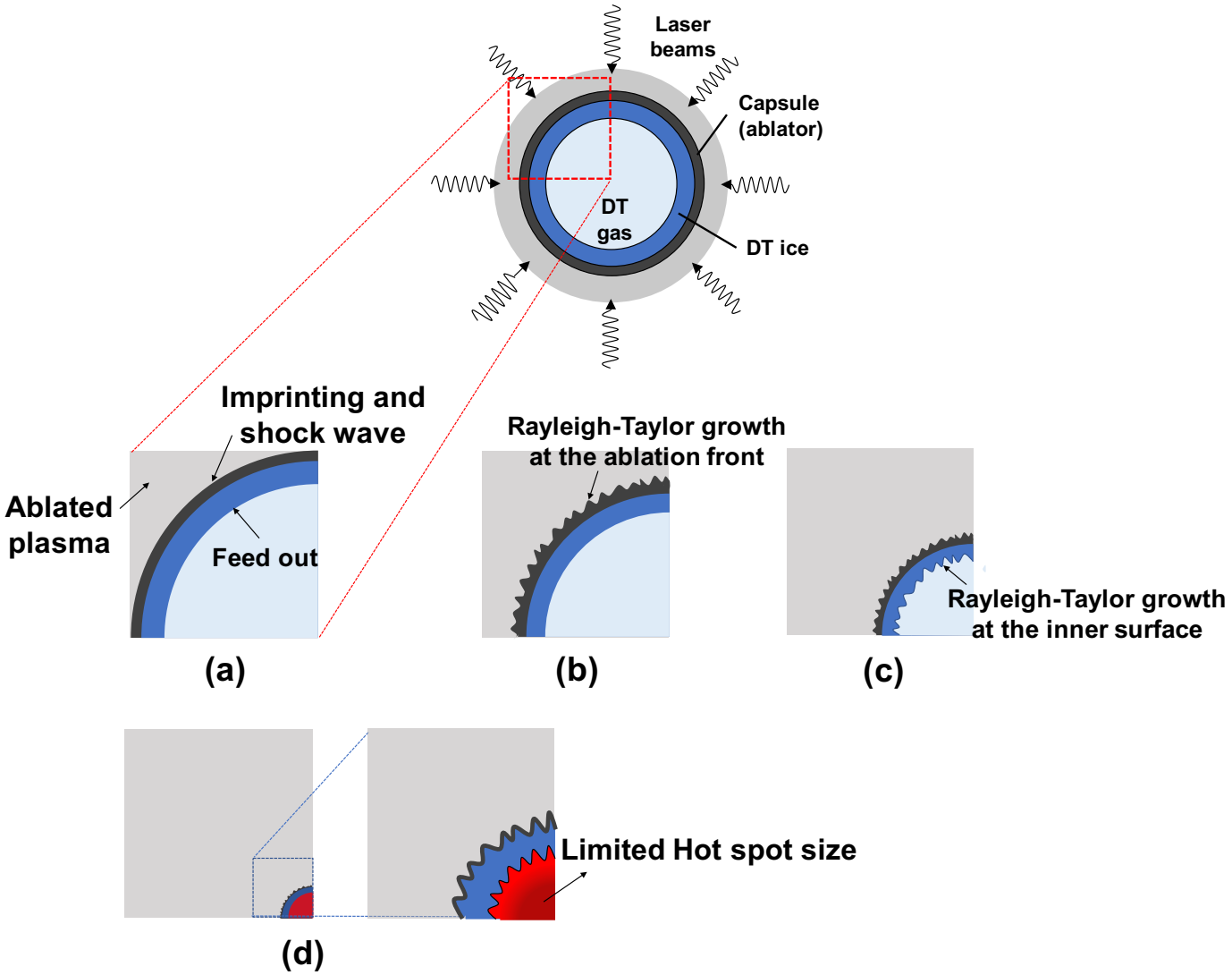

Figure 1.5: Schematic of the four main stages of a direct-drive target implosion. (a) Early stage. (b) Acceleration phase. (c) Deceleration phase. (d) Peak compression.

spot. The grown perturbation limits the hot spot size and reduces the fusion yields (Fig. 1.5(d)).

1.3 Hydrodynamic instabilities on direct-drive inertial confinement fusion

As mentioned in section 1.2, the RT instability occurs at two stages of the ICF implosion. First, it occurs at the outer surface of the shell (acceleration phase). The RT instability also develops at the shell inner surface, at the end of the implosion (deceleration phase), when the converging shell is slowed down by the pressure exerted by the inner hot spot. The RT instability is an important phenomenon in laser implosion because it limits the size of the hot spot in the fuel capsule. The Figure 1.6 shows the illustration of mechanism for the RT instability. The fluids are subjected to gravity, g, and a light fluid with density ρ_1 supports a heavily fluid with density ρ_2. In the bubble region, buoyancy acts dominantly, while gravity becomes dominant in the spike region. Therefore, the force acting on the spike or bubble is $(\rho_2 - \rho_1)\zeta g$, where ζ is the perturbation amplitude at the interface. By assuming incompressibility, i.e., $\nabla \cdot \boldsymbol{v} = 0$, the fluid velocity v_z in the z axis direction can be determined analytically. Using the relational expression $\nabla\phi \equiv \boldsymbol{v}$ of velocity potential ϕ and fluid velocity $\boldsymbol{v}$, Laplace equation is obtained:

$$\nabla^2\phi = 0. \tag{1.2}$$

Assuming that the velocity potential ϕ is $\phi = f(z)\cos ky$ (k is wave number), $\phi = f_0 e^{-k|z|}\cos ky$ is obtained from the equation (1), where f_0 is a time dependent parameter. Hence, the flow velocity v_z in the z axis direction is $v_z = \dot{\zeta} e^{-k|z|}\cos ky$, where $\dot{\zeta}$ represents a parameter of velocity depending on time t. The equation of motion in the z axis direction is

$$\begin{aligned} \frac{\partial}{\partial t}\left[\int_{-\infty}^{\infty}\rho(z)v_z(z)dz\right] &= (\rho_2-\rho_1)\zeta g \\ \frac{\partial}{\partial t}\left[\int_{-\infty}^{0}\rho_1\dot{\zeta}e^{kz}dz+\int_{0}^{\infty}\rho_2\dot{\zeta}e^{-kz}dz\right] &= (\rho_2-\rho_1)\zeta g \\ \frac{\ddot{\zeta}(\rho_1+\rho_2)}{k} &= (\rho_2-\rho_1)\zeta g. \end{aligned} \tag{1.3}$$

From, eq (1.3), in the classical Rayleigh instability of superposed fluids (Fig. 1.6(a)), sinusoidal perturbation ζ of the interface grows exponentially in time

$$\zeta = \zeta_0 \exp(\gamma_{\rm cl} t) \tag{1.4}$$

with growth rate $\gamma_{\rm cl} = \sqrt{Agk}$. $A = \frac{\rho_2-\rho_1}{\rho_2+\rho_1}$ is the Atwood number and ζ_0 is "small" initial amplitude.

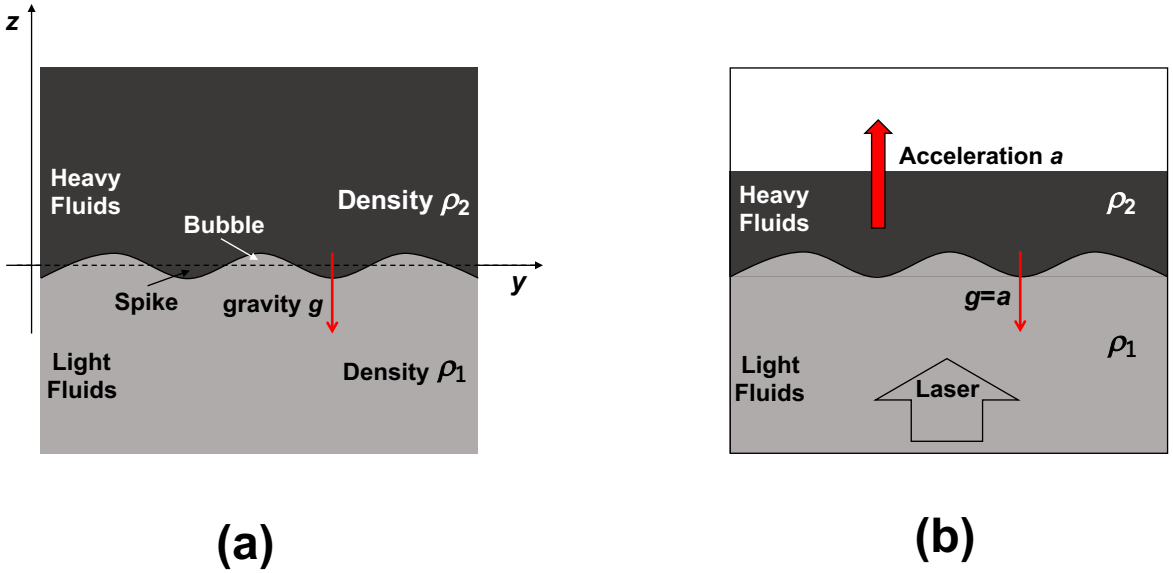

Figure 1.6: Concept of Rayleigh-Taylor instability occurring at the interfaces between fluids of different densities. In (a) a lighter fluid supports a heavier fluid; in (b) a lighter fluid accelerates a layer of denser fluid. two cases are equivalent.

The same considerations can be applied in a straightforward manner to the interface between two fluids in an accelerated frame (Fig. 1.6(b)). This is for instance the case of an ICF shell driven by hot ablating plasma. In a frame moving with the interface the fluid effectively sees an inertial force per unit mass $\boldsymbol{g} = -\boldsymbol{a}$, where $\boldsymbol{a}$ is the acceleration. The interface is then unstable if the acceleration is directed towards the denser fluid, which is just the case of the outer surface of an ICF shell during the stage of inward acceleration. For example, in laser fusion, the shell's acceleration is about 10^{16} (cm/s^2). Assuming that the wavenumber k and the Atwood number A are $2\pi/50\mu$m and ~ 1, respectively, then $\gamma \sim 3.5$ (1/ns) thus the amplitude is amplified to $e^{\gamma \cdot 2(\mathrm{ns})}$ (≈ 1000) times. The same case applies to the inner surface of the ICF shell in the deceleration phase.

It is known that the RT growth on the ablation surface due to laser irradiation is suppressed more than classical growth due to the existence of ablation flow across the boundary surface with different densities and smoothing of the density boundary surface due to the heat conduction. As mentioned above, the perturbation amplitude of classical RT instability grow in time as $\exp(\gamma_{\mathrm{cl}} t)$ and decay in space as $\exp(-kz)$, where z is the distance from the unstable interface. In the ablative RT instability, due to ablation, the interface moves inside the dense material with ablation velocity v_{a}. Therefore, the interface penetrates to the depth $v_{\mathrm{a}} t$ inside the dense material during time t. The effective growth of the perturbation at the interface is $\exp(\gamma_{\mathrm{cl}} t) \cdot \exp(-k v_{\mathrm{a}} t)$. The theoretical growth rate considering ablative stabilization is derived by Takabe *et al* [10] as follows:

$$\gamma \;=\; 0.9\sqrt{kg} - \beta k v_{\mathrm{a}} \tag{1.5}$$

Here, β is a dimensionless value, and $\beta = 3 \sim 4$ in the Ref [10, 21]. Various theoretical studies have been conducted on the growth rate on the ablation front afterwards, and expressions considering the density gradient of the ablation front are widely used [12]:

$$\gamma = \sqrt{\frac{kg}{1+kL}} - \beta k v_{\mathrm{a}}. \tag{1.6}$$

Here, L represents the density scale length ($|\rho/\nabla\rho|$) of the ablation front.

Richtmyer-Meshkov (RM) instability (RMI) is a hydrodynamic instability that occurs in a density discontinuous interface when a planar shock wave passes through a perturbed discontinuous interface. The shock front is distorted by the lens effect due to the distortion ξ_0 of the interface. A non-uniform velocity field is left at the perturbed interface ξ_0, the perturbation increases proportionally with time t, and its amplitude ξ_{RM} can be expressed as

$$\xi_{\mathrm{RM}} = \xi_0(1 + \alpha_{\mathrm{A}} k U_{\mathrm{s}} t), \tag{1.7}$$

where U_{s} is the shock wave velocity and α_{A} is the Atwood number. The atwood number α_{A} refers to the value taken just after the transit of the shock. Equation (1.7) shows that perturbation amplitude ξ_{RM} varies linearly in time t. As far as the ICF condition is concerned, RMI is certainly less dangerous than RT instability. It grows linearly in time, while RT instability grows exponentially in time. However, RMI can be seeds which are amplified by the RT instability later on.

1.4 Influence of initial surface perturbation to direct-drive ICF implosions

Imprinting due to non-uniform irradiation is an important trigger of non-uniformity for the direct-drive ICF implosions and imprint mitigation is crucial for reaching high convergence ratios without breaking shells apart. In this section, the quantitative estimation that initial surface perturbation influence the direct-drive ICF is described. This section also shows the simple estimation for the neutron yield degradation due to perturbation growth of shell inner surface.

When laser beams enter on spherical symmetry to a target capsule, the target is imploded by pressure of plasma formed on the surface. However, in the case of non-uniform irradiation, laser imprinting with various modes l occur on the outer surface in early phase, where l is the spehrical mode number. Mode number l corresponds to $\frac{2\pi R}{\lambda_l}$, where R and λ_l are capsule radius and perturbation wavelength of mode number l, respectively. In target implosion, imprinting perturbation amplitude $\zeta_l^{\rm imp}$ is amplified by Rayleigh-Taylor instability that occurs at the interface of accelerating materials with different densities. According to linear theory, the amplified amplitude $\zeta_l^{\rm out}$ at time t_0 by a perturbation of mode l at the outer surface is expressed as

$$\begin{aligned} \zeta_l^{\rm out} &= \zeta_l^{\rm imp}\Gamma_l^{\rm out} \\ &= \zeta_l^{\rm imp}\exp(\int_0^{t_0}\gamma_l(t)dt). \end{aligned} \tag{1.8}$$

$\Gamma_l^{\rm out} = \exp[\int_0^{t_0}\gamma_l(t)dt]$ is the growth factor for R-T instability, and γ_l is the linear growth rate of mode l. The linear growth rate γ_l is derived from the linear theory of ablative RTI. The linear growth rate γ_l is obtained from the linear theory of ablative RTI with the formula such as

$$\begin{aligned} \gamma_l(t) &= \alpha_2\sqrt{\frac{kg}{1+kL_{min}}} - \beta_2 k u_{\rm a} \\ &= \alpha_2\sqrt{\frac{gl/R}{1+lL_{min}/R}} - \beta_2\frac{l}{R}u_{\rm a}, \end{aligned} \tag{1.9}$$

where $\alpha_2 \simeq 1$ and β_2 takes values of 1.0 and $3 \sim 4$, respectively [10, 21]. From Refs. [1], the most unstable modes have l in the range 100-300 and corresponding growth factors $\Gamma_l^{\rm out}$ of about 1000. When the perturbations are amplified to the shell thickness, the shell breaks and the implosion performance declines. Thus, the grown perturbations must be sufficiently smaller than the in-flight shell thickness. In general, a surface perturbation needs to be suppressed within nanometer order.

At inner surface of the shell, the perturbation grows at the same rate as at ablation front, but with the amplitude reduced by a factor exp(-$\frac{l\delta R}{R}$). Such a phenomenon of transmission of a perturbation from an unstable surface to a stable one is known as "feed-through" and is important for ICF. Perturbations grown at the unstable ablation front are fed to the inner surface of the solid DT fuel during inward acceleration, where they seed the instability occurring at implosion stagnation. Feed-through is, however, negligible for perturbations with wavelength much smaller than the thickness of the shell. The inner surface of the shell becomes unstable when the imploding material starts to decelerate due to the pressure exerted by the inner hot spot. Seeds for such an instability are provided by both defects of the inner surface of the solid fuel with modal amplitude $\zeta_{l00}^{\rm in}$ and feed-through from the ablation front. The latter are caused by perturbations at the outer surface with spherical mode l and amplitude $\zeta_l^{\rm out}$, which are transmitted to the inner surface with amplitudes

$$\zeta_l^{\rm in-feed} \simeq \zeta_l^{\rm out}\exp(-l\delta R/R). \tag{1.10}$$

Assuming random phases, one estimates the effective initial amplitude of mode l as

$$\zeta_{l0}^{\rm in} \simeq [(\zeta_{l00}^{\rm in})^2 + (\zeta_l^{\rm in-feed})^2]^{1/2}. \tag{1.11}$$

RT instability will amplify such a perturbation according to

$$\begin{aligned} \zeta_l^{\rm in} &= \zeta_{l0}^{\rm in}\Gamma_l^{\rm in} \\ &= \zeta_{l0}^{\rm in}\exp(\int \gamma_l^{\rm in}(t)dt), \end{aligned} \tag{1.12}$$

where, $\gamma_l^{\rm in}$ is the growth rate of the deceleration-phase instability and is similar to eq.(1.9) of the growth rate on the outer surface [1]. Integration extends from the beginning of deceleration to just before ignition. Generally, it is found that the most dangerous modes for $\Gamma_l^{\rm in}$ have $l \approx 20$, higher modes being attenuated by feed-through and damped by the finite density gradient and ablation flow [1].

R-T instability and related instabilities cause deformations of the shell's outer and inner surfaces with amplitudes $\zeta^{\rm out}$and $\zeta^{\rm in}$, respectively. Ignition of an ICF target requires that the fuel shell with thickness $\Delta R(t)$ maintains its integrity during implosion and a central hot spot with radius $R_{\rm h}$ is created at stagnation. Therefore, it is required that

$$\zeta^{\rm out}(t) \ll \Delta R(t) \tag{1.13}$$

at any time t during implosion and

$$\zeta^{\rm in}(t) \ll R_{\rm h} \tag{1.14}$$

at implosion stagnation.

The number of neutrons generated by fusion reaction inside the hot spot depends on the DT particle number density ($n_{\rm D}$and$n_{\rm T}$) inside the hot spot, the fusion reaction rate $< \sigma v >$, and the volume $V_{\rm hot}$ of the hot spot. In the ideal case, the number $N_{\rm n}$ of generated neutrons per unit time is expressed as

$$N_{\rm n} = n_{\rm D} n_{\rm T} < \sigma v > V_{\rm hot} = n_{\rm D} n_{\rm T} < \sigma v > \frac{4}{3}\pi R_{\rm hot}^3. \tag{1.15}$$

Here, $R_{\rm hot}$ is the radius of hot spot. If there are perturbations $\zeta^{\rm in}$ due to hydrodynamic instability on the inner surface, the effective radius $R_{\rm eff}$ of the hot spot becomes small. As the effective radius $R_{\rm eff}$ decreases, the number $N_{\rm n}$ of generated neutrons per unit time decreases approximately as follows:

$$N_{\rm n} \approx n_{\rm D} n_{\rm T} < \sigma v > \frac{4}{3}\pi R_{\rm eff^3}$$

$$= n_{\rm D} n_{\rm T} < \sigma v > \frac{4}{3}\pi (R_{\rm hot} - \zeta^{\rm in})^3$$
$$\propto (R_{\rm hot} - \zeta^{\rm in})^3. \quad (1.16)$$

The figure 1.7 shows the decrease in the number of neutrons due to the inner surface perturbation. When the perturbation reaches half the radius of the hot spot, the number of generated neutrons decreases to about 10% of the ideal case.

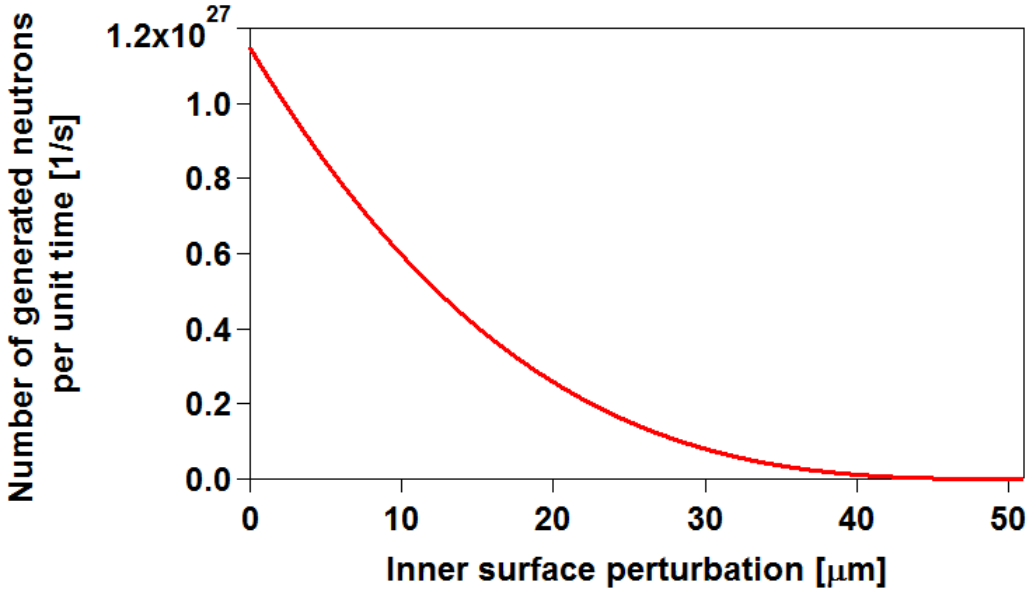

Figure 1.7: Estimation of decrease in neutron yield due to grown perturbations of shell-inner surface.

Also, the laser energy required for fusion ignition is related to the deformation of the hot spot (implosion core). The laser energy $E_{\rm ign}$ required for fusion ignition is expressed as follows:

$$\eta \cdot E_{\rm ign} = \frac{4}{3}\pi \frac{(\rho_{\rm hot} R_{\rm hot})^3}{< \rho_{\rm hot} >^2} E_{\rm h}, \quad (1.17)$$

where η is the the coupling efficiency from the laser energy to the hot-spot plasma, $E_{\rm h}$ is the thermal energy of the unit mass of the plasma at the temperature (5 keV) at which the fusion reaction occurs sufficiently, $R_{\rm hot}$ is the radius of hot spot, and $\rho_{\rm hot} R_{\rm hot}$ is the areal-density of hot spot. On the other hand, deformation of the implosion core due to fluid instability reduces the effective areal density. If $\delta R_{\rm hot}$ is

the perturbation amplitude of the hot-spot deformation, the effective areal-density can be expressed as $\rho R_{\rm eff} = \rho_{\rm hot} R_{\rm hot}(1 - \delta R_{\rm hot}/R_{\rm hot})$. Also, the maximum-allowed hot-spot size $R_{\rm hot}$ increases with the laser energy $E_{\rm ign}$ (or shell kinetic energy), $R_{\rm hot} \leq 40 \times 10^{-4}{\rm cm}(\eta \cdot E_{\rm ign}/10{\rm kJ})^{1/2}$ [11]. Therefore, the required energy $E_{\rm ign}$ considering the deformation of the hot spot can be rewritten as

$$E_{\rm ign} = \left[\frac{\delta R_{\rm hot}}{40 \times 10^{-4}} \times \frac{1}{1 - \left(\frac{4}{3}\pi(\rho R_{\rm eff})^3 \times (40 \times 10^{-4})^2 \times 0.1 \times \frac{\rm Eh}{0.3^2}\right)^{1/3}} \right]^2 \times \frac{10}{\eta} \ [{\rm kJ}]. \quad (1.18)$$

The figure 1.8 shows the relation between required laser energy $E_{\rm ign}$ and perturbation amplitude $\delta R_{\rm hot}$ of the hot-spot deformation, where coupling efficiency η is 0.04, thermal energy (at Temperature 5 keV) of the unit mass $E_{\rm h}$ is 5.75×10^5(kJ/g), and $\rho R_{\rm eff}$ is 0.3 g/cm^2. In order to achieve target ignition with laser energy of 100 kJ and 1 MJ, hot-spot deformation (or shell-inner perturbation) must be suppressed within $\sim 1\,\mu$m and $\sim 4\,\mu$m respectively. Laser energy required for target ignition increases markedly with nonuniformity.

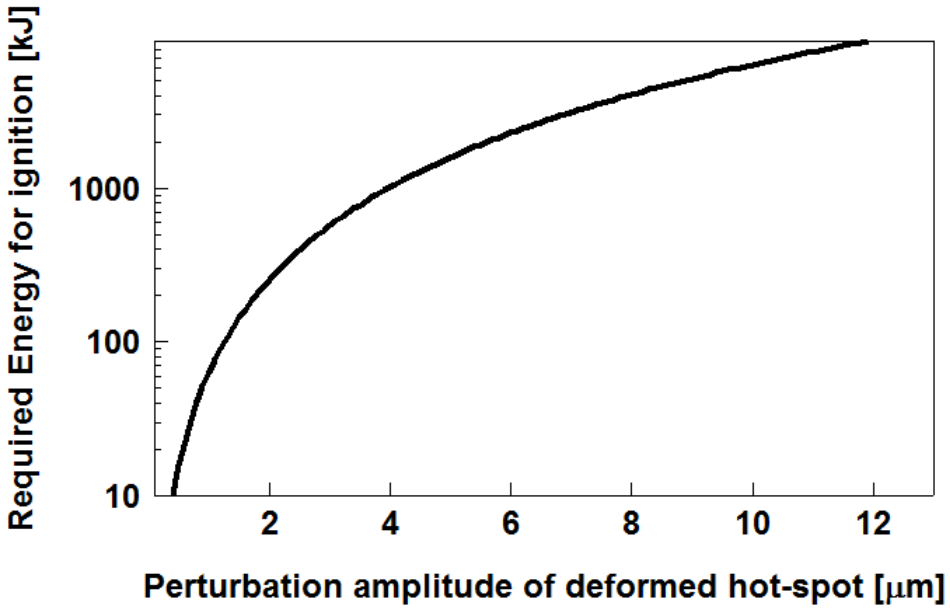

Figure 1.8: Estimation in relation between laser energy required for fusion ignition and allowance for hot-spot deformation (or shell-inner perturbations).

1.5 Significance of this study

In direct-drive inertial confinement fusion (ICF), a fuel capsule is irradiated directly with the intense laser beams. The target is imploded by pressure of ablation plasma formed on the surface. Then, fusion fuel is compressed and heated by target implosion. When high temperature of 50 million degrees or more (≥ 5 keV) and dense plasma of $\sim$1000 times the solid density are realized, explosive fusion reactions (fuel ignition and burn) become possible. In order to produce the fuel ignition and burn, spherically symmetric implosion of the capsule are required. However, initial imprinting due to irradiation non-uniformity on the capsule surface degrades symmetry of the target implosion and reduce the fusion yields as a result. Therefore, suppression of laser imprinting due to irradiation non-uniformity is a important subject on direct-drive ICF targets.

In this dissertation, comprehensive study of how the material stiffness and density affects laser imprinting by nonuniform laser irradiation of an inertial fusion target was conducted. Heretofore, no studies have focused on how the density and compressibility of the target material affect laser imprinting. The effect of density and compressibility is verified both by using 2D hydrodynamic simulations and by experiments for diamond and polystyrene (which is typical capsule material). The main goal of this study is to verify the theory and the two-dimensional calculation of laser imprinting for materials of various densities and compressibilities by comparison with the experiment.

Although the diamond with stiff characteristic becomes candidate as ablator materials, brittle materials such as diamond can easily cleave due to dynamic stress on a certain crystallographic plane. In the case of direct-drive inertial confinement fusion, in particular, the nonuniform laser irradiation would lead to local fracture on brittle material surface. However, so far, little research has been done on solid strength issues in surface perturbation due to nonuniform irradiation. In this study, perturbation structure and influence of the solid strength on diamond foils due to laser irradiation nonuniformity has also been investigated.

Also, high precise capsules with film thickness uniformity at the nano order level

is necessary for ICF target. And, the diamond with stiff characteristic becomes candidate as direct-drive ICF capsule materials. Aiming at improving performance of inertial confinement fusion (ICF) targets, synthesis technology of diamond capsules was developed. Synthesis and characterization of the diamond capsule by using the Hot Filament CVD method was investigated for the first time. This method without mechanical-polishing would be applicable to mass production of capsules.

1.6 Structure of this dissertation

This dissertation consists of seven chapters. In Chapter 2, a model of laser imprinting that affects the implosion performance of ICF targets is shown. It is described that material stiffness and density are important parameters to the mitigate laser imprinting by nonuniform irradiation. Chapter 3 explains equation of state in the radiation hydrodynamic simulation code for comparison with the experimental studies of laser imprinting. Equation of state is related to material stiffness and density. Chapter 4 shows the experimental and simulation studies of laser imprinting with diamond foils. The perturbation generated by irradiation nonuniformity was observed by amplifying its perturbation with hydrodynamic instability growth. The areal-density perturbation for single-crystal diamond and polystyrene foils was measured. Experimental results are compared with simulation calculations and the effects of material stiffness and density on laser imprinting is quantitatively evaluated. Chapter 5, in addition, perturbation structure on diamond foils due to laser irradiation nonuniformity has been investigated and the solid strength issues in non-uniform irradiation is discussed. Chapter 6 describes the fabrication and development of diamond capsules for ICF targets using chemical vapor deposition method. Chapter 7 is conclusion and the contents in this dissertation are summarized.

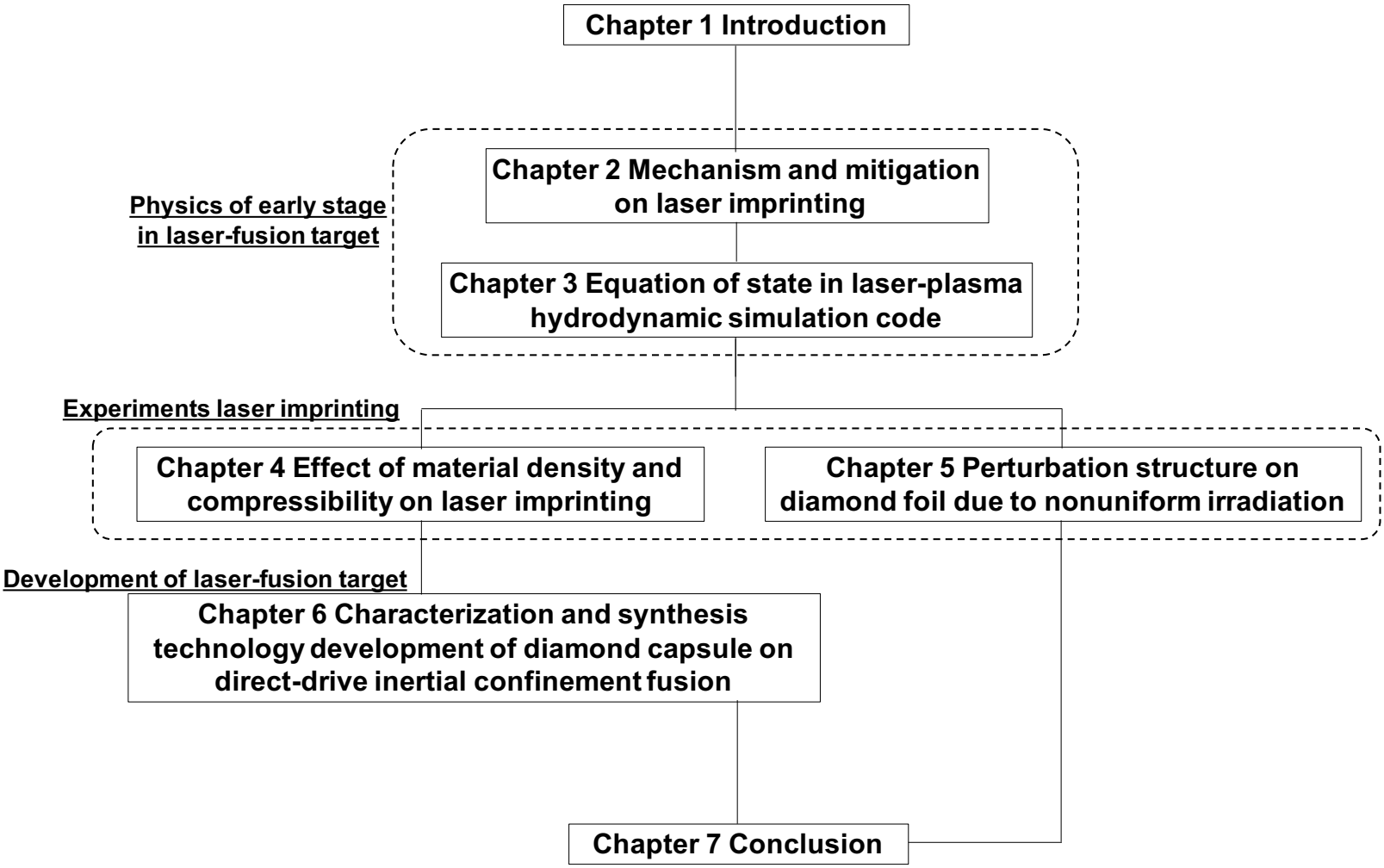

Figure 1.9: Flow chart of this study.

Chapter 2

Mechanism and mitigation on laser imprinting

2.1 Introduction

As shown in Chapter 1, laser imprinting occurs on the target surface due to irradiation non-uniformity at the early stage of direct-drive ICF. Imprint perturbation is amplified by Rayleigh-Taylor instability at the interface of accelerated materials with different densities. For the direct-drive ICF implosions, the imprint mitigation is crucial for reaching high convergence ratios without breaking shells apart. In this chapter, fundamentals of laser imprinting are reviewed and effect of material stiffness and density on imprint mitigation are discussed.

2.2 Modeling of laser imprinting

Figure 2.1(a) shows a schematic illustration of laser imprinting and indicate some physical notations. When a target is irradiated with an intense laser light, a corona plasma is formed and expands on the target surface rapidly, which is called ablation. The intense laser light produces the ablation pressure P_{a} at the ablation front; the ablation pressure launches a shock wave and introduces fluid flow (with

velocity v_{a0}) into the target. Irradiation with non-uniformity $\delta I/I_0$ produce the perturbation δP_{a} of pressure by ablation plasma, where $\delta I/I_0$ is intensity perturbation/average intensity. Pressure perturbation δP_{a} introduces the non-uniform fluid velocity δv_{a} on the ablation front. At the same time, rippled shock propagates into the target. The time derivative of total momentum MV_{depth} of the fluid with the flow v_{x} in target depth direction x between the ablation surface x_{a} and the shock front x_{s} is determined by the pressure P acting on the compressed region, the momentum loss $Loss_{\mathrm{y}}$ in the depth direction x due to the lateral flow v_{y}, and the momentum loss $Loss_{\mathrm{x}}$ in the depth direction x due to mass ablation of the x axis direction. If we ignore the momentum loss $Loss_{\mathrm{x}}$ by mass ablation to make it simple, the x component of the basic equation of motion in the shocked region is

$$\frac{\partial MV_{\mathrm{depth}}}{\partial t} + Loss_{\mathrm{y}} = -P|_{x_a}^{x_s}. \tag{2.1}$$

The momentum MV_{depth} corresponds to the total momentum (per unit area) of the fluid in the depth direction between the ablation surface x_{a} and the shock wave surface x_{s}:

$$MV_{\mathrm{depth}}(y,t) = \int_{x_a}^{x_s} \rho(x,y,t) v_x(x,y,t) dx. \tag{2.2}$$

In the case of non-uniform irradiation, the pressure perturbation causes momentum perturbation of the target. From the equation of motion, the time derivative of the momentum perturbation per unit surface imposed on the target should be equal to the pressure perturbation on the ablation front:

$$\frac{\partial \delta(MV_{\mathrm{depth}})}{\partial t} + \delta(Loss_{\mathrm{y}}) = \delta P_{\mathrm{a}}. \tag{2.3}$$

If the spatial density perturbation $\delta\rho$ can be ignored in the shocked region, the fluid velocity perturbation $\delta v_a(x,t)$ behind the shock wave attenuates along with the depth direction x [19, 21, 22]:

$$\delta v_x(x,y,t) = \delta v_a(x_a,y,t) e^{-k(x-x_a)}. \tag{2.4}$$

In other words, the momentum perturbation in the depth direction $\delta(MV_{\rm depth})$ is

$$\begin{aligned}
\delta(MV_{\rm depth}) &= \int_{x_a}^{x_s} \rho(x,y_1,t)v_x(x,y_1,t)dx - \int_{x_{a0}}^{x_{s0}} \rho(x,y_2,t)v_x(x,y_2,t)dx \\
&= \int_{x_a}^{x_s} \rho_s v_a(x,t)dx - \int_{x_{a0}}^{x_{s0}} \rho_{s0}v_{a0}dx \\
&= \int_{x_a}^{x_s} \rho_{s0}(v_{a0}+\delta v_a e^{-k(x-x_a)})dx - \int_{x_{a0}}^{x_{s0}} \rho_{s0}v_{a0}dx \\
&\approx \rho_{s0}v_{a0}(\delta x_s - \delta x_a) + \rho_{s0}\delta v_a \frac{1-e^{-k(x_{s0}-x_{a0})}}{k}. \qquad (2.5)
\end{aligned}$$

The subscript 0 denotes the unperturbed quantities. From Equation (2.4), velocity perturbation $\delta v_{\rm s}$ on the shock front can be approximated as

$$\delta v_s = v_{\rm s0}\frac{\delta v_a}{v_{\rm a0}}e^{-k(x_s-x_a)}, \qquad (2.6)$$

where $v_{\rm s0}$ is unperturbed velocity of shock wave. Therefore, the perturbation $\frac{\partial\delta(MV_{\rm depth})}{\partial t}$ of the force acting in the depth direction x can be expressed as

$$\begin{aligned}
\frac{\partial\delta(MV_{\rm depth})}{\partial t} &= \frac{\partial}{\partial t}\left\{\rho_{s0}v_{a0}(\delta x_s - \delta x_a) + \rho_{s0}\delta v_a\frac{1-e^{-k(x_{s0}-x_{a0})}}{k}\right\} \\
&= \rho_{s0}\delta v_a\{2v_{s0}e^{-k(xs0-xa0)} - v_{a0}(1+e^{-k(xs0-xa0)})\} \\
&+ \rho_{s0}\frac{1-e^{-k(x_{s0}-x_{a0})}}{k}\frac{d\delta v_a}{dt}. \qquad (2.7)
\end{aligned}$$

Here, the density behind the shock wave $\rho_{\rm s0}$ and the fluid velocity $v_{\rm a0}$ behind the shock wave are assumed to be independent of time.

At the same time, There is momentum due to the lateral fluid motion from the strongly to the weakly pushed region. The momentum loss due to the lateral flow in the depth direction is

$$\delta(Loss_{\rm y}) = \int_{x_a}^{x_s}\frac{\partial}{\partial y}(\rho_s v_y v_x)dx$$

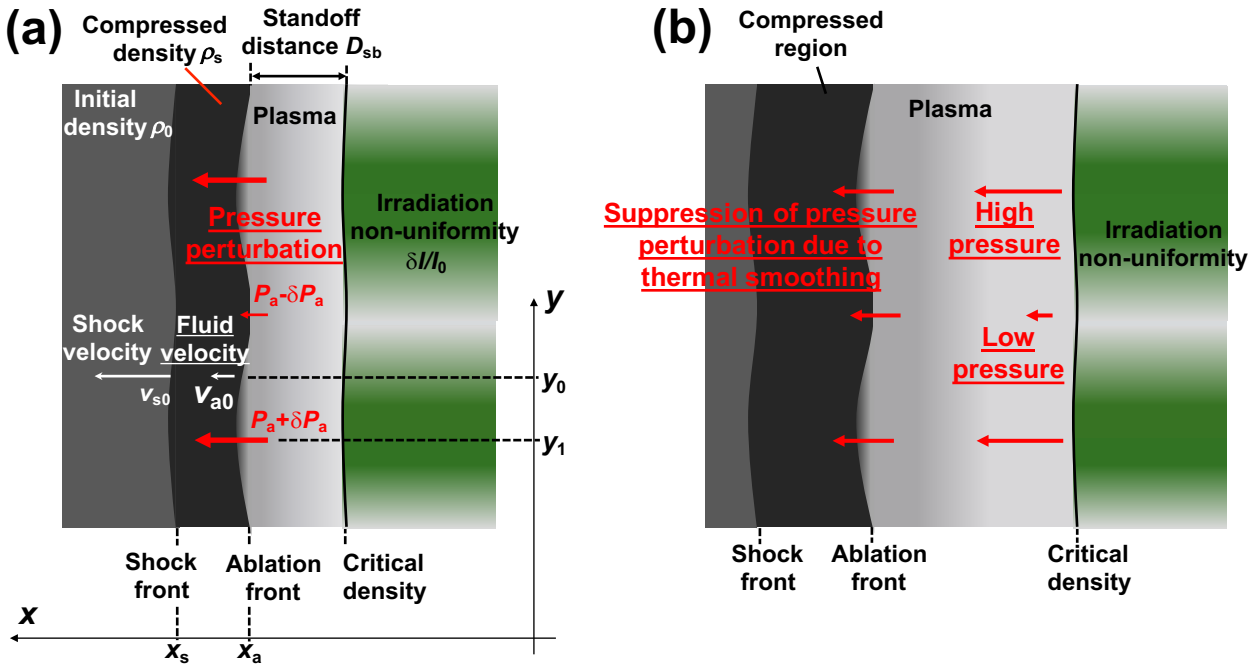

Figure 2.1: Schematic illustration of laser imprinting due to nonuniform irradiation: (a) Early irradiation time. (b) When time has elapsed from just after irradiation and the plasma region on the surface is expanded.

$$\begin{aligned} &\approx \rho_{s0} v_{a0} \int_{x_a}^{x_s} (-\frac{\partial v_x}{\partial x}) dx \\ &= \rho_{s0} v_{a0} \delta v_a (1 - e^{-k(x_{s0} - xa0)}) \\ &= \rho_{s0} v_{a0} \delta v_a (1 - e^{-kU_{s0}t}). \end{aligned} \tag{2.8}$$

$-\frac{\partial v_x}{\partial x}$ is derived from the assumption that the fluid is incompressible: $\nabla \cdot \boldsymbol{v} = 0$. Finally, from Equation (2.3), the equation describing the fluid velocity perturbation δv_a on the ablation front can be expressed as

$$\rho_{s0} \frac{d\delta v_a}{dt}(t) \frac{1 - e^{-k(x_{s0} - x_{a0})}}{k} + 2(v_{s0} - v_{a0}) e^{-k(x_{s0} - x_{a0})} \delta v_a(t) \rho_{s0} = \delta P_a(t). \tag{2.9}$$

Numerical calculation of momentum perturbation $\rho_{s0} \delta v_a$ on the ablation front can be simplified by Runge-Kutta method [19, 21, 22]. ρ_{s0}, x_{a0}, x_{s0}, and δP_a can be calculated from the 1D hydrodynamic simulation (ILESTA) [45] and the amplitude $\delta x_a(t)$ of the imprint perturbation is

$$\delta x_{\rm a}(t) \;=\; \int_0^t \delta v_a(t')dt'. \tag{2.10}$$

In the early phase, $k(x_{\rm s} - x_{\rm a}) < 1$, Eq.(2.9) approximately equals the following equation:

$$2(v_{\rm s0} - v_{\rm a0})\delta v_a\, \rho_{\rm s0} = \delta P_a(t). \tag{2.11}$$

The imprint amplitude (i.e., the perturbation of the ablation front) $\delta x_{\rm a}$ in very early irradiation timing can be obtained as

$$\begin{aligned} \delta x_{\rm a} &= \int_0^t \delta v_{\rm a}(t')dt' \\ &= \int_0^t \frac{\delta(P_{\rm a})}{2\rho_{\rm s0}(v_{\rm s0} - v_{\rm a0})}dt'. \end{aligned} \tag{2.12}$$

In general, the laser energy is mainly absorbed by a low-density plasma from the critical density surface to the laser direction via inverse-bremsstrahlung process. The laser absorption is spatially distributed along the laser path.The absorbed energy is then transported to the ablation surface by electron thermal conduction. For laser imprinting, pressure perturbation (or the temperature perturbation) is relaxed by diffusive electron's thermal conduction (see Fig. 2.1(b)). It is called thermal smoothing effect. This effect is taken into account in the model of laser imprinting. Then the pressure perturbation normalized by the unperturbed pressure $\delta P_{\rm a}/P_0$ may be given by cloudy-day model [23]

$$\delta P_{\rm a}/P_0 = \frac{2}{3}\frac{\delta I}{I_0}e^{-kD_{\rm sb}}, \tag{2.13}$$

where the factor 2/3 comes from the relation of $P \propto I^{2/3}$, $\exp[-kD_{\rm sb}]$ is a smoothing coefficient. The exponential factor stands for the reduction of the nonuniformity due to the thermal conduction from a point of the laser absorption to the

ablation surface. $D_{\rm sb}$ is the effective separation from a point of the laser absorption to the ablation front (called the “standoff distance”) as given by

$$D_{\rm sb} = -\frac{1}{k}\log\{\frac{\int_{-\infty}^{x_a} S(x)e^{-k(x_a-x)}dx}{\int_{-\infty}^{x_a} S(x)dx}\}, \tag{2.14}$$

where $S_{\rm abs}(z)$ is the absorbed laser power per unit length and k is the wavenumber of the laser nonuniformity. $x_{\rm a}$ is the position of the ablation front, and $-\infty$ corresponds to a position far from the target toward the laser. Although the imprint perturbations are suppressed by the thermal smoothing effect, when the wave number k of the irradiation nonuniformity or the standoff distance $D_{\rm sb}$ at early irradiation timing are small, suppression by thermal smoothing is not so effective. In other words, another new idea to compensate for a weak point of this effect is necessary.

2.3 Effects of material density and compressibility on laser imprinting

Consider a laser imprinting corresponding to small strain of the solid and very early irradiation times. When the strain of the solid is very small, the variation of the density $\rho_{\rm s}$ is small ($\rho_{\rm s} \approx \rho_0$), and the flow in the lateral direction y can be neglected. The equation of motion in the depth direction of the shocked region is as follows:

$$\frac{\partial \delta(MV_{\rm depth})}{\partial t} = \delta P_a. \tag{2.15}$$

Using Eq.(2.5) and Eq.(2.6), Equation (2.15) can be written as

$$\begin{aligned} \frac{\partial}{\partial t}\left\{\rho_{s0}v_{a0}(\delta x_s - \delta x_a) + \rho_{s0}\delta v_a \frac{1-e^{-k(x_{s0}-x_{a0})}}{k}\right\} &= \delta P_a \\ 2\delta v_{\rm a}\rho_{\rm s0}(v_{\rm s0} - v_{\rm a0}) &= \delta P_a. \end{aligned} \tag{2.16}$$

(Here, it is assumed that $k(x_{\rm so} - x_{\rm a0}) \ll 1$.) Hence, the imprint amplitude (i.e., the perturbation of the ablation front) $\delta x_{\rm a}$ can be obtained as

$$\begin{aligned} \delta x_{\rm a} &= \int_0^t \delta v_{\rm a} dt \\ &= \int_0^t \frac{\delta(P_{\rm a})}{2\rho_{\rm s0}(v_{\rm s0} - v_{\rm a0})} dt. \end{aligned} \tag{2.17}$$

Some parameters of laser imprinting are particularly important during very early irradiation times [i.e., when $\exp[kD_{\rm sb}({\rm t})] \approx 1$]. Equation (2.12), (2.17) also infers that density and compressibility, which are related to the equation of state (EOS), are functions of laser-imprinting amplitude. Based on conservation of mass across a shock wave in the form $\rho_{s0}/\rho_0 = v_{s0}/(v_{s0} - v_{a0})$ (see Appendix A.1), low compressibility implies a large difference $v_{s0} - v_{a0}$, that is, a stiff material with low compressibility ($= \rho_{s0}/\rho_0$) may reduce laser imprinting. In addition, the imprint amplitude is expected to decrease as the ablator density ρ_{s0} increases. The imprint amplitude δx_a can be approximated as

$$\begin{aligned} \delta x_a &= \int_0^t \frac{\delta(P_{\rm a})}{2\rho_{\rm s0}(v_{\rm s0} - v_{\rm a0})} dt \\ &\approx \frac{1}{3}\frac{\delta I}{I_0} \int_0^t v_{\rm a0} \cdot \exp[-kD_{\rm sb}(t)] dt. \end{aligned} \tag{2.18}$$

Thus, laser imprinting on a material is seeded by nonuniform motion of mass due to pressure perturbations ($\propto \delta I/\delta I_0 \cdot v_{\rm a0}$), which is related to material density and stiffness, as shown above. The EOS of a solid or a liquid can be represented as a sum of three components, which describe the elastic properties of the cold body, the thermal motion of the atoms (nuclei), and the thermal excitation of the electrons. Material stiffness or compressibility is related to the Hugoniot curve for a condensed substance and to the elastic pressure curves of a cold body, which are included in the EOS for a material. In particular, at very early times, material properties including the density and compressibility play an important role in laser

imprinting for long-wavelength perturbations and small standoff distance ($\mathrm{k}D_{\mathrm{sb}} \ll 1$). Also, material strength is expected to be essential in low-pressure conditions because compressibility in the solid state below the elastic limit is generally very small. The compressibility implicitly includes material strength, that is, Young's ratio and Poisson's ratio.

2.4 Dependence of materials on thermal smoothing effect

The standoff distance D_{sb} characterizing the thermal smoothing depends on the atomic weight A and atomic number Z, that is, the effect of thermal smoothing may be different depending on the material. The speed at which the standoff distance expands roughly corresponds to the velocity of the critical density surface c_{s} ($c_{\mathrm{s}} \gg$ fluid velocity behind the shock v_{a0}). The velocity of the critical density surface c_{s} can be estimated assuming steady-state planar flow [34]. Here it is assumed the laser-driven ablation front has a constant ablation rate, where the laser energy absorption is localized at the critical density surface. In the reference frame of the stationary ablation front, the conservation equations for planar flow (as described in Appendex A.1) can be applied [34]

$$\rho v = \rho_{\mathrm{c}} v_{\mathrm{c}} \tag{2.19}$$

$$P + \rho v^2 = P_{\mathrm{c}} + \rho_{\mathrm{c}} v_{\mathrm{c}}^2 \tag{2.20}$$

$$(\frac{5}{2}\frac{P}{\rho} + \frac{v^2}{2})\rho v + q_{\mathrm{a}} = (\frac{5}{2}\frac{P_{\mathrm{c}}}{\rho_{\mathrm{c}}} + \frac{v_{\mathrm{c}}^2}{2})\rho_{\mathrm{c}} v + q_{\mathrm{c,a}} + q_{\mathrm{c,out}} - I_{\mathrm{L}}, \tag{2.21}$$

where ρ, v, P are mass density, velocity and pressure and subscript c denotes quantities at the critical density. The heat flux at the ablation front is described by q_{a}, and $q_{\mathrm{c,a}}$, $q_{\mathrm{c,out}}$, and I_{L} describe the heat flux leaving the critical surface toward the ablation front, the outward flowing heat flux leaving the critical surface (away from

the ablation front), and the absorbed laser irradiance. If the thermal conduction is sufficiently high, the plasma expansion can be approximated by an isothermal rarefaction [1,34]. It is assumed that the laser maintains isothermal conditions in the ablating gas through heat conduction [1]. This leads to $q_{\mathrm{c,out}} = \rho_{\mathrm{c}} c_{\mathrm{T}}^3$, representing the additional heat flux needed to maintain isothermal conditions [1,34]. The isothermal sound speed, c_{T}, can be expressed as $c_{\mathrm{T}}^2 = P/\rho$. The rarefaction wave connects with the ablation flow as long as $v_{\mathrm{c}} = c_{\mathrm{T}}$. The heat at the ablation front emerges from the conduction zone, therefore $q_{\mathrm{a}} = q_{\mathrm{c,a}}$. At the ablation front $v = 0$ by definition. One can apply these conditions to Equation (2.21) leading to a relation between the absorbed laser intensity and hydrodynamic quantities,

$$I_{\mathrm{L}} = 4\rho_{\mathrm{c}} C_{\mathrm{T}}^3. \tag{2.22}$$

Evaluating Equation (2.20) at the ablation front yields [1,34]

$$P_{\mathrm{a}} = 2\rho_{\mathrm{c}} c_{\mathrm{T}}^2, \tag{2.23}$$

where P_{a} is the ablation pressure. The mass density at the critical surface, ρ_{c}, can be expressed in terms of the number density, n_{c}, as $\rho_{\mathrm{c}} = A m_{\mathrm{p}} n_{\mathrm{c}}/Z$, where A, m_{p}, and Z are the atomic weight, proton mass, and atomic number, respectively. The electron number density n_{c} of the critical surface is a function of laser wavelength [11], therefore

$$\rho_{\mathrm{c}} = \frac{A m_{\mathrm{p}}}{Z} \left(\frac{1.1 \times 10^{21}}{\lambda_{\mu\mathrm{m}}^2} \right), \tag{2.24}$$

where $\lambda_{\mu\mathrm{m}}$ is the laser wavelength in μm. Substituting Equations (2.22) and (2.24) into Equation (2.23) results in

$$P_{\mathrm{a}} = \left(\frac{A \cdot m_{\mathrm{p}} \cdot (1.1 \times 10^{21})}{2Z} \right)^{\frac{1}{3}} \left(\frac{I_{\mathrm{L}}}{\lambda_{\mu\mathrm{m}}} \right)^{\frac{2}{3}}. \tag{2.25}$$

The velocity of the critical density surface c_{s} can be estimated using the atomic weight A and atomic number Z. The velocity c_{s} can be expressed as

$$c_{\rm s} = v_{\rm c} = \left(\frac{1}{2}\right)^{\frac{7}{6}} \left(\frac{A \cdot m_{\rm p} \cdot (1.1 \times 10^{21}) \cdot \lambda^2 \cdot I^4}{Z}\right)^{\frac{1}{6}}, \tag{2.26}$$

where $m_{\rm p}$, λ, and I are proton mass, laser wavelength in μ m, and laser intensity in units of 10^{15} W/cm^2. However, for example, the velocity $c_{\rm s}$ for diamond ($A = 12$, $Z = 6$) is almost the same as the that of polystyrene ($A = 6.5, Z = 3.5$). Therefore the standoff distance $D_{\rm sb}$ between for diamond and polystyrene is almost the same level under the same laser intensities.

Although mitigating laser imprinting by increasing the standoff distance at the very early irradiation times ($\exp[(-k \cdot D_{\rm sb})] \approx 1$) is not effective, thermal smoothing may be affected by material differences because the velocity of the critical-density surface is basically related to the atomic weight and atomic number [34]. As shown in section 4.2.5, however, the standoff distances for diamond and polystyrene are almost the same for the given laser pulse.

Chapter 3

Equation of state in laser-plasma hydrodynamic simulation code

3.1 Introduction

For ICF target investigations, one needs information on material state over a large range of densities ($10^{-4} < \rho/\rho_0 < 10^4$, ρ_0 is solid density) and temperatures ($0 < k_\mathrm{B}T < 100\,\mathrm{keV}$), corresponding to pressures in the range of $0 < P < 10^{12}\,\mathrm{bar}$. k_B is Boltzmann's constant (1.38×10^{-23} [J/K]). In ICF, various phenomena such as laser absorption, electron heating, ablation, shock wave propagation, hydrodynamic instability, X-ray radiation, etc. occur. In many real processes the macroscopic parameters characterizing the state of the gas, such as the density ρ, specific internal energy ϵ, or temperature T, change slowly in comparison with the rates of the relaxation processes leading to thermodynamic equilibrium. Under such conditions gas particles are at any instant of time in a state that is very close to the thermodynamic equilibrium state corresponding to the instantaneous values of the macroscopic parameters. Therefore, such macroscopic behavior of plasma can be treated as the fluid. Also, radiation hydrodynamic simulations require the equation of state (EOS) and in particular radiation transport coefficients, which depend on material.

As described in Chapter 2, laser imprinting depends not only on thermal smooth-

ing due to diffusive heat conduction effect but also on density and compressibility of material. These parameters are closely related to the EOS of matter, The EOS is the important part to describe the shock wave formation and motion of ablation plasma.

Here we describe the EOS in the radiation hydrodynamic simulation code (PINOCO-2D [46]) for comparison with the imprint experiment in the next chapter. The PINOCO-2D is a radiation ALE (arbitrary Lagrangian Eulerian) hydrodynamic code. This code includes hydrodynamic, flux-limited Spitzer-Harm thermal conduction [33], nonlocal thermal equilibrium multi-group radiation transport, quotidian equation of state (QEOS) [48] and ray-trace laser energy deposition. For the EOS, we incorporated multiphase EOS [51] and table of melting curve [52] for a diamond with the QEOS model. In addition, we discuss the relation between the material compressibility and EOS.

3.2 Structure of equation of state in hot dense matters

The EOS indicates the internal state of materials, such as the pressure or internal energy of materials expressed by temperature or density. The EOS is related not only to ablation plasma motion and shock wave formation but also to laser imprinting. In quotidian equation of state (QEOS) model, the pressure P and internal energy E include elastic and thermal elements by ion and electron as follows:

$$P = P_{\mathrm{i}}(\rho, T_{\mathrm{i}}) + P_{\mathrm{e}}(\rho, T_{\mathrm{e}}) + P_{\mathrm{c}}(\rho) \tag{3.1}$$

$$E = E_{\mathrm{i}}(\rho, T_{\mathrm{i}}) + E_{\mathrm{e}}(\rho, T_{\mathrm{e}}) + E_{\mathrm{c}}(\rho), \tag{3.2}$$

where P_{c} and E_{c} are called elastic pressure and elastic energy, respectively. These macroscopic physical parameters are elastic components due to elastic force of the materials and are expressed as a function only of density ρ, which does not depend

on temperature T. The elastic component is related exclusively to the forces of interaction among atoms of the medium and it is needed to obtain reasonable results for a cold matter at/or near the solid density. $P_{\rm c}$ and $E_{\rm c}$ must be experimentally determined by measuring the sound speed or bulk modulus in the solid. $P_{\rm i}$ and $E_{\rm i}$ are parts due to thermal motion of ions, and $P_{\rm e}$ and $E_{\rm e}$ are components due to thermal excitation of electrons. They follows for different electron and ion temperature $T_{\rm e}$ and $T_{\rm i}$. For the pressure and internal energy due to ions, the Cowan EOS model [48] which takes into account the contributions due to atom vibrations is chosen. The electric contribution is calculated via a basic Thomas-Fermi (TF) model which includes particle interactions [26]. The QEOS is meant to be a standalone model with no need of libraries as in the case for SESAME [27].

3.3 Material stiffness by equation of state

As an example of full QEOS results, the pressure EOS of aluminum (Al) is shown in Fig. 3.1. It shows the effect of the ion EOS at low pressures and temperatures (order of tens of thousands of degrees). Above that temperature, thermal excitation of the electrons plays an important role. Also, EOS calculations included in PINOCO-2D simulation on the shock-compression curve of diamond and polystyrene (PS) foil are shown in the Fig. 3.2. The QEOS result for PS is in reasonably good agreement with the experimental data on shock-compression. In particular, in the simulation code PINOCO-2D, the EOS is based on the QEOS model coupled with recent multiphase calculation [51] and table of melting curve [52] (Fig. 3.3) for diamond. By adapting the parameters peculiar to the material in QEOS, the internal state of the material can be properly expressed and the result of the laser-driven shock compression experiments can be reproduced. As in Fig. 3.2 , compressibility for diamond is much smaller than PS which is a typical ICF capsule material. As mentioned in Section 2.3, there is the prediction that material compressibility (or material stiffness) would affect the laser imprinting. The laser imprinting on material is seeded by non-uniform mass motion due to

pressure perturbation, which is related to compressibility of target material (see Section 2.3). In the next chapter, experimental investigation on the effects of material compressibility on laser imprinting is shown. Also, based on these EOS, experimental results of laser imprinting are studied with the radiation hydrodynamic simulation (PINOCO-2D).

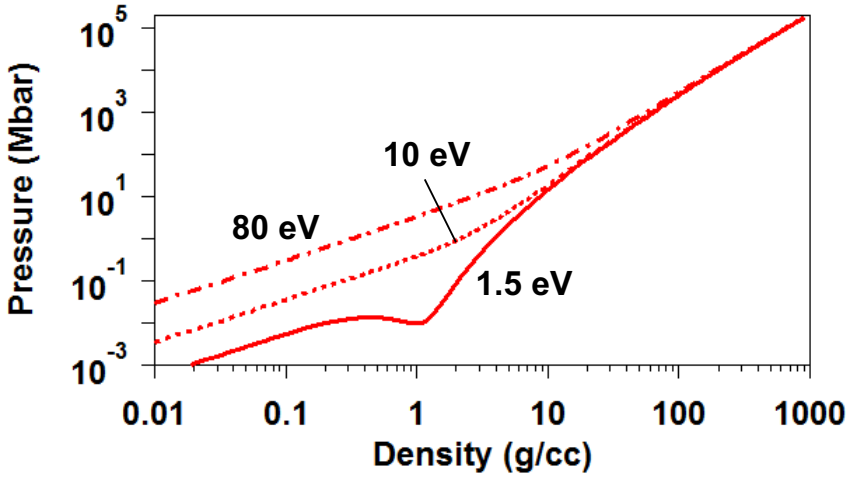

Figure 3.1: Total pressure of aluminum (Al) by QEOS model.

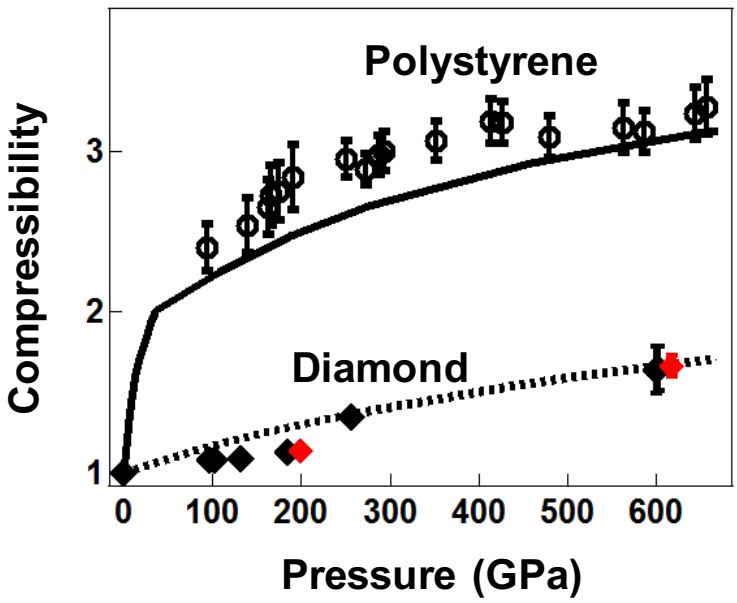

Figure 3.2: Shock compression curve for diamond and polystyrene foils. Open circles show the experimental data of shock compressibility (Compressed density/Initial density) for polystyrene foils [50]. Compressibility data on $< 100 >$-oriented single-crystal diamond and polycrystalline diamond [37] are squares black and red, respectively. A solid line is QEOS model calculation on the shock compression. A dashed line is QEOS model coupled with recent multiphase calculation [51] for diamond.

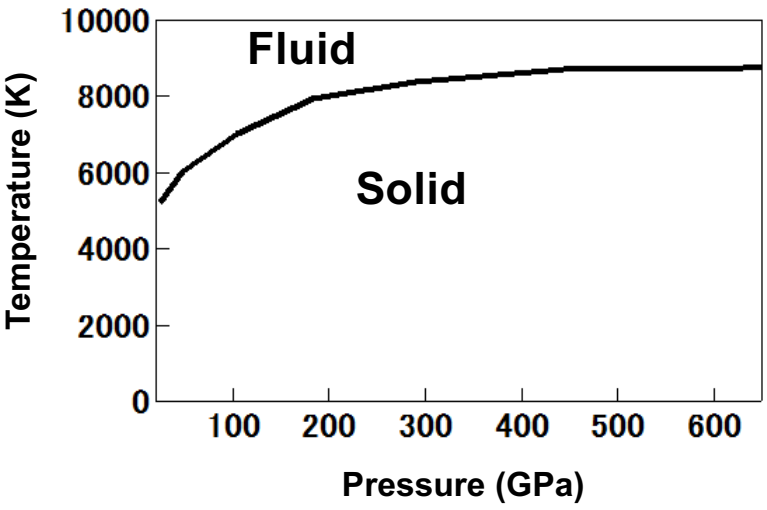

Figure 3.3: Melting curve [52] of diamond on high pressure and high temperature.

Chapter 4

Experimental investigation on the effect of material density and compressibility on the laser imprinting

4.1 Introduction

The Rayleigh-Taylor instability (RTI) is a hydrodynamic instability caused by gravity and is generally understood as a basic phenomenon in nature [13, 14]. As mentioned in Section 1.3, the RTI occurs at the interface between accelerating materials with different densities. In the inertial confinement fusion (ICF), the RTI and related hydrodynamic mixing are the most crucial factors determining thermonuclear ignition [4, 15] during the implosion timeline. Numerous studies of the RTI and related hydrodynamic instabilities have been done based on this understanding [16, 21]. Because the RTI makes small perturbations at the target surface grow exponentially over time, initial perturbations at the ICF target surface should be as small as possible. Such surface perturbations are mainly due to two factors: (i) the surface roughness resulting from target fabrication and (ii) imprinting due to nonuniform laser irradiation. Therefore, numerous efforts have

been made to understand the physics of laser imprinting [17–19]. The laser imprinting is caused primarily by pressure perturbations resulting from nonuniform laser irradiation (see Section 2.2). Such pressure perturbations introduce deformations on the target surface, followed by rippled shock propagation into the target [20]. The pressure perturbations are reduced within the coronal plasma via thermal smoothing as mentioned in Section 2.2. Many previous investigations have striven to mitigate the laser imprinting by enhancing the thermal smoothing by using low-density foam ablators [24, 25, 28, 29], radiation with high-Z coatings [30, 31], " picket " pulse irradiation [32], or soft-x-ray pre-irradiation [33]. Although these methods do mitigate the laser imprinting, they also increase fuel preheating and isentropicity. Moreover, at very early irradiation times, mitigating the laser imprinting by enhancing the thermal smoothing is not effective for long-wavelength perturbations nor for small plasma formation or insufficient standoff distance (see Section 2.2).

Some parameters of laser imprinting are particularly important during very early irradiation times. Equation (2.17) in Section 2.3 also infers that density and compressibility, which are related to the equation of state (EOS), are functions of laser-imprinting amplitude. A stiff material with low compressibility (= shock-compressed density ρ_{s0}/initial density ρ_0) may reduce the laser imprinting. In addition, the imprint amplitude is expected to decrease as the ablator density ρ_{s0} increases. The imprint amplitude δx_a can be approximated as

$$\begin{aligned} \delta x_a &= \int_0^t \frac{\delta(P_{\rm a})}{2\rho_{\rm s0}(v_{\rm s0}-v_{\rm a0})}dt \\ &\approx \frac{1}{3}\frac{\delta I}{I_0}\int_0^t v_{\rm a0}dt. \end{aligned} \tag{4.1}$$

Thus, laser imprinting δx_a is seeded by nonuniform motion v_{a0} of mass into the material due to irradiation nonuniformity $\delta I/\delta I_0$ ($\delta x_a \propto \delta I/\delta I_0 v_{a0}$), which is related to material density and stiffness, as shown above. The EOS of a solid or a liquid can be represented as a sum of three components, which describe the elastic prop-

erties of the cold body, the thermal motion of the atoms (nuclei), and the thermal excitation of the electrons (see Section 3.2). Material stiffness or compressibility is related to the shock compression curve for a condensed substance and to the elastic pressure curves of a cold body, which are included in the EOS for a material. In particular, at very early times, material properties including the density and compressibility play an important role in laser imprinting for long-wavelength perturbations λ and small standoff distance $D_{\rm sb}$ ($\frac{2\pi}{\lambda}D_{\rm sb} \ll 1$). Also, material strength is expected to be essential in low-pressure conditions because compressibility in the solid state below the elastic limit is generally very small. The compressibility implicitly includes material strength, that is, Young's ratio and Poisson's ratio. Although mitigating laser imprinting by increasing the standoff distance at the very early irradiation times is not effective, thermal smoothing may be affected by material differences because the velocity of the critical-density surface is basically related to the atomic weight and atomic number [34]. As shown below, however, the standoff distances for diamond and polystyrene (PS) are almost the same for a given laser pulse.

Heretofore, no studies have focused on how the density and compressibility of the target material affect laser imprinting. Diamond is the most probable candidate for a stiff ablator material for ICF targets because it has a small atomic number and a large elastic limit. Sophisticated studies of diamond under ultrahigh pressure have recently been conducted by using high-intensity lasers [35–37] and Z-pinch machines [38] and have demonstrated that diamond has both a large elastic-plastic transition pressure [37] and a high melting temperature [36], thus indicating that diamond maintains low-compressibility under high pressure and high temperature.

In this chapter, detailed results of simulations showing how material density and compressibility affect laser imprinting are reported. The main goal of this paper is to verify the theory and the two-dimensional calculation of laser imprinting for materials of various densities and compressibilities by comparison with the experiment. Section 4.2. describes in detail the experimental conditions of measurements of areal-density perturbations caused by nonuniform irradiation.

Face-on x-ray backlighting, which is a standard technique for measuring hydrodynamic instabilities was used. Section 4.3 presents and analyzes the experimental data on areal-density perturbations and target trajectories. Section 4.4 analyzes laser imprinting by using the two-dimensional hydrodynamic simulation code PINOCO-2D. The spatial perturbation amplitude due to laser imprinting and the areal-density perturbation amplitude based on comparisons with the experimental results are described. That section also show comparison of the basic hydrodynamic parameters determined from the laser imprinting amplitude. All materials used in the simulation, experiment, and the theoretical model lead to the same result that density and compressibility are the key factors of laser imprinting.

4.2 Experimental conditions

The experiment was conducted at the GEKKO-XII Nd:glass laser facility at the Institute of Laser Engineering, Osaka University [39]. An overview of the experimental setup is shown in Fig. 4.1. Flat foils were irradiated with the second harmonic (λ=0.527 μm) of a Nd:glass laser. The pulse shape was Gaussian with a full width at half maximum of 1.3 ns, using one beam for the foot pulse and two stacked beams for the main drive pulse with time delays between the pulses. A typical pulse shape is shown in Fig. 4.1. Each beam was smoothed by using a random-phase plate [40]. Because the perturbation by laser imprinting is typically very small for direct observation, perturbations of the target material were measured via amplification through the growth of the RTI caused by the drive beams.

The intensity of the foot pulse was modulated by placing a grid mask in front of the focusing lens. Figure 4.2(a) shows the spatial pattern and intensity distribution of the foot pulse at the target. The nonuniformity of the higher spatial-harmonic components (wavelength=20$\sim$50 μm) in the imprint pulse was less than 10 % of the nonuniformity of the fundamental wavelength [see Fig. 4.2(b)]. The modulation wavelength at the target surface was 100 μm, with $\sim$ 10 % intensity nonuniformity ($\delta I/I_0$). The two foot-pulse intensities were chosen mainly to investigate the imprint perturbation in the elastic and plastic states of diamond. The averaged

intensities I_0 of the foot pulse were $4 \times 10^{12}\,\mathrm{W/cm^2}$ (" low-foot " condition) and $5 \times 10^{13}\,\mathrm{W/cm^2}$ (" high-foot " condition). The high-foot pulse rapidly produces a shock stress via the plastic response (>160 GPa) for diamond [37]. The peak intensity of the main pulse was $1 \times 10^{14}\,\mathrm{W/cm^2}$.

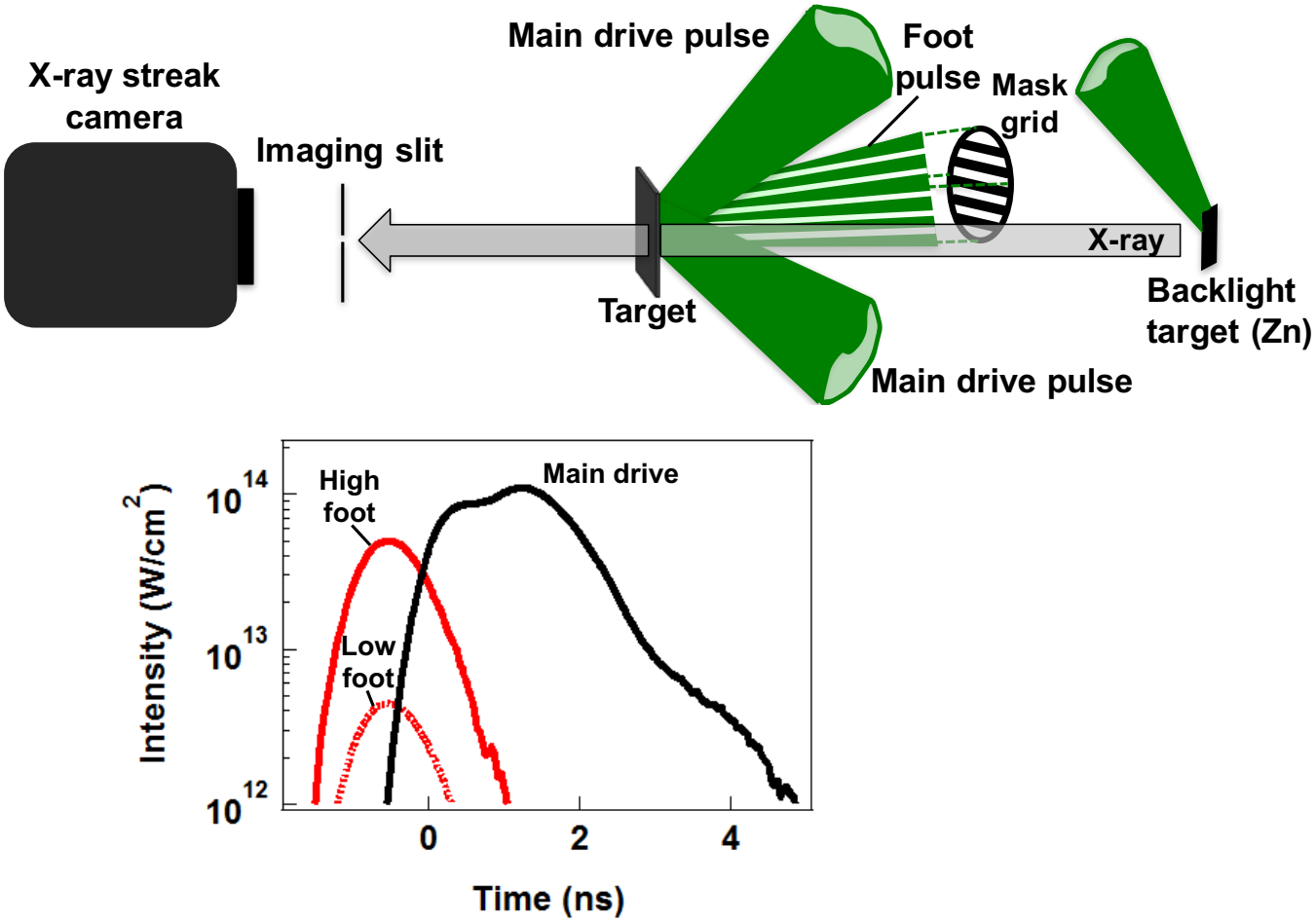

Figure 4.1: Top panel shows the experimental setup for the face-on x-ray backlighting measurement of areal-density perturbations seeded by nonuniform laser irradiation. The bottom panel shows a typical pulse shape.

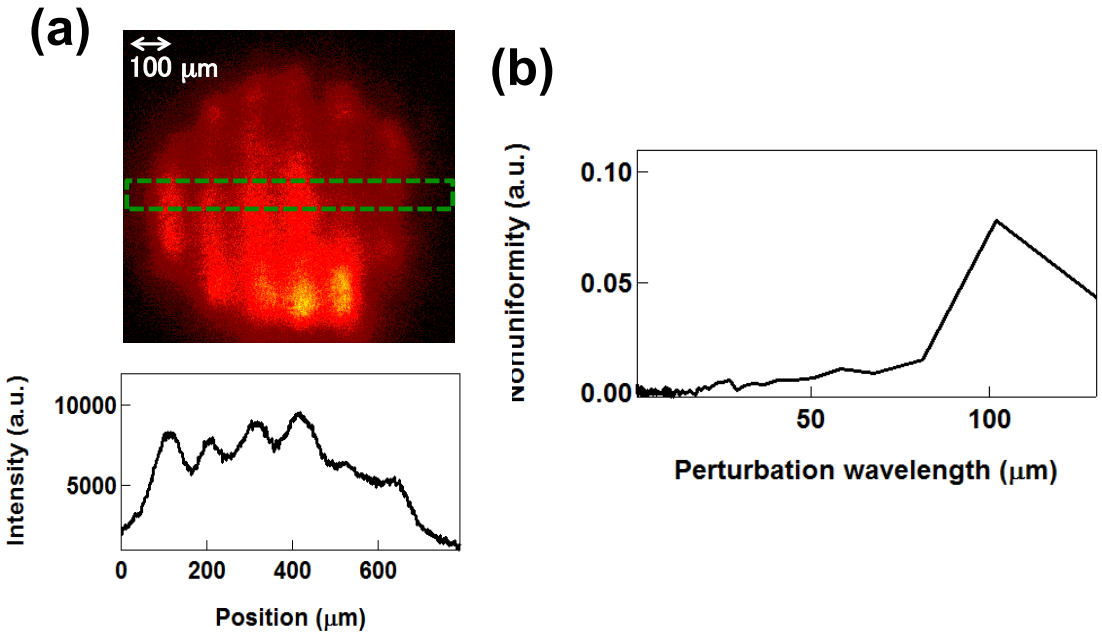

Figure 4.2: (a) Spatial pattern of the foot pulse at the target surface. (b) Modulation wavelength spectrum of nonuniform irradiation.

The targets were 13-μm-thick single-crystal diamond foils (type-Ib, initial density= 3.51 g/cm^3). The surface orientation of the single-crystal diamond was (100) plane. PS foils (initial density= 1.06 g/cm^3) with a thickness of 25 μm were used as a reference material because several previous RTI experimental results are available for PS [41–43], along with precise EOS data [44] and experiment data on laser imprinting of PS [19, 21, 22]. The foil surfaces were coated with 0.05 μm of Al as a shield against shine-through inside the foils during very early irradiation times.

The areal-density-perturbation growth was measured by using the face-on x-ray-backlighting technique. A backlight target (Zn) was irradiated to generate ∼1.5 keV quasimonochromatic x-rays coupled with a 6-μm-thick Al filter. The quasimonochromatic x-rays energy and absorption coefficient necessary for data analysis of areal-density perturbation are measured by using "cold" foils (see Fig. 4.3). The temporal evolution of the transmitted x-rays from the Zn backlighter through a diamond or PS foil was imaged by a slit (10×50 μm^2) onto the CuI photocathode of an x-ray streak camera with 26× magnification. The temporal resolution of the x-ray streak camera was 143.1 ps.

As shown in Fig.4.4(a), the trajectories of the irradiated foils were measured separately by using side-on x-ray backighting so as to evaluate their basic hydrodynamics based on comparison with the results of the simulations described in Section 4.3. The drive-laser conditions were the same as for the areal-density-perturbation measurements. A Cu backlit target was placed in the direction perpendicular to the target-acceleration direction. The temporal evolution of the transmitted x-rays from the Cu backlighter through accelerated flat foil (diamond or PS foil) was imaged by a slit ($20 \times 50\,\mu$m^2) onto the CuI photocathode of an x-ray streak camera with a 20× magnification. The temporal resolution of the x-ray streak camera was ∼100 ps.

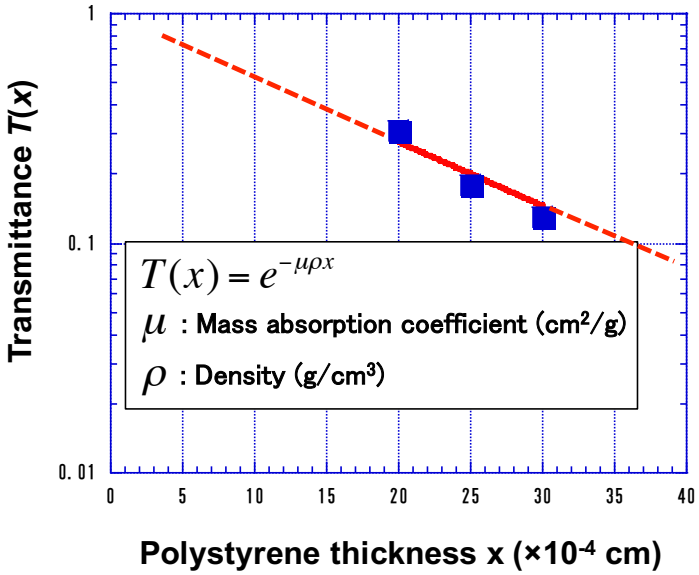

Figure 4.3: Transmittance of Zn backlighter with 6-μm-thick Al filter to polystyrene thickness: The experimental data (symbols) is in good agreement with the calculated value (red line) when the mass absorption coefficient μ of polystyrene (density $\rho = 1.06$ (g/cm^3)) is 606.78 (g/cm^2). Then, the x-ray photon energy corresponds to 1.53 keV.

4.3 Experimental results

4.3.1 Target trajectory with side-on backlighting method

The target consists of the accelerated foil target, a 50-μm-thick Be substrate, and a 50-μm-thick Al spacer, as shown in Fig.4.4(a). Figure 4.4(b) shows an example of a raw streaked side-on image of the target acceleration trajectory. The time origin (t=0) is when the rise of the drive pulse reaches 50% of the maximum peak intensity. In Fig.4.4(b), the Be substrate and the accelerated diamond target are indicated in the backlight image. The raw image is line scanned at various observation times and integrated over a time approximately equal to the temporal

resolution [see example in Fig. 4.4(c)]. From the x-ray spatial profile provided by raw data, we determine the center of mass of the accelerated foil target.

The experimental trajectory is compared with the results of the ILESTA-1D simulation code [45] and of the two- dimensional radiation hydrodynamic code PINOCO-2D [46]. As seen in Fig.4.4(d), both simulation results are consistent with the experiment result. Then, the maximum intensity of the main drive for accelerating the target is $8.8 \times 10^{13}\,\mathrm{W/cm^2}$ and the average acceleration of the diamond foil (Thickness 17.5 μm) is $1.6 \times 10^{15}\,\mathrm{cm/s^2}$. The table 4.1 shows the observation results of the target acceleration trajectory for each laser shots.

In this study, we use the ILESTA-1D code to evaluate the basic hydrodynamic parameters for “ unperturbed ” conditions (e.g., shock breakout time, onset of foil acceleration, and standoff distance). To analyze the laser imprinting under “ perturbed ” conditions, we use the PINOCO- 2D simulation code.

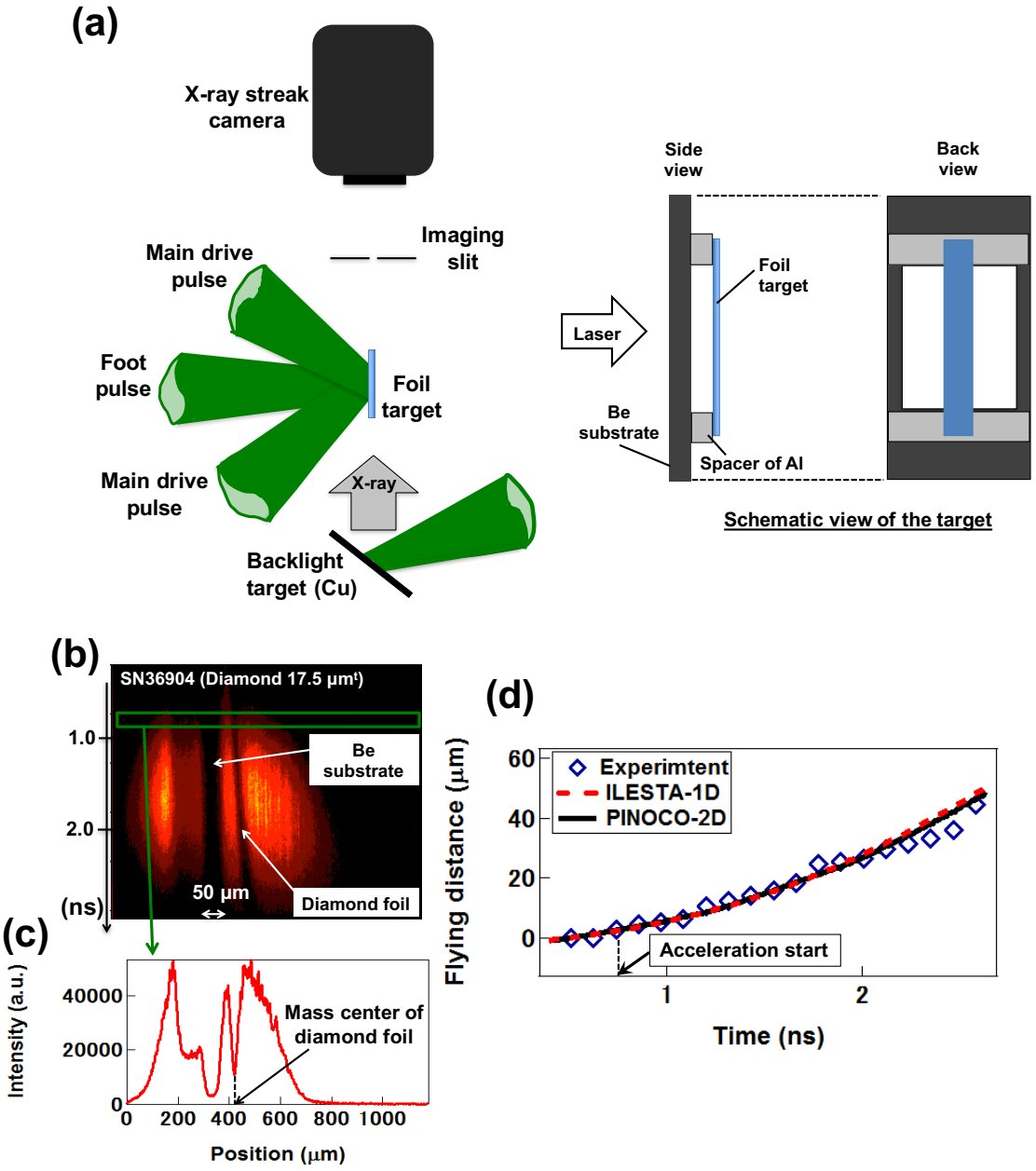

Figure 4.4: (a) Schematic illustration of the experimental setup for measuring acceleration trajectory. A schematic illustration of the target is also shown. (b) Raw streaked image of the target trajectory measured by side-on x-ray backlighting. (c) Lineout of the raw image at t=0.8 ns. (d) Target trajectory (center of mass) of diamond foil from the experiment and from simulation.

Table 4.1: Observation results of the target acceleration trajectory for each laser shot.

Shot No	Target foil (Thickness)	Maximum intensity of the main drive [W/cm^2]	Target acceleration [cm/s^2]
36899	PS (25.0 μm$^{\rm t}$)	6.50×10^{13}	$\sim 3.70 \times 10^{15}$
36902	Diamond (15.0 μm$^{\rm t}$)	8.08×10^{13}	$\sim 2.15 \times 10^{15}$
36904	Diamond (17.5 μm$^{\rm t}$)	8.83×10^{13}	$\sim 1.61 \times 10^{15}$

4.3.2 Growth areal-density perturbation with the face-on backlighting method

The spatial resolution for x-ray imaging system was measured by using a backlit gold grid image to analyze the areal-density perturbation. The Au mesh (63.5 μm/period) was used to obtain the backlit grid image. In the measurement system of this experiment, there are mainly two imaging systems, including the imaging slit and the optical system inside the x-ray streak camera. The resolution function of the entire diagnostics system is given by the sum of two Gaussian functions as

$$R(x) = \left(\frac{1}{1+\alpha}\right)\left(e^{\frac{-x^2}{2\sigma_1^2}} + \alpha e^{\frac{-x^2}{2\sigma_2^2}}\right). \tag{4.2}$$

Here, x is the position. From the Fourier transform of $R(x)$, Modulation Transfer Function (MTF) can also be obtained:

$$\mathrm{MTF}(k) = \left(\frac{1}{\sigma_1 + \alpha\sigma_2}\right)\left(\sigma_1 e^{\frac{-\sigma_1^2 k^2}{2}} + \alpha\sigma_2 e^{\frac{-\sigma_2^2 k^2}{2}}\right), \tag{4.3}$$

The x-ray intensity I observed by the streak camera can be expressed by a convolution of the x-ray intensity distribution $I_{\rm G}$ just after passing through the grid and the resolution function $R(x)$:

$$I(x) \quad = \quad \int R(x-u) I_{\mathrm{G}}(u) du. \tag{4.4}$$

Here x is the position. Figure 4.5(a) represents the raw data of backlit grid image observed by experimental system as in Fig. 4.1, and also shows the spatial profile of the backlit grid image obtained by integrating the raw data into the time resolution (143.1 ps). As shown in Fig. 4.5(b), spatial resolution are obtained by fitting the raw profile with the fitting function I in eq. (4.4), where $\alpha = 0.194$, $\sigma_1 = 5.753\,\mu$m, and $\sigma_2 = 20.381\,\mu$m for this measurement. The intensity distribution I_{G} corresponds to a step function with the spatial profile of the backlight X-ray source. I_{G} (input step function) was determined from the profiles of backlit grid image and the backlit source (as in Fig 4.5(b)). Figure 4.6 shows the resolution function $R(x)$ and MTF in this experimental measurement system. The full width at half maximum (FWHM) of the resolution function $R(x)$ is $\sim 15\,\mu$m, which corresponds to the spatial resolution of the x-ray imaging system.

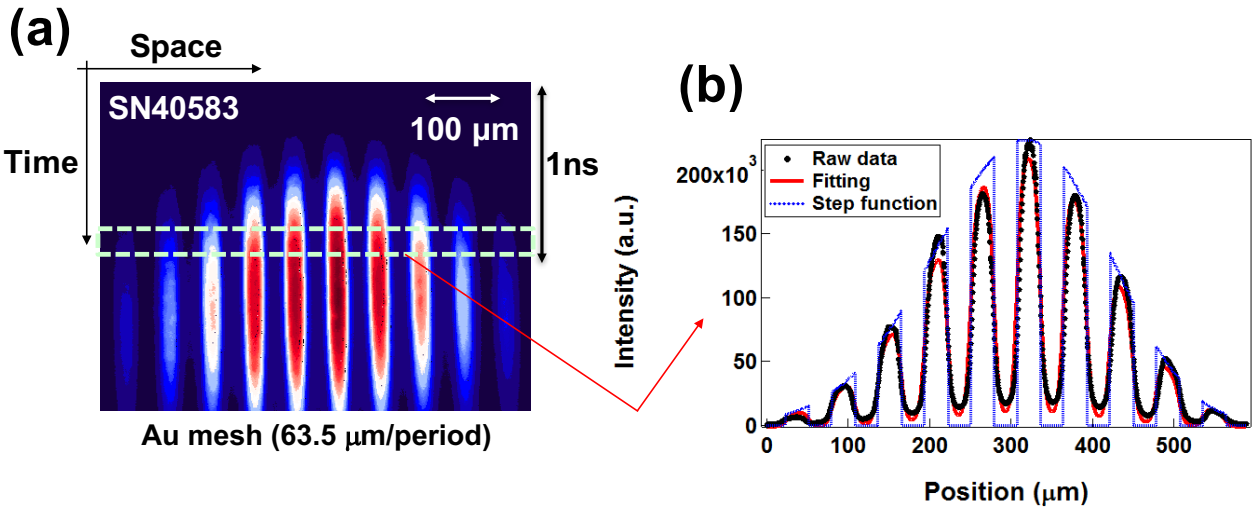

Figure 4.5: (a) Raw streaked images for face-on x-ray backlit grid on the spatial resolution measurement. (b) Determination of spatial resolution by fitting the raw profile with the fitting function.

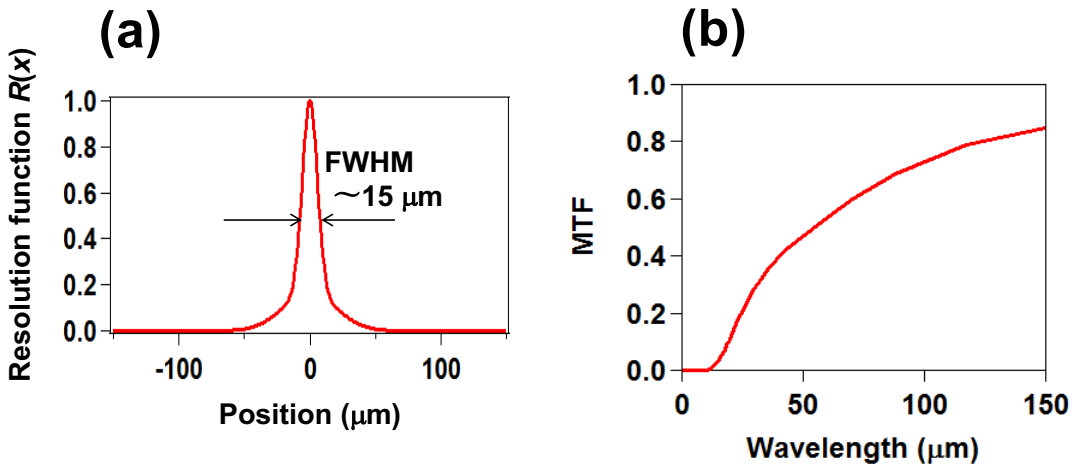

Figure 4.6: (a) Spatial resolution function R(x). The half value width (FWHM) of $R(x)$ is about 15 μm. (b) Modulation Transfer Function (MTF). The perturbation wavelength corresponding to MTF = 5% is defined as the spatial resolution of the x-ray imaging system.

Figure 4.7 shows raw streaked face-on backlit images for the diamond and PS targets the high-foot and low-foot irradiation conditions. The time origin (t = 0) of the main pulse is as described above. All experimental results were acquired during the foil-acceleration phase.

"Lineouts" are extracted by integrating the raw data over the temporal resolution, as indicated in Fig. 4.7 for t=1.7 ns. The lineouts shown are the backlit x-ray intensity distribution and the fitted profile. The areal-density perturbations are obtained by fitting the convolution of the resolution and a sinusoidal perturbation function to the raw lineouts, taking into account the x-ray absorption coefficient (at $h\nu$ = 1.53 keV), which was separately calibrated by using "cold" foils (as mentioned in Section 4.2). The raw lineouts I(x) is expressed as

$$I(x) = \int R(x-u) I_0(u) e^{-\mu\{\delta\rho l cos(ku)\}} du, \tag{4.5}$$

where I_0 is the spatial profile of the backlit x-ray source, $\delta\rho l$ are perturbation amplitudes of the fundamental component (fundamental wavelength $\lambda = 100\,\mu$m). k (=$2\pi/\lambda$) is the wave number of the raw lineouts.

In the fitting procedure, second- and third-harmonic spatial components (wavelengths of 50 and 33 μm, respectively) of the areal-density perturbation due to the irradiation non-uniformity are also taken into account. The effect of including the higher harmonic components falls within the fitting error of the areal-density perturbation plots.

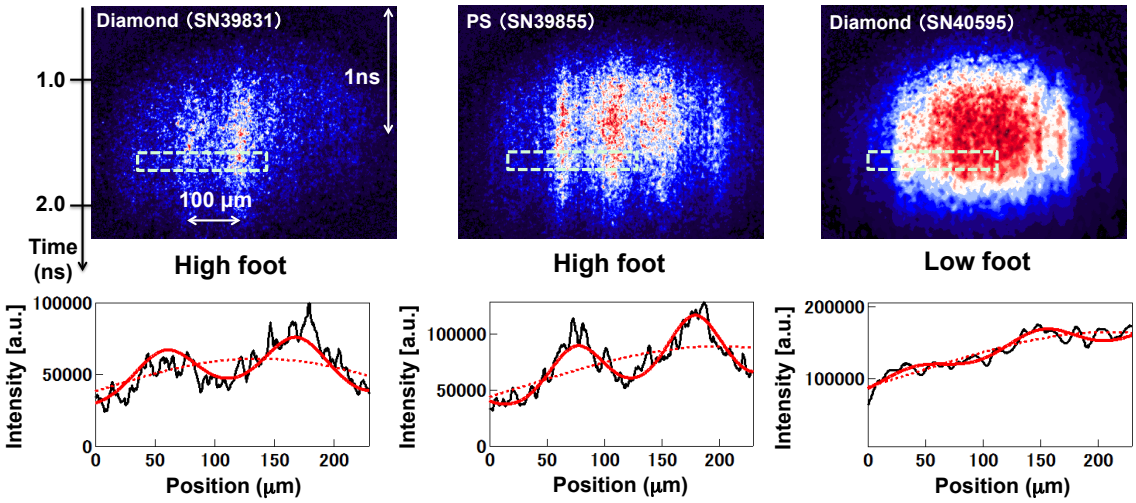

Figure 4.7: Raw streaked images for face-on x-ray backlit diamond and PS foils. All lineouts are at t=1.7 ns. Red lines are curve fits for each profile.

4.4 Analysis of laser imprinting with the radiation hydrodynamic simulation

4.4.1 Growth of areal-density perturbation from the experiment and comparison with results of PINOCO-2D simulation

Figure 4.8(a) shows the temporal evolution of the areal-density perturbations amplified by the RTI for diamond and PS foils. Also plotted in Fig. 4.8(a) are the results of simulations of the three experimental configurations by the two-dimensional radiation hydrodynamic code PINOCO-2D [46]. PINOCO-2D gives

the arbitrary Lagrangian Eulerian (ALE) hydrodynamic for the radiation. This code includes hydrodynamic, flux-limited Spitzer-Härm thermal conduction [47], nonlocal thermal equilibrium multigroup radiation transport, quotidian equation of state, and ray-trace laser-energy deposition. For the EOS, we incorporated an elastic-plastic boundary [48], a multiphase EOS [51], and a table of melting curves [52] for diamond with the quotidian equation of state model. The results of PINOCO-2D are consistent with the experiment results for the three configurations.

Figure 4.8(b) shows the averaged target densities during the foil-acceleration phase, as calculated by the ILESTA-1D code. During the acceleration phase, the areal-density perturbation $\delta\rho l$ detected by using face-on backlighting is expressed [see Fig. 4.9(b)] as $\delta\rho l = \delta(\int \rho dx) = \int_{x_\mathrm{a}+a(x_\mathrm{a})}^{x_\mathrm{r}+a(x_\mathrm{r})} \rho(x, y_\mathrm{p})dx - \int_{x_\mathrm{a}}^{x_\mathrm{r}} \rho(x, y_\mathrm{u})dx$, where the x axis is perpendicular to the target surface, x_a is the position of the ablation front, x_r is the position of the rear surface, $\rho(x, y)$ is density distribution in the target, y_p and y_u are the perturbed and unperturbed y coordinates of the transverse direction, respectively, and $a(x)$ is the spatial perturbation amplitude for the target depth along the x axis, including the effect of feedthrough [1], and is written as $a(x) = a_a \exp[-k(x_\mathrm{a} - x)]$, where a_a is the perturbation amplitude at the ablation front. In our calculation of areal-density perturbation, the density distribution $\rho(x, y)$ is considered as mentioned above. Also, the areal-density perturbation $\delta\rho l$ for uniform target density ρ is approximated as $\delta\rho l \approx \rho[a(x_\mathrm{a}) - a(x_\mathrm{r})]$. Thus, the areal-density perturbations $\delta\rho l$ increase upon increasing not only the spatial amplitude $a(x)$ but also the target density ρ. The areal-density perturbation for PS and diamond for the high-foot pulse is at the same level as in Fig. 4.8(a). However, the spatial-perturbation amplitude of diamond should be smaller because the density of diamond is greater than that of PS during the observation time [as in Fig. 4.8(b)]. Here, the time variation of the target density is due to repeated shock propagation by laser pulses and expansion of the rear surface after shock breakout. Figure 4.8(c) shows the temporal evolution of the spatial perturbation at the ablation front as determined by PINOCO-2D for the three experimental configurations and for the low-foot PS as a reference. Both high-foot calculations

and the low-foot calculation indicate that the spatial perturbation of diamond is less than that of PS over the entire period of observation.

Figure 4.10 shows density-contour plots in the perturbation-wavelength range for diamond and polystyrene at 1.2 ns obtained by using PINOCO-2D. The front and rear ablation surfaces are defined to be at 1/e of the peak density. These positions describe spatial perturbations at the front and the rear ablation surfaces. The areal-density perturbations of the two-dimensional (2D) simulation are obtained from $\delta\rho l = \delta(\int \rho dx) = \int_{x_{\rm a}(y_{\rm p})}^{x_{\rm r}(y_{\rm p})} \rho(x, y_{\rm p})dx - \int_{x_{\rm a}(y_{\rm u})}^{x_{\rm r}(y_{\rm u})} \rho(x, y_{\rm u})dx$.

The basic hydrodynamic parameters (shock-breakout time, onset time of foil acceleration, and foil acceleration) must be confirmed to estimate the perturbation amplitude. The target acceleration for the high-foot diamond is slightly less than that for the PS because diamond foil is more massive. According to the 2D simulation, the accelerations of the PS and diamond due to the high-foot pulse are 3.9×10^{15} cm/s^2 and 2.4×10^{15} cm/s^2, respectively. The growth rate of the RTI of the spatial perturbation differs slightly between the three experimental configurations, as shown in Fig. 4.8(c). In the present work, we confirm by using side-on radiography that the experiment data for the acceleration trajectory are reproduced by the one-dimensional (1D) and 2D simulations (as in Fig. 4.4). The basic parameters (shock-breakout time and onset time of foil acceleration) are evaluated by simulations (Table 4.2). In addition, the experimental areal-density perturbation may be compared with 2D simulations [Fig. 4.8(a)]. By understanding the basic parameters, we can discuss the perturbations due to the irradiation nonuniformity between diamond and PS (see Sec. 4.2.5). Note that the spatial amplitude for diamond is less than that for PS just before the growth of the RTI. Conversely, the growth of the areal-density perturbation differs from that of the spatial perturbation. Note that the areal-density perturbation is not simply the target density multiplied by the spatial perturbation at the front surface because two-dimensional effects influence the spatial distribution of the density inside the foil.

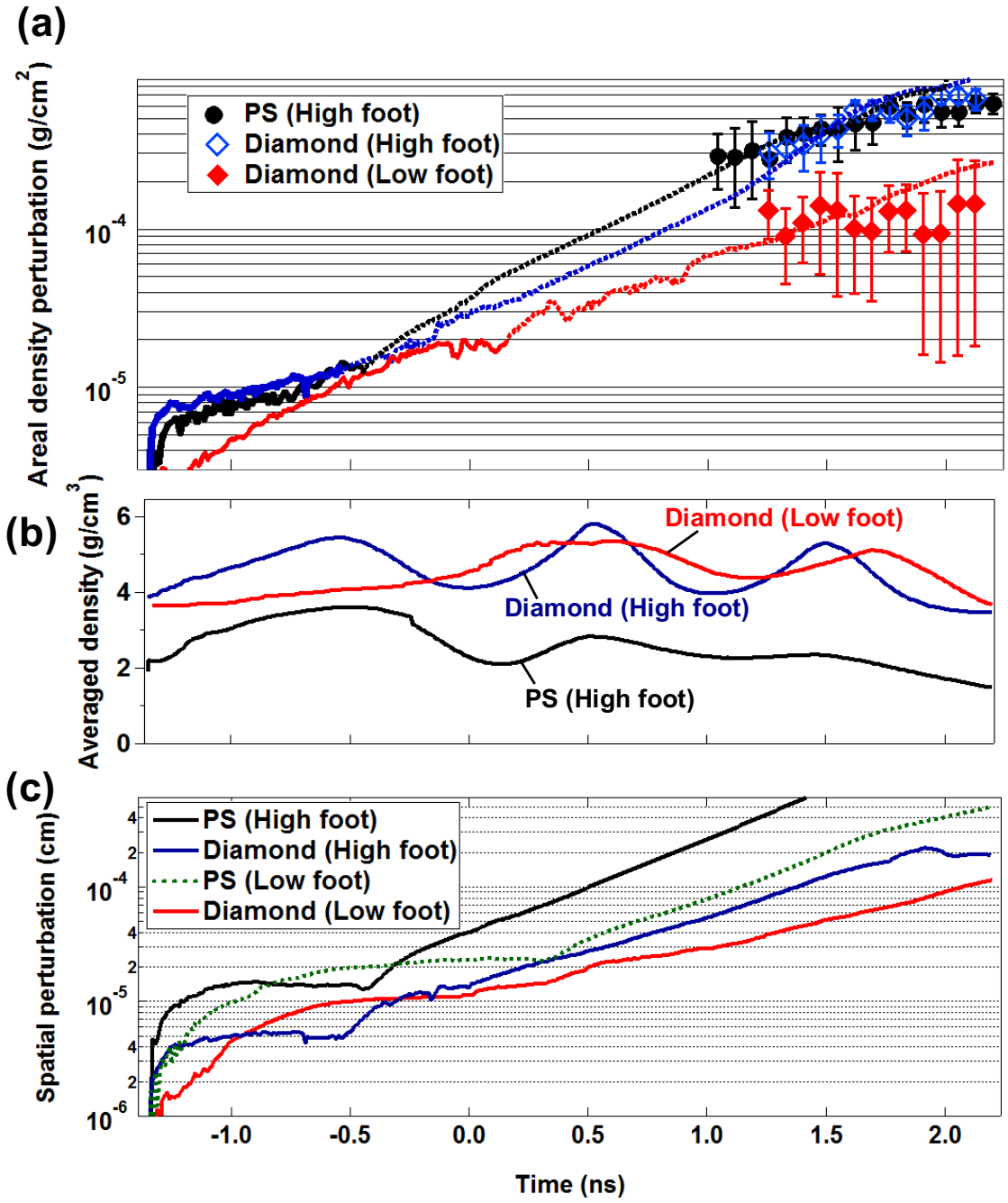

Figure 4.8: (a) Areal-density perturbation growth ($\lambda = 100\,\mu$m) for diamond and PS targets from experiments (symbols) and from the PINOCO-2D simulations for each experimental configuration prior to foil acceleration (solid curves) and after acceleration (dotted curve). (b) Averaged target densities calculated by 1D hydrodynamic simulation ILESTA-1D. (c) Spatial perturbation at the target surface obtained from PINOCO-2D simulation.

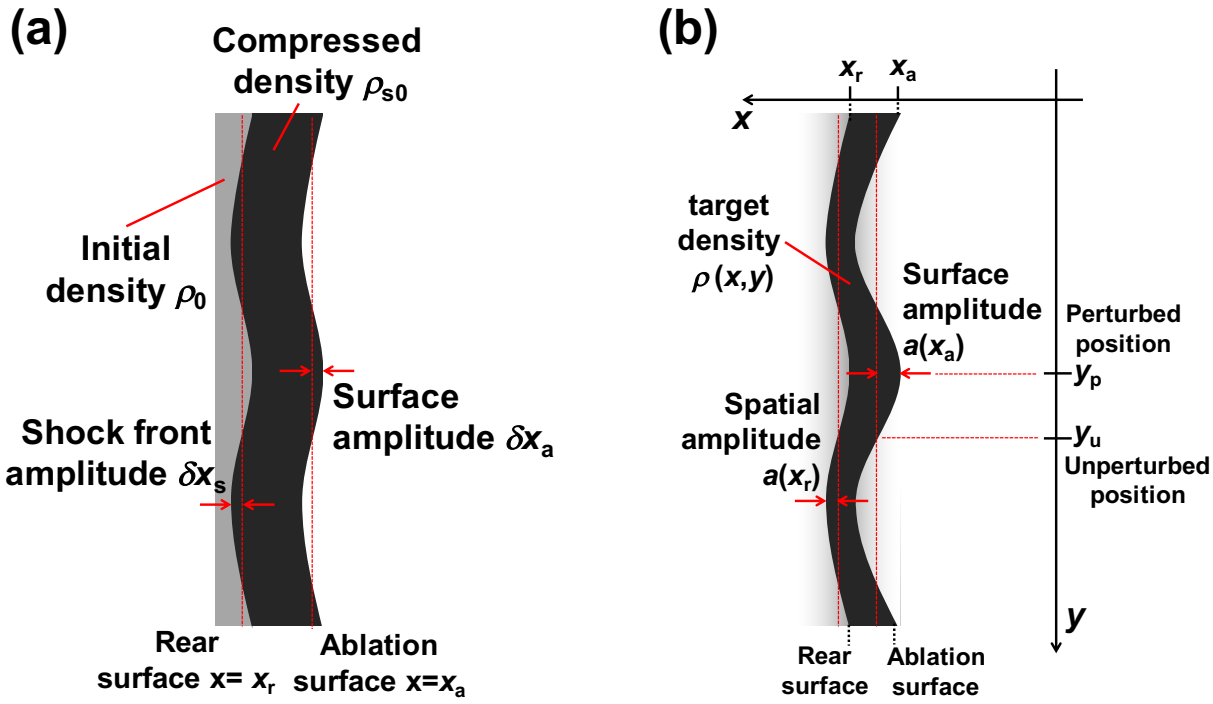

Figure 4.9: (a) Areal-density perturbation prior to shock breakout. (b) Schematic illustration of the target during the acceleration phase (after shock breakout).

Note also the difference in basic hydrodynamics between the data for the low- and high-foot diamond experiments. For the low-foot diamond data, the areal-density perturbation is smaller than that for the high-foot diamond data. This is partly because the duration over which the foil is accelerated is shorter for high-foot irradiation conditions. To correlate the basic hydrodynamics, the timing of the shock breakout and the onset of foil acceleration in the ILESTA-1D simulation for the three experimental configurations are shown in Table 4.2. Also, Fig. 4.8(a) shows the areal-density perturbation plots from the simulation before and after the foil acceleration (see solid and dotted curves).

On the other hand, the RTI growth rate obtained from PINOCO-2D with classical Spitzer-Härm thermal conduction is slightly greater than the experimentally obtained growth rates. This difference in growth rates is attributed to target heating by nonlocal electron thermal-energy transport, which reduces the RTI growth [43, 53] because PINOCO-2D does not consider nonlocal electron thermal-

Table 4.2: Timing of shock breakout and onset of acceleration for three experimental configurations obtained from ILESTA-1D simulation. The time origin (t = 0) is at the half maximum of the main laser pulse.

	PS (High foot)	Diamond (High foot)	Diamond (Low foot)
Shock breakout time	-0.53 (ns)	-0.75 (ns)	-0.07 (ns)
Acceleration onset	-0.44 (ns)	-0.53 (ns)	0.16 (ns)

energy transport in the Fokker-Planck equation. In our experiment, however, the perturbation wavelength is relatively high so that reduced RTI growth due to non-local electron thermal-energy transport would not be significant. Therefore, the experimental areal density almost agrees with the PINOCO-2D calculation even in the foil-acceleration phase.

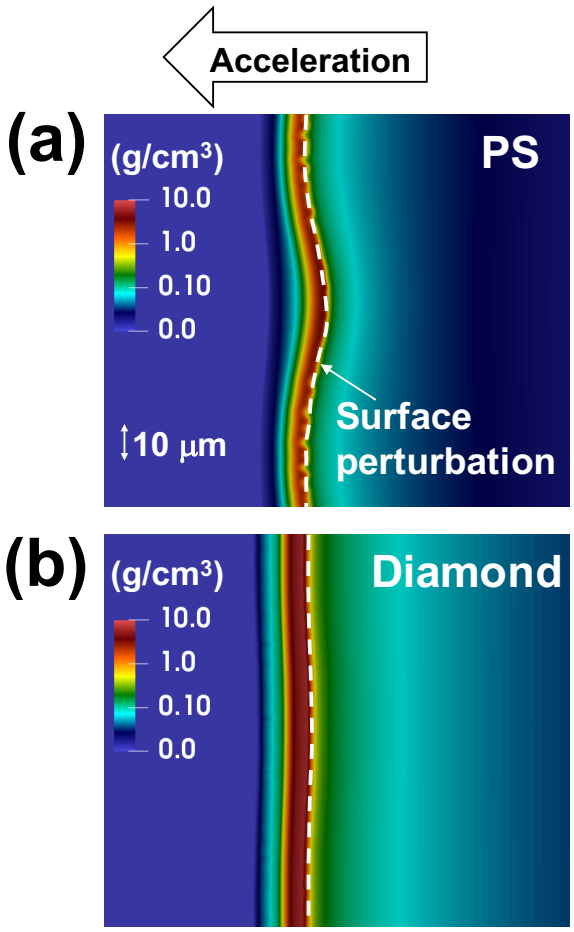

Figure 4.10: Simulated density contour plots at 1.2 ns for (a) high-foot PS and (b) high-foot diamond.

4.4.2 Analysis of imprint spatial amplitude with the PINOCO-2D simulation code

In our experiments, we measured the areal-density perturbation of the accelerated foils by amplifying the imprint perturbation due to the RTI with face-on x-ray backlighting because the imprint amplitude is generally too small to observe with conventional experimental techniques. Because we used two materials of different densities and masses, the areal-density perturbations at a given observation time should not be compared even for the same pulse shape because of the difference in a few important parameters, namely, acceleration, in-flight density, and foil thickness. Therefore, we discuss the spatial amplitude based on the results of the

PINOCO-2D simulation after we verify that the experimental results for the areal-density perturbation are consistent with the results of PINOCO-2D.

The 2D density contour plots obtained from PINOCO- 2D for both targets (high-foot PS and diamond) are shown in Fig. 4.11. The density plots show clearly that the imprint amplitude on diamond is less than that on PS. Also, the PS target is more compressed. Figure 4.12 shows the calculated spatial amplitude on the laser-irradiated surface as a function of time obtained from PINOCO-2D simulations. The calculations were carried out up to the shock-breakout time for each experimental configuration. The best comparison in this experiment is high foot PS and high foot diamond. The shock-compressed density ρ_{s0} for high-foot diamond up to the shock-breakout time is 1.5 to 2.0 times larger than that for high-foot PS. For a denser material, the imprinted surface perturbation is smaller, as shown by Eq. (4.1). Furthermore, the average difference between shock velocity and fluid velocity behind the shock front (i.e., $v_{s0} - v_{a0}$) for diamond is about 1.8 times greater than that for high-foot PS.

On the other hand, the areal-density perturbation prior to the shock-breakout time (t < -0.5 ns) is slightly greater for high-foot diamond, as shown in Fig. 4.8(a). As illustrated in Fig. 4.9(a), the areal-density perturbation $\delta\rho l$ prior to shock breakout may be approximated by $\delta\rho l = \int_{x_a}^{x_r} \rho(x)|\partial a(x)/\partial x|dx \approx \rho_s(\delta x_a - \delta x_s) + \rho_0\delta x_s$, where ρ_s is the compressed target density, δx_a is the spatial amplitude of the ablation front, δx_r is the shock-front amplitude, and ρ_0 is the initial density. The target density and the amplitude of both the ablation front and the shock front should be considered to calculate the area-density perturbation. For example, at t =1.1 ns, the compressed-target density ρ_s and initial target density ρ_0 for diamond are 4.41 and 3.51 g/cm^3, respectively. On the other hand, the compressed density ρ_s and initial target density ρ_0 for PS are 2.90 and 1.06 g/cm^3, respectively. The calculated spatial amplitude δx_a on the ablation front for diamond and PS is 0.048 and 0.126 μm, respectively.

Because the shock-propagation distance is much smaller than the perturbation wavelength, the shock-front amplitude δx_s may be approximated by δx_a. Thus, the areal-density perturbation prior to shock breakout depends strongly not only

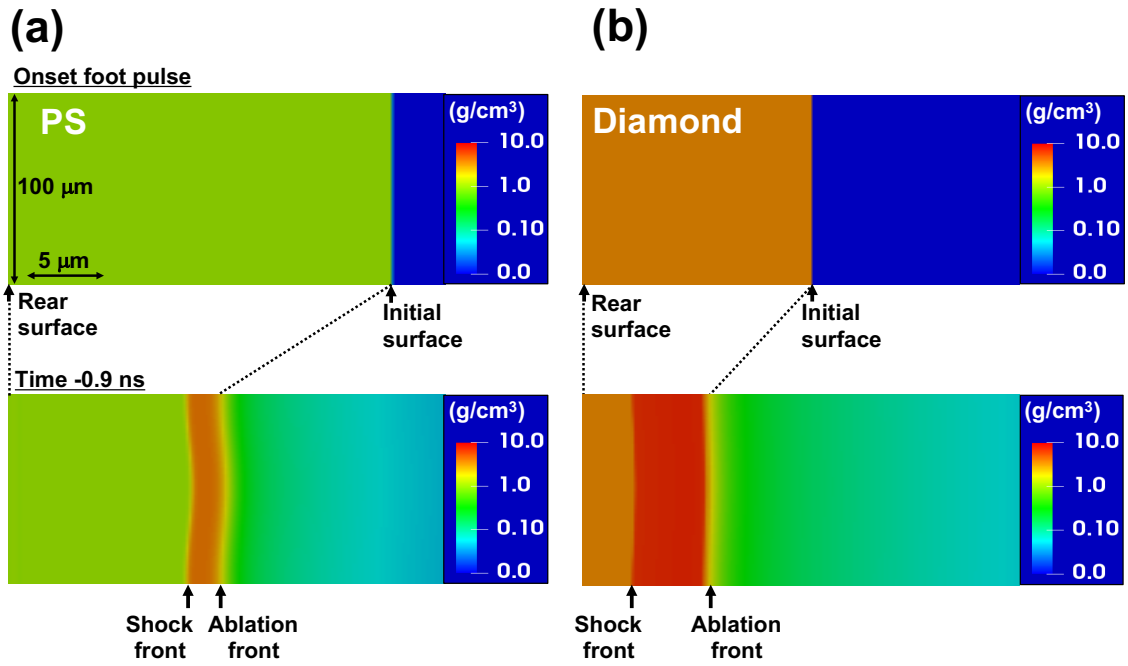

Figure 4.11: Simulated density contour plots at onset of the foot pulse and at 0.9 ns for (a) high-foot PS and (b) high-foot diamond.

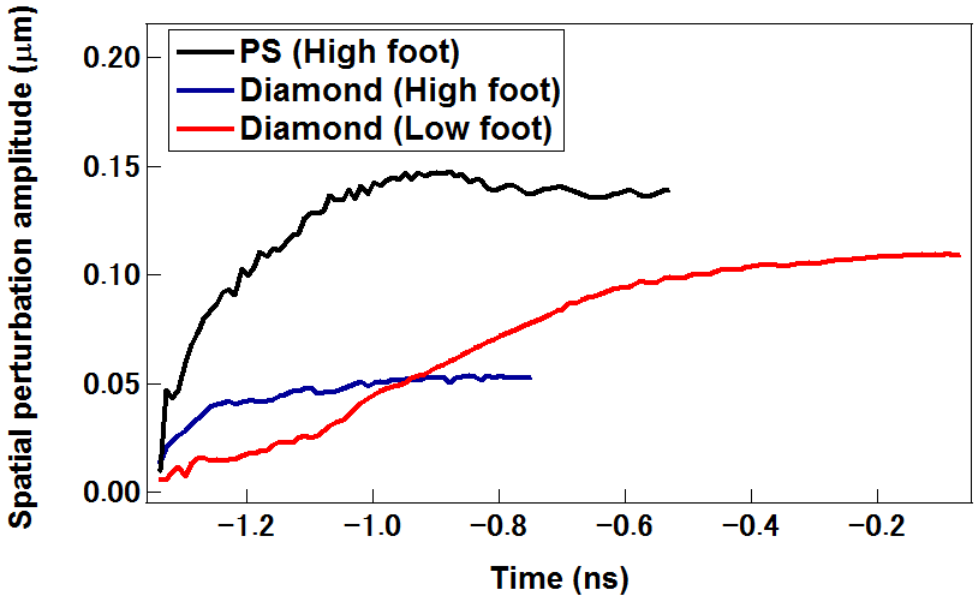

Figure 4.12: Temporal evolution of spatial perturbation at the target surface obtained from PINOCO-2D simulation.

on the spatial amplitude $\delta x_{\rm a}$ ($\sim\delta x_{\rm s}$) but also on the initial density ρ_0. The simulations show that the spatial amplitude at the ablation surface for high-foot PS is about two to three times greater than that for high-foot diamond. Conversely, the initial density of diamond is $\sim$3.5 times greater than that of PS. Therefore, the parameters are all consistent in explaining why the areal-density perturbation for high-foot diamond is slightly greater than that for high-foot PS.

As shown in Section 2.4, the standoff distance is also a key parameter for determining the imprint amplitude, which should also be considered. Figures 4.14(a) and 4.14(b) show the temporal evolution of the target compressibility in the shock-compressed region and the standoff distance obtained from ILESTA-1D, respectively, for the three experimental configurations. The compressibility is $\rho_{\rm s0}/\rho_0$, where $\rho_{\rm s0}$ is the averaged density of the shock-compressed region and ρ_0 is the initial density. As shown in Fig. 4.14(a), the compressibility for PS is 3.4 at the shock-breakout time, whereas the compressibility for high-foot diamond is $\sim$1.5. For high-foot conditions, the shock pressure is about 530 GPa, at which point the diamond remains solid [37] but is beyond the elastic-plastic transition pressure. As shown in Fig. 4.14(b), the stand-off distances for high-foot PS and diamond are very similar, which means that the imprint perturbation for the high-foot condition is definitively mitigated by the differences in density and compressibility, which are strongly related to the EOS between the two target materials. In our dataset, we have no low-foot PS experiment data to compare with the low-foot diamond data. The low-foot PS simulated by PINOCO-2D indicates that exactly the same correlation exists between low-foot PS and low-foot diamond as in the high-foot dataset.

From the point of view of practical ICF target design, the high-density ablator should be thinner to maintain the acceleration. Therefore, the spatial imprint amplitude should be compared between the same-mass conditions at the shock breakout times. In our case, because 13-μm-thick diamond foil is equivalent to 43-μm-thick PS foil, the spatial amplitude should be compared with these two conditions at their shock-breakout times. As seen in Fig. 4.12, the spatial amplitude of both targets (high-foot diamond and high-foot PS) starts to saturate prior

to shock breakout because of the standoff distance. Figure 4.13 show the spatial perturbation plots for PS (43 μm^t), PS (25 μm^t)) and diamond (13 μm^t) on the high-foot pulse. From PINOCO-2D, the spatial imprint amplitude for high-foot PS at shock breakout is also approximately 30% of that for high-foot diamond at its shock breakout time.

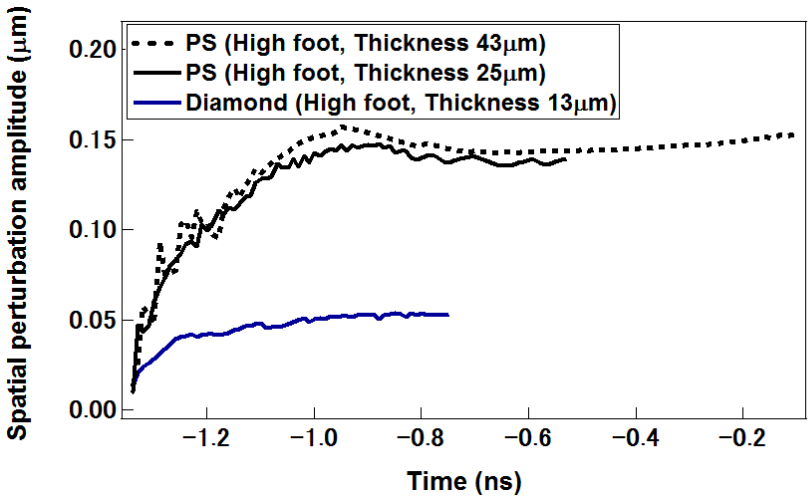

Figure 4.13: Temporal evolution of spatial surface perturbation until the shock breakout timing with the PINOCO-2D simulation code.

For low-foot diamond, the standoff distance is much less than that for high-foot diamond, as shown in Fig. 4.14(b). However, the imprint amplitude for low-foot diamond is the lowest at very early times. The shocked pressure for low- foot diamond is about 110 GPa, which means that the diamond pressure remains below the elastic-plastic transition pressure. As shown in Fig. 4.14(a), the compressibility for low-foot diamond is very small because of its material strength, whereas the pressure on high-foot diamond exceeds the elastic-plastic transition pressure. This implies that the reduction is effective because of the lower compressibility below the elastic-plastic transition pressure even though the standoff distance is smaller for low-foot diamond [see Fig. 4.14(b)]. The imprint amplitude for low-foot diamond over- takes that for high-foot diamond at about 1.0 ns because the standoff distance increases more rapidly with time for the high-foot conditions. Note that the 2D simulation result is consistent for low- and high-foot diamond although the code

does not include a precise model of material strength below the elastic limit. This is attributed to the pressure perturbation (imprint amplitude) being so small that effects such as shear stress are negligible. Thus, the analysis of imprinting with one-dimensional compressibility is valid also for the solid phase.

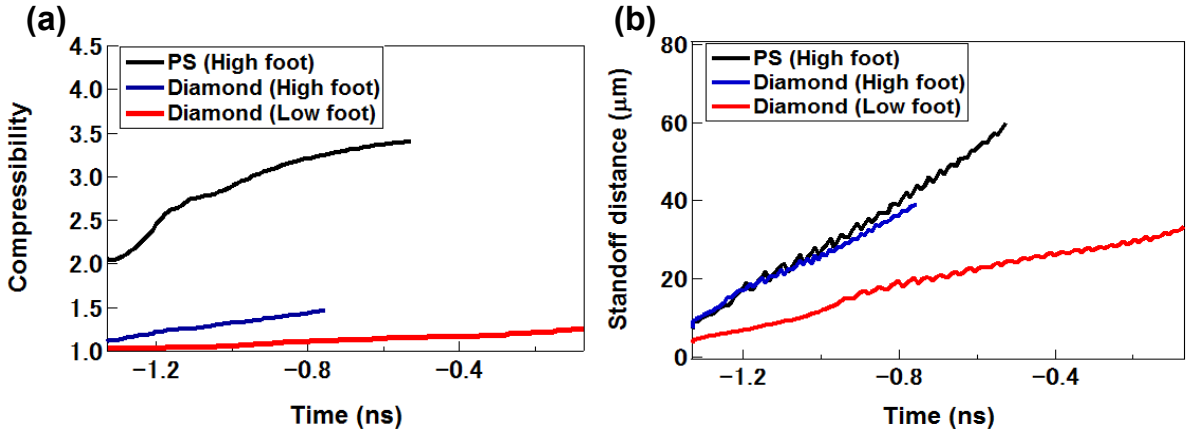

Figure 4.14: (a) Compressibility as a function of time up to shock breakout obtained from ILESTA-1D simulation. (b) Temporal evolution of the standoff distance obtained from ILESTA-1D simulation.

We do not have data for low-foot polystyrene control shot in hand. However, there are a lot of previous PS data on the similar low-foot experimental condition, which had been benchmarked by analysis with the 2D hydrodynamic simulation and simple incompressible model [19,21,22]. As a reference, Fig. 4.15(a) and (b) shows the calculation with the PINOCO-2D simulation code for the low-foot conditions. The calculations between two low foot conditions (diamond and polystyrene) also shows reasonable difference as seen in comparison of the high foot conditions. Figure 4.16 shows the temporal evolution of (a) compressibility of the targets at the shock-compressed region and (b) stand-off distance calculated with the ILESTA-1D simulation code for low foot conditions. In that case, the difference in compressibility between diamond and PS is around factor of 2. On the other hand, the stand-off distance for the low-foot PS and diamond is very similar as in Fig. 4.16(b).

These comparisons between the low-foot diamond and the low-foot PS are on exactly same interpretation as shown in the comparison between the high-foot

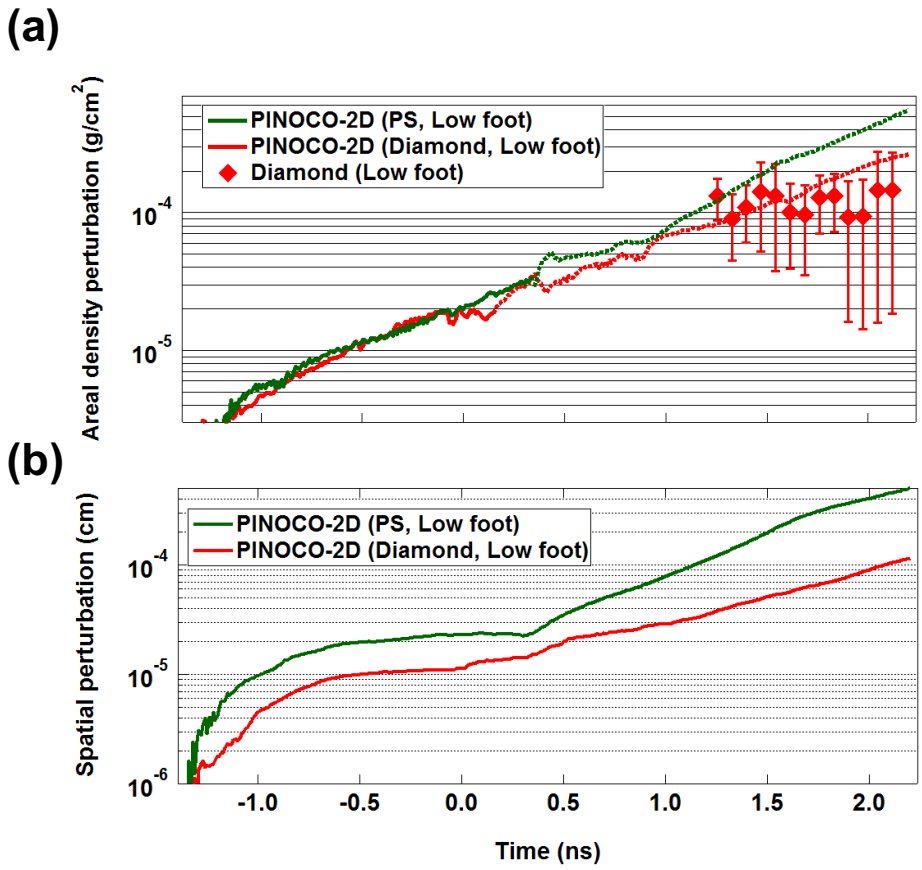

Figure 4.15: (a) Areal-density perturbation amplitude from the experiment (symbols), and from the PINOCO-2D calculations for diamond and PS on low foot condition prior to the foil acceleration (solid curves) and after the acceleration (dotted curve). (b) Temporal evolution of spatial perturbation amplitude on the target surface with the PINOCO-2D simulation code for low-foot diamond and PS.

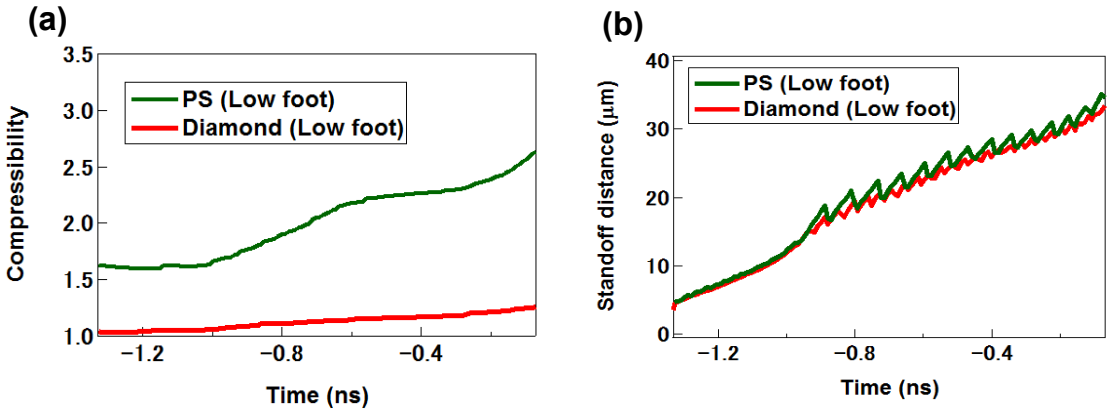

Figure 4.16: (a) Calculated compressibility and (b) Temporal evolution of stand-off distance by the ILESTA-1D simulation code in the foot pulse regime.

dataset.

The previous works on high-density carbon (HDC) report that solid or partially melted conditions might provoke distortions of the shock front due to anisotropy in the sound velocity in crystals [54, 87]. Thus, microstructures would be generated below the fully melted condition, which constitute a possible seed for hydrodynamic instability. In the first shock of over 6 Mbar, the effect of microstructures is at an acceptable level for HDC [54]. However, a strong shock precludes a low-fuel adiabat and high compression during ICF. Although the anisotropy of HDC is indeed a concern for ICF, recent experiments at the National Ignition Facility (NIF) have suggested that this can be mitigated by using the laser pulse profile to allow low adiabats and high compression [84].

There are possibilities that strength effects and melt issues could be affecting the observed perturbation growth or seed to instabilities. In this study, there is little influence of the microstructures due to grains and the anisotropic sound velocity in the crystal because the target is single-crystal diamond. Actually, the results of the two-dimensional hydrodynamic simulation are consistent with the experimental results. Therefore, the density and compressibility, that is, the material EOS, are prominent factors for laser imprinting in many differences between diamond and PS.

The most recent experimental investigation on NIF facility suggests that hydrodynamic fuel/core mixing in the final phase is the most crucial factor for fusion ignition. Successful fusion ignition requires to minimize the mix width at the deceleration phase. The mix width is rear surface spatial perturbation of the shell that is seeded by feedthrough from the front surface spatial perturbation growth. The whole process about the perturbation transfer is strongly depends on its target design including laser irradiation condition, and on scheme of ignition (central hot spark ignition, fast ignition, shock ignition, and so forth). The diamond ablator would reduce laser imprinting, but the effect of feed-through to the inner shell surface might be large in use of thinner diamond capsules. The implosion performance of diamond capsules in direct-drive ICF experiments should therefore be discussed in future works.

4.5 Conclusion

In conclusion, this study clarify herein how density and compressibility affect laser imprinting by using diamond as a candidate stiff-ablator material for ICF targets. The effect of density and compressibility is verified both by using 2D hydrodynamic simulations and by experiments. Laser imprinting on high-foot PS is compared with the same on high-foot diamond, and the same is done for high- versus low-foot diamond. Imprinting amplitude due to non-uniform laser irradiation (average intensity 4.0×10^{12} (low-foot)-5.0×10^{13}(high-foot) W/cm^2, non-uniformity $\sim$10%) differs shows difference by a factor of 2-3 between diamond and PS foils. For high-foot conditions (both diamond and PS), the difference in imprinting amplitude is mainly due to the difference in density and compressibility. Conversely, the difference in imprinting amplitude for low-foot diamond is influenced by material strength (elastic-plastic transition) and by the standoff distance. The 2D simulation well reproduces the measurements of areal-density perturbation, which reveals the effect of density and compressibility on laser imprinting. The advantage of low-compressibility materials in ICF target design is that such a scheme may be combined with another suppression scheme by enhancing the standoff distance, as was proposed in previous works. For example, the mitigation method involving high-Z material coatings is easily coupled with the present scheme. By combining these schemes, both short- and long-wavelength laser imprinting may be mitigated. The physics of material stiffness affecting laser irradiation is also very important, not only for ICF-target design but also for general questions on laser-matter interactions for laser processing, laser peening, and other applications.

Chapter 5

Perturbation structure on diamond foil due to nonuniform irradiation

5.1 Introduction

In direct-drive inertial confinement fusion (ICF), a fuel capsule is irradiated directly with laser light [1,11]. The capsule consists of a cryogenic layer of deuterium and tritium (DT) frozen onto the inner surface of a spherical shell of ablator material. Laser imprinting occurs on the surface of ablator material due to irradiation nonuniformity [19, 78]. Spatial perturbation due to laser imprinting is amplified by Rayleigh-Taylor instability during the shell acceleration phase [21, 79]. The grown perturbation could disrupt the shell and cause mixing of fuel [15]. On the direct drive scheme, laser imprinting is one of the most important issue because imprinting perturbation on the capsule surface degrade symmetry of the target implosion and target performance as a result. Level of laser imprinting depends on the parameter of ignition conditions (neutron yield and target areal-density) in ICF experiments [62]. Many previous investigations have striven to mitigate laser imprinting by smoothing the effective laser irradiation nonuniformity by using low-density foam ablators [24, 25, 28, 29], radiation with high-Z coatings [30, 31, 80, 81],

" picket " pulse irradiation [32], or soft-x-ray pre-irradiation [33]. In previous our work, it has founded that stiffer and denser materials reduce the laser imprinting [64]. Among the stiff materials, diamond is the most probable candidate as an ablator material for direct-drive ICF targets [64]. The advantage of stiff materials in ICF target design is that such a scheme may be combined with another suppression scheme by smoothing the effective laser irradiation nonuniformity. The mitigation method involving high-Z material coatings is easily coupled with the present scheme. Also, in x-ray indirect drive implosions, High Density Carbon (HDC) is a leading candidate as an ablator material because it has good potential to reach a high implosion velocity and high stagnant pressure due to its high density and optimal X-ray opacity [54, 69]. Indirect-drive implosions with a high-density carbon (HDC) capsule are being conducted at the National Ignition Facility (NIF) [54, 82–86].

In the case of diamond, the shock physics is further complicated by its tightly bound crystalline nature in combination with an extremely high melting temperature, and the existence of another high pressure solid phase of carbon called BC8 [57, 58]. Specifically, Solid or partially melted diamond ablator during the ICF implosion can provide microstructures that seed hydrodynamic instabilities [54, 87, 88]. The strong shock that completely melts the diamond or keeping that in the coexistence regime is necessary in order to suppress the distortions of the shock front due to anisotropy in the sound velocity in crystals [54]. The anisotropy of diamond is indeed a concern for the ICF application, but recent experiments at NIF have demonstrated that this can be mitigated by using the right laser pulse profile [84]. Although the diamond with stiff characteristic becomes candidate as ablator materials, brittle materials such as diamond can easily cleave due to dynamic stress on a certain crystallographic plane [89, 90]. In the case of direct-drive inertial confinement fusion, in particular, the nonuniform laser irradiation would lead to local fracture on brittle material surface. However, so far, little research has been done on solid strength issues in laser imprinting.

In this chapter, the Influences of solid strength to conditions of dynamic stress on the laser imprinting are reported. The understanding of the solid strength in

the laser irradiation is particularly important in the basic physical process of the laser material processing and early phase of the inertial confinement fusion. We carried out measurements of areal-density perturbation due to non-uniform irradiation with face-on x-ray backlighting method that is standard technique for hydrodynamic instability experiments [19, 21]. The areal-density perturbation data, their analysis and calculations of areal-density perturbation amplitude with two-dimensional hydrodynamic simulation code PINOCO-2D [46] are presented. We analyzed the dependence of irradiation nonuniformity and high-Z coating on areal-density perturbation for diamond foils. All the materials from the experiment and simulation suggest that the solid strength issues on the fracture affect the laser imprinting.

5.2 Experimental conditions

The experiments were conducted using the GEKKO-XII Nd: glass laser facility at the Institute of Laser Engineering, Osaka University [39]. Experimental setup and typical stacked pulse shape are shown in Fig. 4.1 in section 4.2.1. The diamond foils were irradiated with the second harmonic light (Wavelength: 0.527 μm) at an incident angle of 37.4°. The stacked pulse with time delays between the beams consists of one beam for the foot pulse at an intensity of $\sim 4.0 \times 10^{12}\,\mathrm{W/cm^2}$, and a subsequent two beams for the main drive pulse at an intensity of $\sim 10^{14}\,\mathrm{W/cm^2}$ (see Fig. 4.1(b)). The laser pulse was focused on to the diamond foil to a spot with a size of ∼600 μm (FWHM). The averaged intensities, I_0, of the foot pulse were $\sim 4 \times 10^{12}\,\mathrm{W/cm^2}$. The peak intensity of the main drive was $\sim 10^{14}\,\mathrm{W/cm^2}$. Intensity modulation δI of the foot pulse was introduced using a grid mask placed in front of the focusing lens, whereas the main drive was kept uniform. Figure 5.1(a) show spatial pattern of the foot pulse at the target surface. Foot pulse have the irradiation nonuniformity (perturbation intensity δI/average intensity I_0 ∼40 %), in order to generate the laser imprinting. The wavelength λ of the perturbation intensity is ∼100 μm as in Fig. 5.1(b). The higher spatial harmonic components (wavelength: 20∼50 μm) in the imprint pulse were less than 10 % of the funda-

mental wavelength (as in Fig. 5.1(b)). Perturbations were observed on the target via amplification due to the RTI growth using the main drive beams because the imprinted perturbations were typically too small for detection.

The targets comprised single-crystal diamond foils (Type-Ib, density: 3.51 g/cm^3) with a thickness of 13-16 μm. The surface orientation of the single-crystal diamond was (100) plane. The target foils were coated with Al of 0.05 μm thickness as a shield for shine-through inside of the foils in very early irradiation timing [59]. Some of the diamond foils were surface coated with Cu of 0.1 μm thickness in order to compare the radiation effect that smooths the effects of irradiation non-uniformity, which is descried following sections.

The areal-density perturbation growth was measured using a face-on x-ray back-lighting technique. A Backlight target (Zn) was irradiated to generate $\sim$1.53 keV quasi-monochromatic x-rays coupled with a 6 μm-thick aluminum filter. Temporal evolution of the transmitted x-rays from the Zn backlighter through a diamond or PS foil was imaged through a slit (10×50 μm^2) onto the photocathode of an x-ray streak camera. The total magnification was $\sim$25.9$\times$, and the temporal resolution of the x-ray streak camera was 143.1 ps. The spatial resolution was measured using a backlit grid image that took into account the analysis of the areal-density perturbation. The resolution function of the entire diagnostics system is given by the sum of two Gaussian functions as $R(x) = [1/(1+\alpha)]\exp[-\mathrm{x}^2/(2\sigma_1^2)] + \alpha\exp[-\mathrm{x}^2/(2\sigma_2^2)]$, where $\alpha = 0.242, \sigma_1 = 4.881\,\mu\mathrm{m}, and\ \sigma_2 = 11.303\,\mu\mathrm{m}$.

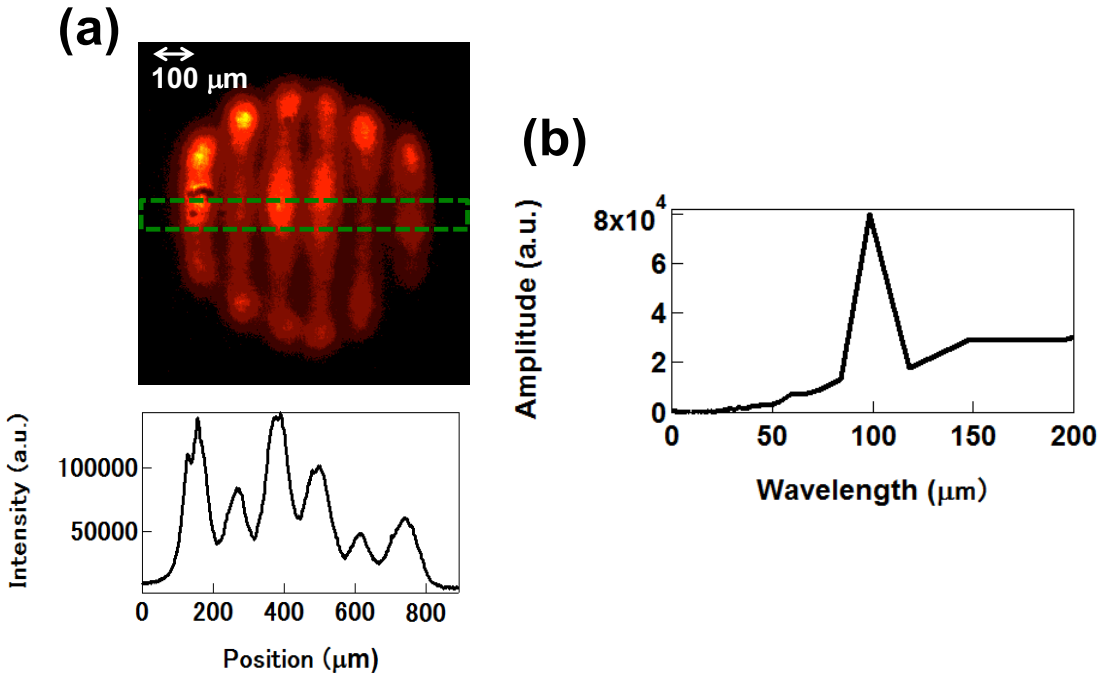

Figure 5.1: (a) Spatial pattern of the foot pulse at the target surface. (b) Modulation wavelength spectrum of the irradiation non-uniformity.

5.3 Experimental results by areal-density perturbation growth with face-on backlighting method

Examples of raw streaked backlit images of the diamond and diamond with Cu coating (0.1 μm^{t}) foils for the foot pulse intensity $\sim 4 \times 10^{12}$ W/cm^2 are shown in Fig. 5.2. The time origin (t = 0) was set as the time when the onset of the main drive pulse reached the half maximum, as shown in Fig. 4.1 in section 4.2. Figure 5.2 also shows the lineouts for these targets. Time-integrated lineouts were obtained for temporal resolution duration ($\sim$ 140 ps). The areal-density perturbations were obtained by fitting the convolutions of the resolution functions and sinusoidal perturbation functions to the raw lineouts, taking into account the x-ray absorption coefficient (at $\mu = 660.9$ cm^2/g) for diamond. From the lineouts for the diamond with the irradiation non-uniformity $\sim$10 %, the typical sinusoidal like perturbations of the RTI growth can be seen. On the other hand, the backlit

image for the diamond with the large irradiation non-uniformity $\sim$ 40 % indicates the non-sinusoidal perturbation with sharp shape, which is different from usual single mode perturbation growth of the diamond for laser irradiation noniniformity $\sim$10 % [64]. When there is high-Z coating, the sharp shape structure disappears on the x-ray transmission distribution. From the lineouts for the diamond with Cu coating foil, the typical sinusoidal like perturbations of the RTI growth can be seen in Fig. 5.2.

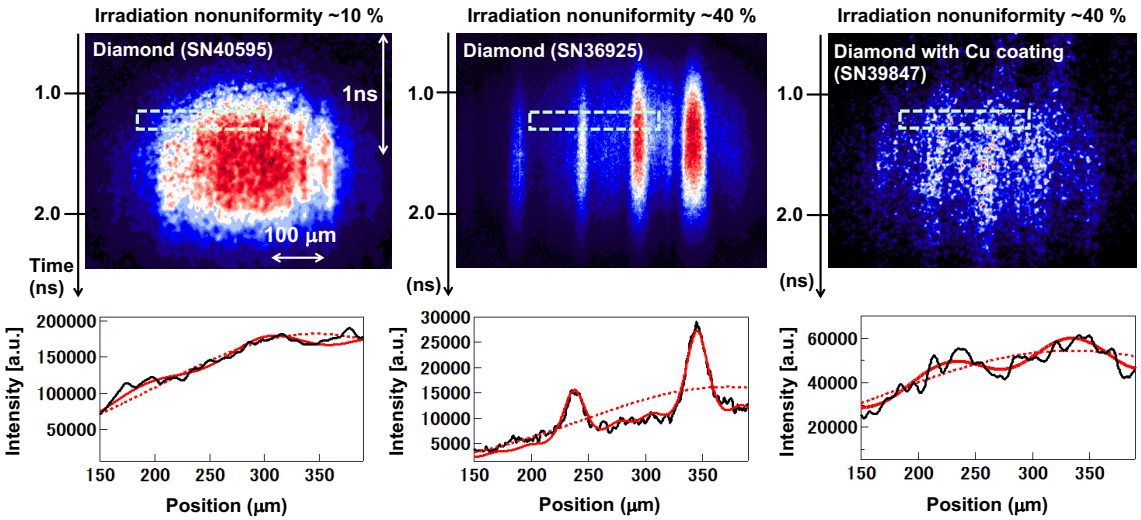

Figure 5.2: Raw streaked images for the face-on x-ray backlit single-crystal diamond and diamond with Cu coating foils for the foot pulse intensity $\sim 4 \times 10^{12}$ W/cm^2. All the lineouts (black lines) are about time 1.2 ns. Red lines are curve fitted curves for each profile. Raw data for diamond with irradiation nonuniformity $\sim$10 % is shown in [64].

Figure 5.3 presents the analysis of the temporal evolution of the areal-density perturbations for the diamond with laser irradiation noniniformity $\sim$10 % and $\sim$40 % with the fundamental (λ:100 μm) and second harmonics (λ:50 μ m) perturbation plotted. In previous our work [64], the diamond with irradiation noniniformity $\sim$10 %, it was founded that the fundamental perturbation generates which is well reproduced by the two-dimensional radiation hydrodynamic simulation code PINOCO-2D [46] (see Fig. 5.3 (a)). On the other hand, for the diamond with large irradiation noniniformity $\sim$40 %, second harmonic generation of the

same level as fundamental component was observed very early in time before the foil acceleration time ∼0.75 ns (as in Fig. 5.3(b)). Both fundamental and second harmonic components individually grow with their growth rate. Here, the onset of foil acceleration is evaluated by simulation. We confirmed separately by using side-on radiography that the experimental data for the acceleration trajectory are well reproduced by PINOCO-2D simulations (see section 4.2.2). For the diamond with large irradiation nonuniformity ∼40 %, it is not typical for imprinting generation and amplification, compared to some previous studies of single spatial mode experiments on direct-driven planar targets4,6. In radiation hydrodynamic simulation, PINOCO-2D do not reproduce experimental result for the diamond with large irradiation nonuniformity (Fig. 5.3 (b)). We estimate there are solid-strength issues due to large pressure perturbation as shown in following Discussion section, which do not include the simulation code. Figure 5.3(c) presents the temporal evolution of the areal-density perturbations for diamond with Cu coating in the irradiation noniniformity ∼40 %. The fundamental perturbation grew with time and second harmonic perturbation is clearly smaller than that of fundamental component in time after the foil acceleration time 0.5 ns. As a result, a sinusoidal like perturbation occurs as shown in Fig. 5.2(c). For the diamond with Cu coating, PINOCO-2D simulation result is in reasonably good agreement with the experimental result. However, details of the high-Z coating effect on the temporal evolution of the spatial ablation structure and density distribution inside target are not known yet. In single spatial mode experiment and simulation studies, the future works are to better understand the effects of high Z coating on the ablation structure mechanism from imprint generation to hydrodynamic instability.

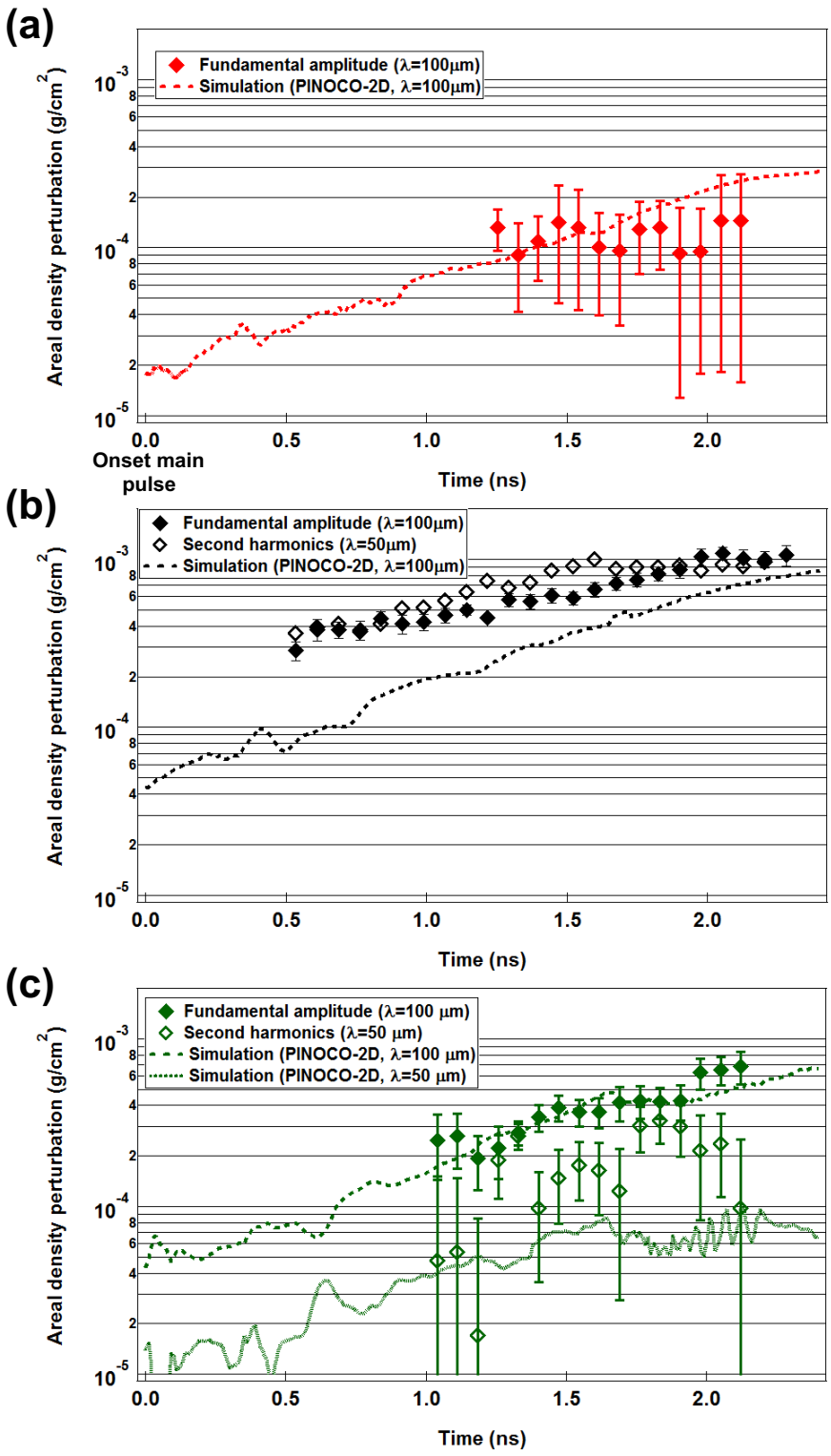

Figure 5.3: Areal-density perturbation growth for single-crystal diamond targets from experiments (symbols), and from the PINOCO-2D calculations simulations (dotted curve) for each experimental configuration: (a) Diamond on nonunifomity ∼10 % [64]. (b) Diamond on nonunifomity ∼40 %. (c) Diamond with Cu coating on nonunifomity ∼40 %.

5.4 Discussion

When irradiation non-uniformity is large, 2D hydrodynamic simulation do not reproduce experimental results on the diamond foil. In interpretation of these results, we consider that material-strength would influence the laser imprinting. In shock compression experiments, the Hugoniot elastic limits (HEL) of diamond are measured to be 80.1 (± 12.4), 80.7 (± 5.8) and 60.4 GPa (± 3.3) for $< 100 >$, $< 110 >$, and $< 111 >$ orientations, respectively [37]. The elastic yield strength of diamond inferred from these measurements is 75 (± 20) GPa [37]. In our experiments, pressure perturbations due to foot pulse produce the non-uniform stress which are tensile stress and shear stress into the diamond foils. In the local area beyond HEL, slip and fractures which are not considered in the hydrodynamic simulation code occurs primarily on crystal planes [37,61]. As a result, non-sinusoidal perturbation would generate at the diamond surface. Figure 5.4 show density and pressure distribution by PINOCO-2D near the ablation front at the early irradiation time. When irradiation nonuniformity is large, pressure region exceeding the HEL or (elastic yield strength) of diamond partially appears conspicuously as in Fig. 5.4(a). On the other hand, in the case of small irradiation nonuniformity (or generation of typical sinusoidal-like perturbation), the area corresponding the HEL produces over the entire surface (Fig. 5.4(b)).

The influence of solid strength using a thin high Z coating that smoothes the effects of irradiation non-uniformity or the pressure perturbation has also been investigated. In multi spatial mode experiments [30, 31, 80], under initial low-intensity laser irradiation, the high-Z ablation layers expand and convert the initial nonuniform laser flux into uniform x-ray radiation that uniformly ablates and accelerates the target. As the laser pulse shifts to higher intensities, the high-Z material burns away, and the target transitions to pure direct drive [30, 31, 80]. By this method, indirect x-ray drive is used during the nonuniform start-up phase while direct drive is employed during the remaining more uniform phases of the drive pulse. Figure 5.4(c) show pressure distribution due to foot pulse for diamond with Cu coating. Pressure perturbation of the foot pulse can be reduced by high-Z

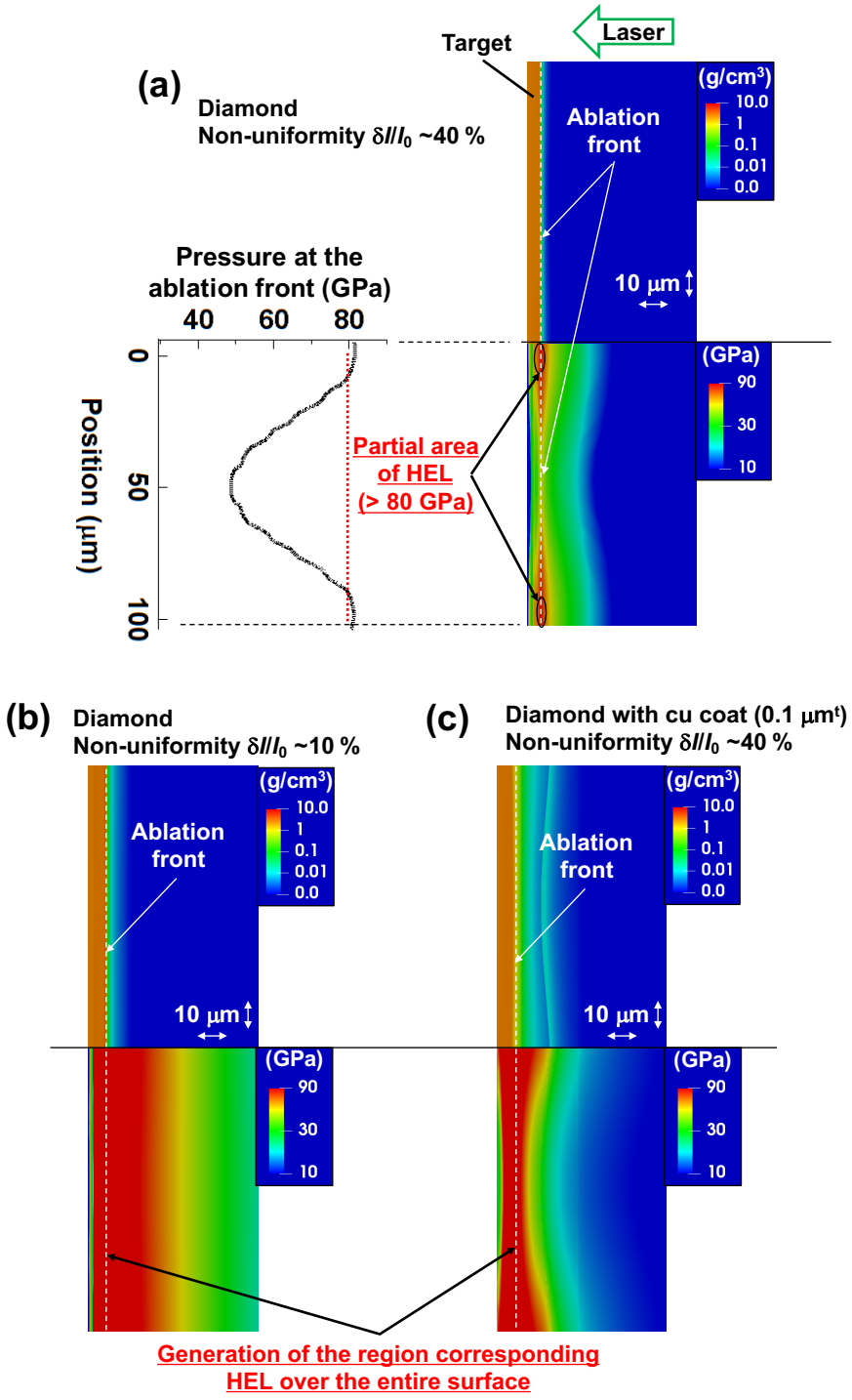

Figure 5.4: Simulated density and pressure contour plots for diamond foils at the time -0.95 ns: the (a) Nonuniformity∼40 %. (b) Nonuniformity∼10 %. (c) Nonuniformity∼40 % with Cu coating.

coating than that of only diamond. That means local fracture at the surface would be difficult to occur. As shown in Fig. 5.2, the crack-like structure which is non-sinusoidal perturbation disappears by thin high-Z layers. When there is high-Z layers, influence of material strength would be suppressed. Also, Figure 5.5 shows the temporal evolution of areal-density perturbation (fundamental component) for diamond with Cu coating and polystyrene (thickness 25 μm^{t}) targets. Under the same experimental conditions, the areal-density perturbation for diamond with Cu coating is smaller than that of polystyrene. That suggest the combination of diamond and high-Z coating are effective for suppression to the surface perturbation and the solid-strength issue due to large irradiation non-uniformity.

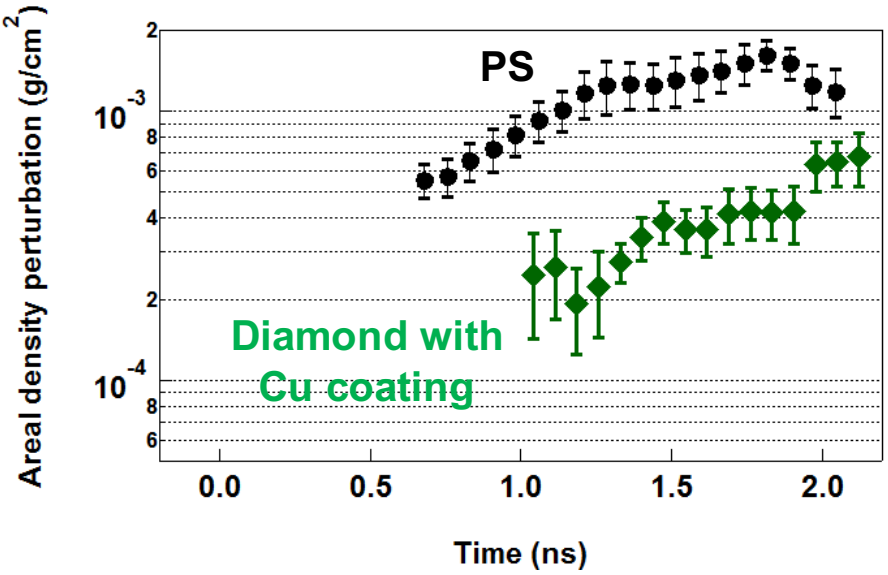

Figure 5.5: Areal-density perturbation growth (λ = 100 μm) for diamond with Cu coating and polystyrene (PS) targets. In experimental conditions, irradiation nonuniformity of the foot pulse is ~40 % and foot pulse intensity is $\sim 4 \times 10^{12}$ W/cm^2.

As mentioned above, in single-crystal diamond (surface orientation, (100) plane), experimental results and 2D simulations show that spatial pressure perturbations that partially exceed the elastic limit develop into solid strength issues on surface perturbation. Single-crystal diamond for surface orientation of (100) and (110) plane have relatively large strength of the elastic limit ($\sim$ 80 GPa) [37]. It is con-

sider that influence of solid strength appears also in polycrystalline diamond surface under the same experimental conditions. The figure 5.6 shows the x-ray backlit images of single crystal and polycrystalline diamond under the same experimental conditions (Nonuniformity$\sim$40%, average foot pulse intensity $\sim 4.0\times10^{12}\,\mathrm{W/cm^2}$). Sharp-structured non-sinusoidal perturbations generate on each diamonds at about the same time and they grow. The temporal evolution of the areal-density perturbation for polycrystalline and single-crystal diamond is shown in Fig 5.7. The difference in areal-density perturbation between single-crystal and polycrystalline diamond does not appear remarkably. The strength of single-crystal and polycrystalline diamond are comparable under high strain-rate dynamic loading [37, 60] and it can be considered that the difference whether the pressure perturbation partially exceeds the elastic limit or not is related to the perturbation structure on both single and poly-crystal diamond surface.

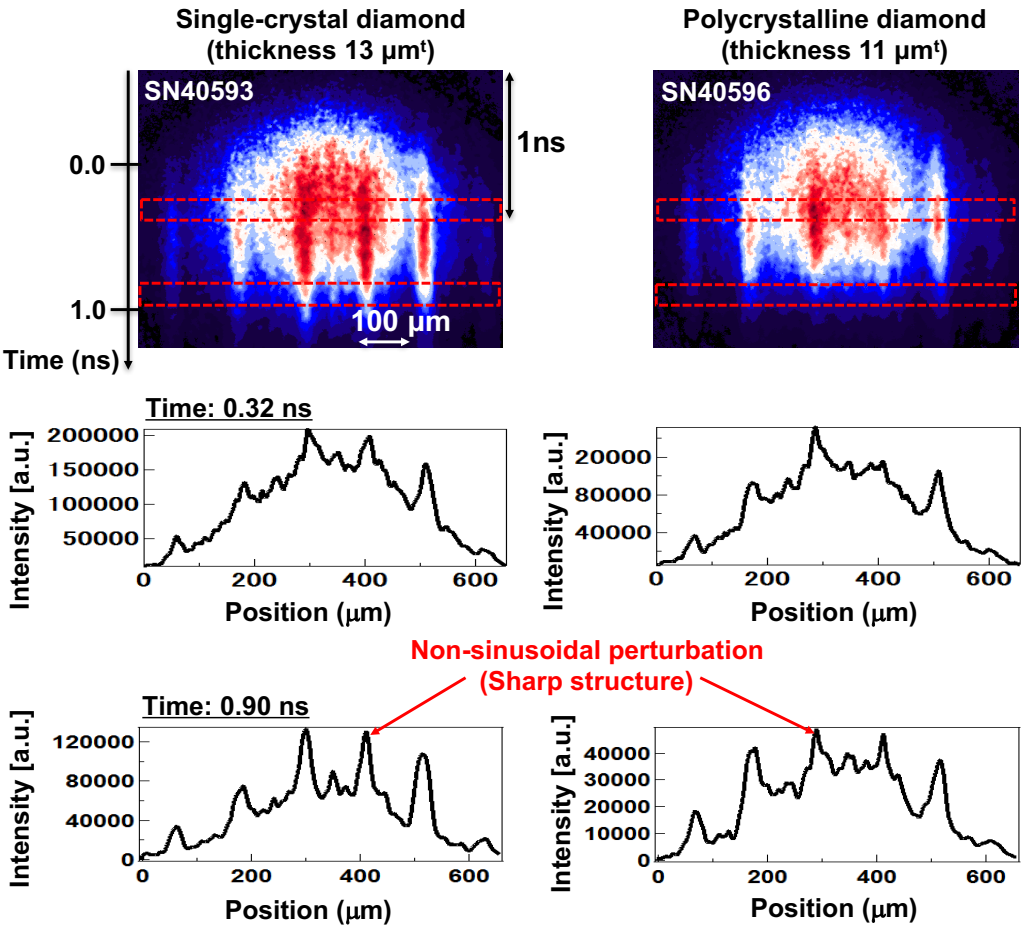

Figure 5.6: Raw streaked images for the face-on x-ray backlit single-crystal and polycrystalline diamond foils for the foot pulse intensity $\sim 4 \times 10^{12}$ W/cm^2. Irradiation nonuniformity of foot pulse is ~40 %. The time origin (t = 0) is onset main pulse (see Fig 4.1). Lineouts (black lines) are extracted by integrating the raw data over the temporal resolution. The lineouts shown are the backlit x-ray intensity distribution.

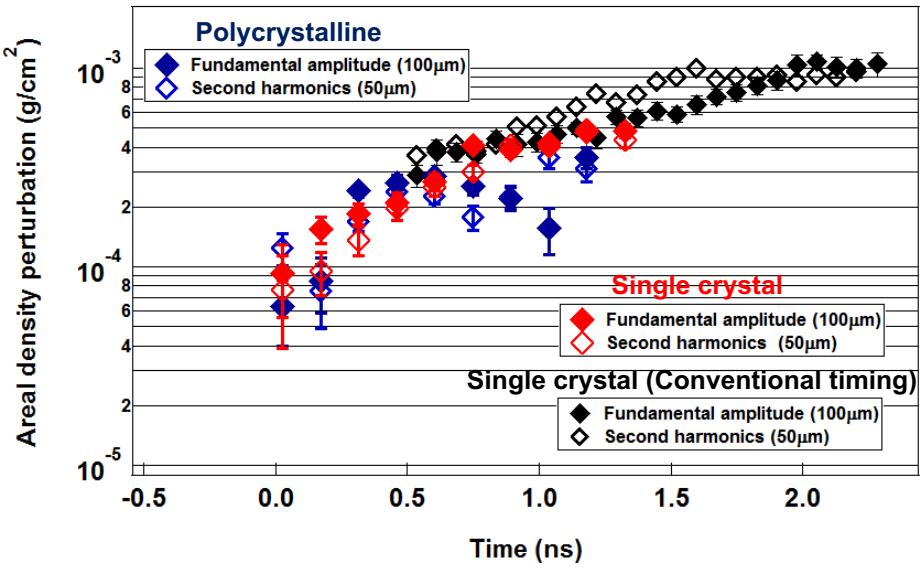

Figure 5.7: Areal-density perturbation growth for single-crystal and polycrystalline diamond targets from experiments (symbols). Experimental data (black symbols) for single-crystal diamond at conventional observation timing is shown in Fig. 5.3(b).

5.5 Conclusion

In conclusion, the influences of solid strength on the surface perturbation due to nonuniform irradiation and the perturbation structure have been investigated in experiment and simulation using diamond foils. When irradiation non-uniformity is large, 2D hydrodynamic simulation do not reproduce experimental results on the diamond foil. Pressure perturbations which partially exceeds the HEL of diamond develop into solid strength issues on laser imprinting. The thin high-Z surface coating is effective in suppressing local fracture due to yield strength on the large pressure perturbation. These findings are particularly closely related to the target physics at the early irradiation timing of direct-drive ICF. In particular, fracture of the brittle ablator due to nonuniform irradiation is sensitive to the performance of laser implosion. Although stiff materials would reduce laser imprinting, attention must be paid to the degree of irradiation nonuniformity on ICF. This data platform would be crucial for understanding not only on ICF target physics but also on laser-material interactions and laser processing.

Chapter 6

Characterrization and synthesis technology development of diamond target on direct-drive inertial confinement fusion

6.1 Introduction

In the direct-drive inertial confinement fusion (ICF), a fuel capsule is irradiated directly with the laser light. The capsule consists of a cryogenic layer of deuterium and tritium (DT) frozen onto the inner surface of a spherical shell of ablator material. Typical ignition and high-gain target capsules have diameters from 3 to 5 mm for MJ lasers [11]. Owing to such high power laser injection onto such a tiny space, the laser implosion occurs. To realize high efficient nuclear fusion reaction, uniform implosion is desirable to compress the fuels inside the shell. However, typically, laser imprinting occurs on the surface of ablator material due to irradiation non-uniformity [11, 17–19]. Spatial perturbation of the laser imprinting is amplified by the Rayleigh-Taylor instability (RTI) during the shell acceleration [11, 19, 21]. The grown perturbation could disrupt the shell and cause mixing of fuel. The level of the laser imprinting depends on the parameter of ignition

conditions (neutron yield and target areal-density) in ICF experiments [62,63]. As shown in Chapter 4, it was found that stiffness of the capsule material contribute to reduce the laser imprinting [64]. Therefore, diamond is considered to be the most probable candidate as a stiff ablator material for direct-drive ICF targets. On the other hand, since small perturbations on the target surface grow exponentially with time by the RTI, initial perturbations on the ICF target surface should be reduced as small as possible [11]. The surface perturbations are mainly caused by the surface roughness of the target as well as the laser imprinting. Specifically, the capsule is required to have uniform thickness of nanometer order as a target capsule to achieve efficient ignition [65]. Figure 6.1 shows acceptable deviations in ablator thickness uniformity of standard capsules for the respective mode numbers of Fourier series expansion of the initial perturbations, which was estimated theoretically. The quality of the capsules is expected to be influenced by fabrication processing. Therefore, the processing technique is also one of the key issues for realization of the laser fusion.

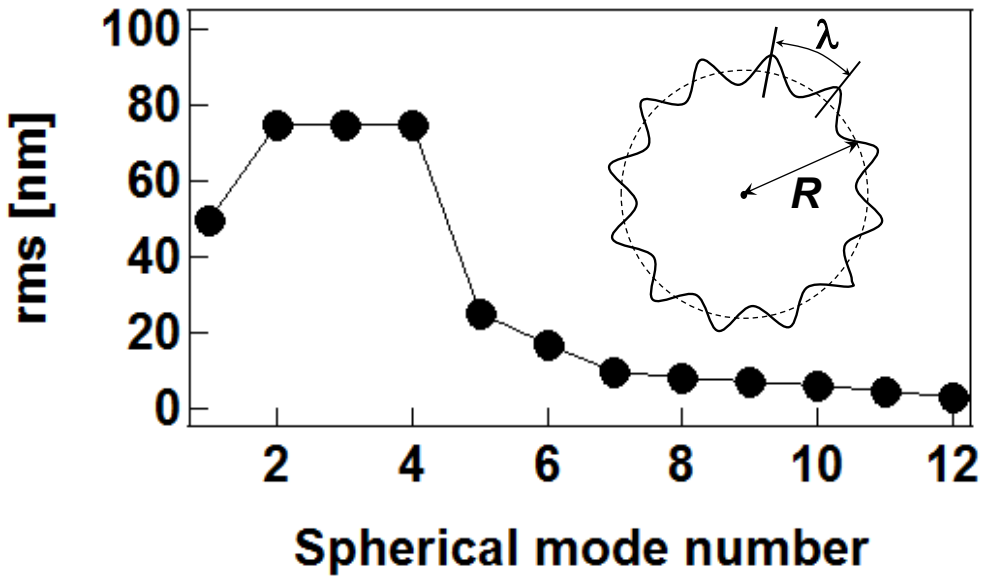

Figure 6.1: Low mode specifications for ablator thickness of capsule, in rms per mode. Mode number corresponds to $2\pi R/\lambda$, where R and λ are capsule radius and roughness wavelength, respectively. The data is shown in [65].

Artificial diamond was firstly reported by using high-pressure-high-temperature

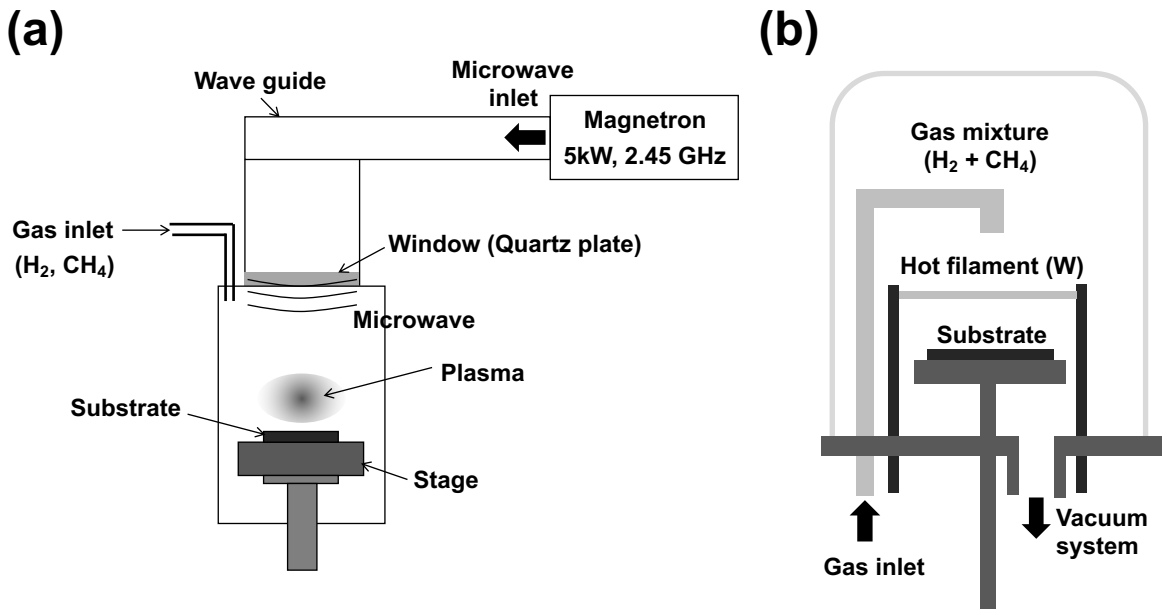

Figure 6.2: Diamond synthesize on chemical vapor deposition: (a) Microwave plasma CVD. (b) Hot filament CVD.

method [66]. This method is now widely adopted to product mechanical tools in industry. Also, chemical vapor deposition (CVD) is another possible way to obtain artificial diamond. Hydrogen radical plays a very important role when diamond is synthesized by gas phase synthesis method. Hydrogen radical selectively etches and suppresses sp2 bond (graphite component) and amorphous component by-product during diamond synthesis. Therefore, in the gas phase synthesis method, a method of efficiently generating hydrogen radicals is used. As a raw material, mixed gas of hydrogen and a small amount (0.1% to 3%) of carbon source is used, and it is often done at low pressure. This is due to the fact that as the pressure is lowered, the thermodynamic equilibrium moves toward the hydrogen radical side and the proportion of hydrogen radicals in the gas phase increases. In the production of diamond crystals by CVD, a large excess of hydrogen is introduced into hydrocarbons (such as methane), and the source gas is decomposed by microwave plasma or a filament (hot filament) heated to a high temperature ($\geq$ 2000 °C). Figure 6.2 shows the concept of microwave plasma CVD and hot filament CVD. The temperature was about 800 °C to 900 °C and the pressure of the atmosphere was several tens of torr when growing on the substrate. On

this principle it became possible for the first time to use a substrate such as silicon, aluminum, high melting point metal, ceramic It became possible to obtain diamond crystals with self-shaping on top of them. In addition to hydrocarbons such as methane, it is obvious that synthesis is also possible by using alcohols, ketones, carbon monoxide, etc. Microwave plasma (MWP) CVD would be the most widely adopted method to obtain the diamond films for electronics [67, 68]. Actually, the diamond capsules made from MWPCVD [69, 70] are commercially available. However, growth processing to prepare such artificial diamond capsules have not been studied well. Also, at the Lawrence Livermore National Laboratory, the growth conditions and processing of MWPCVD nanocrystalline-diamond films for laser-driven high-energy-density physics experiments have been carefully investigated [71]. In hot-filament (HF) CVD, the correlation between grain size and mechanical properties of nanocrystalline diamond films was studied [72], however, diamond capsules made by using the HFCVD have not been studied well.

This study focuses on hot-filament (HF) CVD as a candidate method to prepare the diamond capsules. If the growth surface on the capsule is very rough, a polishing process is required [69, 70]. Diamond is the hardest and chemically stable material. Therefore mechanical polishing by using diamond is typically applied [73]. This, however, causes mechanical damages underneath and the pits on the outermost surface. This may causes processing difficult, or even limits the quality of the capsules as a target. On the other hand, HFCVD is expected to realize fine structures of the capsule surface, which may not need post-polishing process. In addition, the expansion of the synthesis area is possible easily by increasing the number of filaments. By utilizing such advantages of HFCVD, there is also the possibility that ICF capsules would be fabricated easily. This chapter shows the growth process by using HFCVD and characterization of the diamond capsule by using HFCVD for the first time.

6.2 Fabrication of diamond capsules by using the hot filament chemical vapor deposition method

6.2.1 Experimental conditions

The goal of the fabrication of the diamond capsule is to obtain a diameter of ∼500 μm and diamond coatings with thickness less than ∼10 μm. The thin diamond capsules are fabricated to be compared with the previous ICF experiments [63] with polystyrene shell (diameter ∼500 μm, film thickness ∼8 μm) on GEKKO-XII Nd: glass laser facility at the Institute of Laser Engineering, Osaka University [39]. In this study, hot filament chemical vapor deposition (HFCVD) technique [74] was employed in high-rate growth condition [75]. Also, in principle, long-term operation to prepare thicker coated capsules is also possible [76]. Figure 6.3 shows the experimental setup for synthesis of diamond capsule due to HFCVD. Filament (W) is electrically heated approximately to 2000 degree. The feed gas mixture, H_2 and CH_4, are dissociated into the radicals, such as H, CH_3, and so on, by thermal reactions. These radicals deposit on Si spheres as diamond crystal. The roughness of the Si sphere was about ∼10 nm initially, which is much smaller than that of the deposited layer. In advance of the deposition, the spheres were seeded in an ultrasonically agitated diamond powder-IPA suspension, where the powder size was ∼400 nm. We tested the deposition by just putting the spheres, but failed to obtain fully coating; a certain area facing on the holder was not coated as shown in Fig. 6.4. Therefore, a feature to rotate the Si spheres during diamond CVD to achieve uniform and fully coating was equipped by using a vibrator as shown in Fig. 6.3. It takes approximately 5 h to deposit the required film thickness of ∼10 μm using a feed gas mixture of 3 percent methane in hydrogen at total pressure of 10 Torr. The deposition temperature is about 1000 degree on the molybdenum-holder.

After deposition of polycrystalline diamond films on the silicon spheres, a micrometre-sized hole is drilled by fs-laser ablation to remove the Si sphere (Fig. 6.5(a)). The Si sphere can then be removed using wet etching through this hole, where the

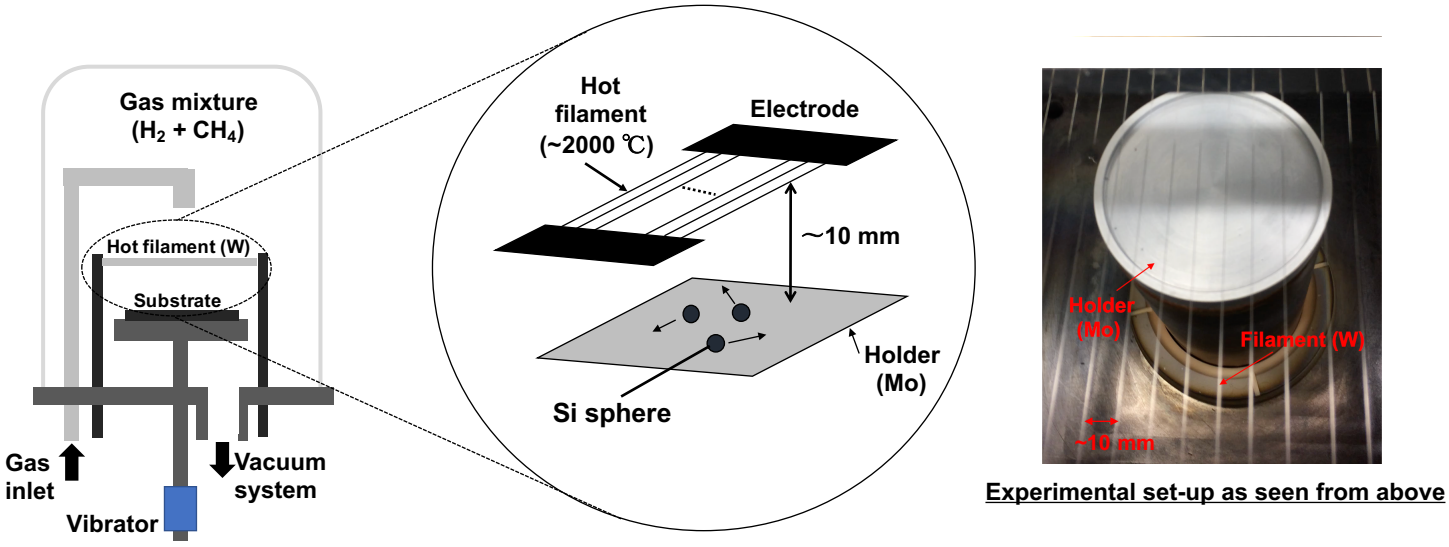

Figure 6.3: Deposition of polycrystalline diamond film on Si spheres by hot filament CVD.

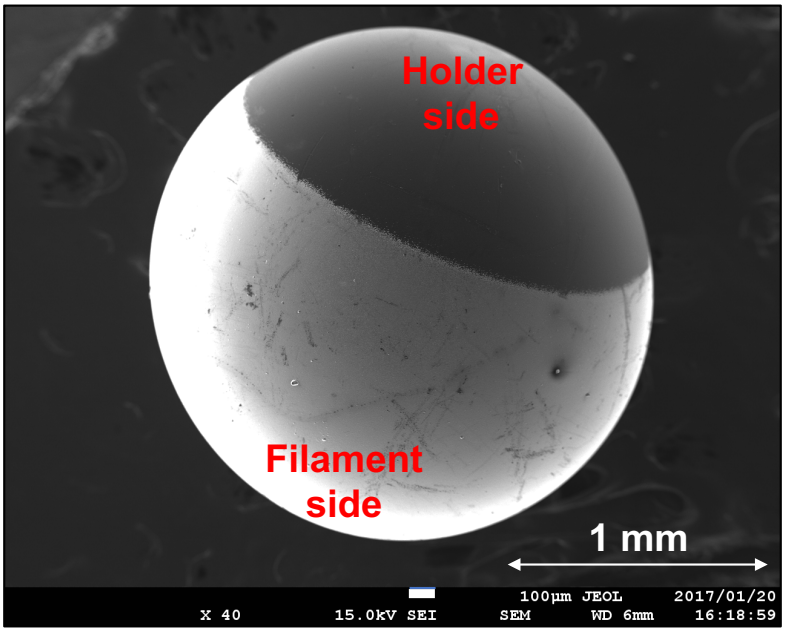

Figure 6.4: Observation result of diamond deposition by just putting Si sphere with the scanning electron microscope (SEM). Different of the surface-property be- tween holder side and filament side of the sphere appears.

spheres were dipped in the nitrohydrofluoric acid (HF/HNO3) solution under the room temperature (Fig. 6.5(b)). After removing the sphere, the hollow diamond capsule can then be filled with the DT fuel at cryogenic temperatures using a micrometre-sized fill tube glued to the hole.

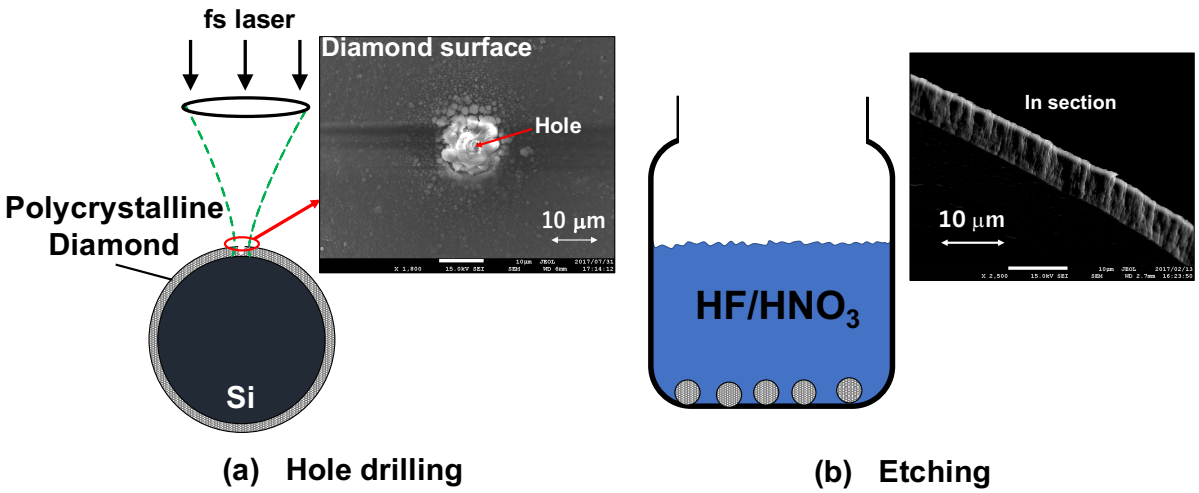

Figure 6.5: Fabrication of diamond shell for ICF experiments. (a) Fabrication of 3-5 μm diameter holes through the diamond film using fs laser (pulse width 300 fs) with a 3 MHz pulse repetition rate at an average power of 1 W. (b) Etching of the Si spheres using a HF/HNO_3 wet etch process. Then, Hydrofluoric acid (HF) and nitric acid (HNO_3) ratio are 3 : 1.

6.2.2 Experimental results

The polycrystalline diamond capsule of the diameter ~500 μm was obtained as shown in Fig. 6.6(a). Obvious (pin-) holes and voids could not be observed. However, the leak tests have been not checked, which is left as future works. The thickness of diamond after the wet etching of the Si spheres is less than 10 μm as in Fig. 6.5(b). The synthesis of diamond capsule with a few millimetre size is also possible (Fig. 6.7). The grain size of the diamond is much smaller than 1 μm (Fig. 6.6(b)). For the ICF application, solid or partially melted diamond ablator may produce microstructures that seed hydrodynamic instabilities, however, the overall design of laser-pulse shaping for stable high compression is very important and effective [54, 77]. Figure 6.8(a) show the measurement results of surface

roughness by atomic force microscope (AFM). Mean surface roughness for capsule is smaller than 100 nm (Fig. 6.8(b)). The surface roughness would be reduced if the grain size becomes smaller by the change of the synthetic parameter.

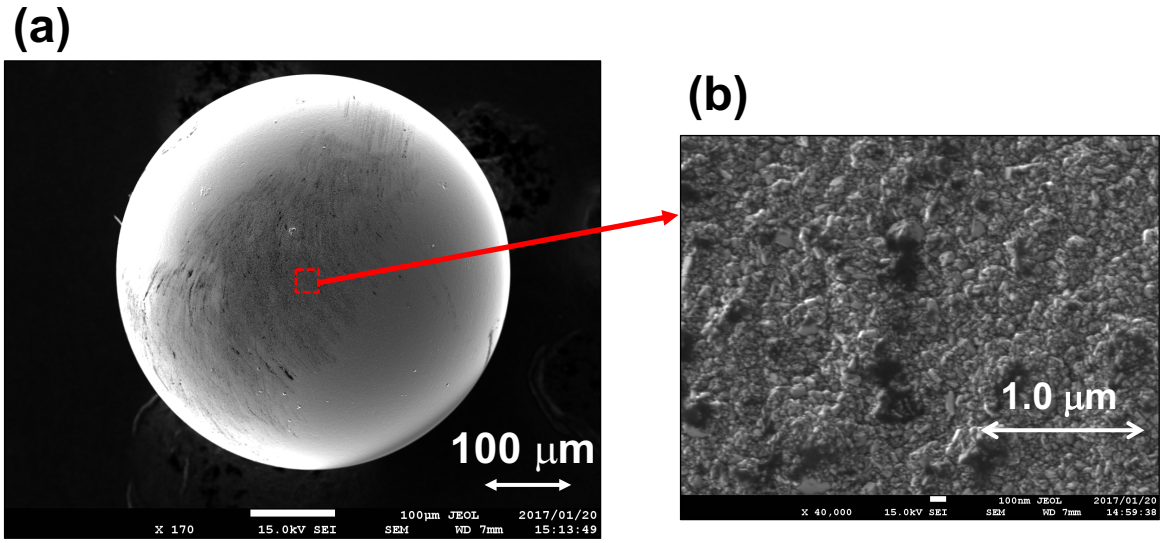

Figure 6.6: (a) Observation result of diamond capsule with the SEM. (b) Observation result of capsule surface with the SEM.

Estimated sphericity of the capsule was $99.7 \pm 0.2\%$. Figure 6.9(a) shows the diamond capsule after removal of the Si sphere in the optical microscope observation. The sphericity was estimated by measuring the radius at 10 points under the optical microscope. The errors are the reading errors due to the digital micrometer used. The sphericity S was defined as $S = 1 - (R_{\max} - R_{\mathrm{av}})/R_{\mathrm{av}}$, where $R_{\max}$ and R_{av} are maximum radius and average radius, respectively. Figure 6.9(b) shows the cross section of the capsule after removal of the Si sphere. The estimated sphericity ($99.8 \pm 0.2\%$) of the Si sphere is almost the same level as that of the diamond capsule, which implies that diamond is deposited on the Si surface with high uniformity (see Fig. 6.9(b)).

Also, Raman spectra of the fabricated capsule are shown in Fig. 6.10. Raman spectra were measured using the laser source with a wavelength of 532 nm. The capsule exhibited the Raman shift (1333 cm^{-1}) attributable to the presence of diamond (red line). Relations between ICF experiments and film property on the

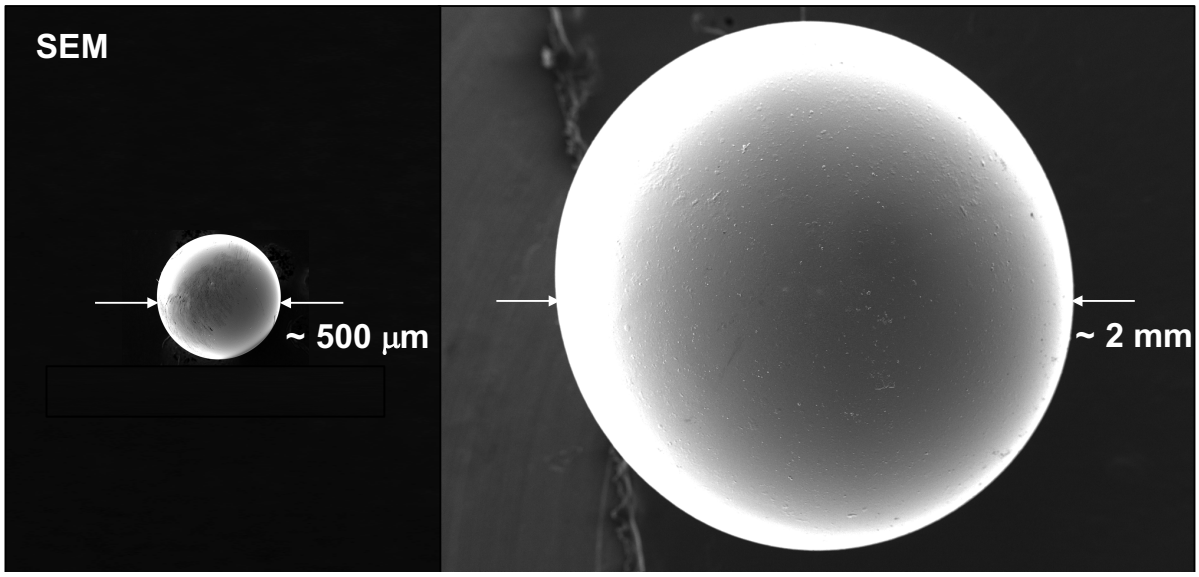

Figure 6.7: Synthesis size of diamond capsule.

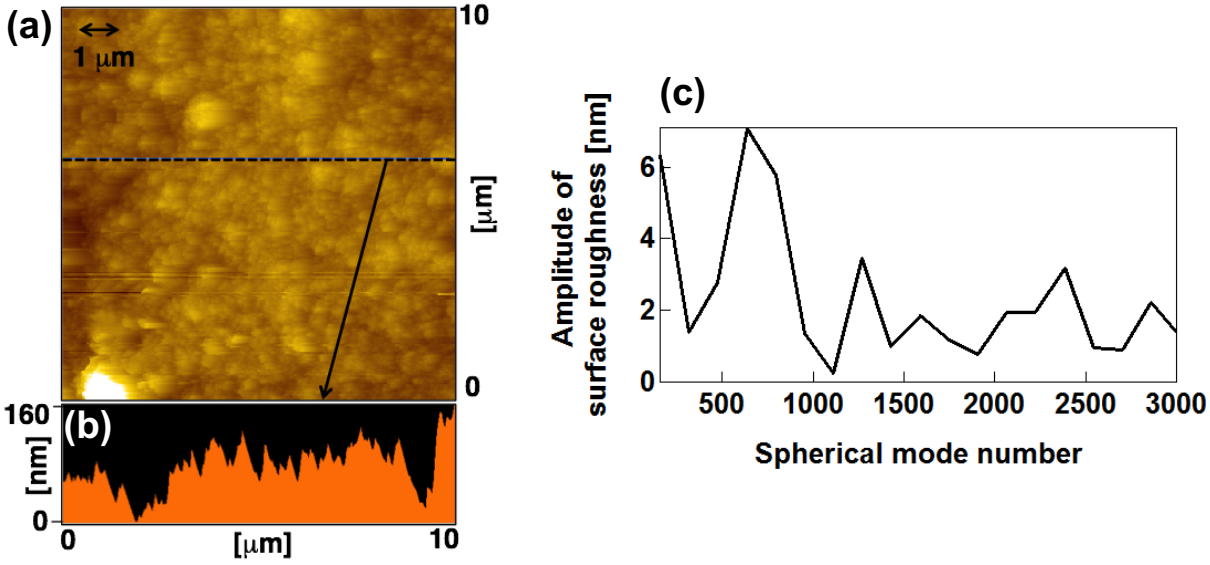

Figure 6.8: (a) Measurement of surface roughness by atomic force microscope. (b) Line profile of the capsule surface. (c) Spectrum of surface roughness for the spherical mode number.

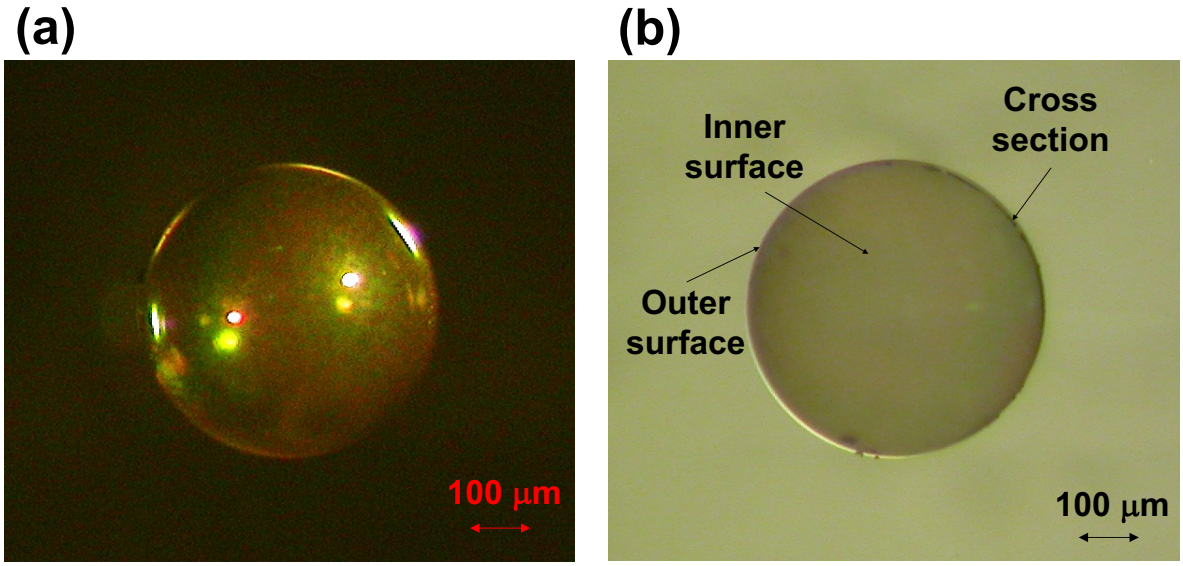

Figure 6.9: (a) Diamond capsule after removal of the Si sphere in the optical microscope observation. (b) Cross section of diamond capsule by the optical microscopy observation. The cross section of the capsule is obtained by laser processing.

component ratio of the deposited diamond and graphite are the future topics of discussion.

In the previous works on fabrication and characterization of diamond capsules for ICF experiments on NIF, the diamond capsules have been made using the MWCVD, which was polished by diamond grinding disk [69, 70]. However, the ∼100 nm polished rms surface roughness is dominated by the contribution from the pits formed during polishing. It is difficult to produce large quantities of diamond targets if polishing cannot be avoided. In this study, it was demonstrated that the capsule fabrication of the surface roughness of several nm level could be realized by the HFCVD method without post-processing. On the other hand, though this study have understood the amplitude of the surface roughness in relatively short wavelength (high-mode) as in Fig. 6.8(c), the long-wavelength (low mode) roughness is also important for the effect of feed-through to the inner capsule surface in ICF [1]. The evaluations of surface roughness including low mode should be done in future works.

In general, the differences of synthetic parameter between HFCVD and MWPCVD are gas pressure, CH_4/H_2 ratio, and so on mainly. In MWPCVD, the

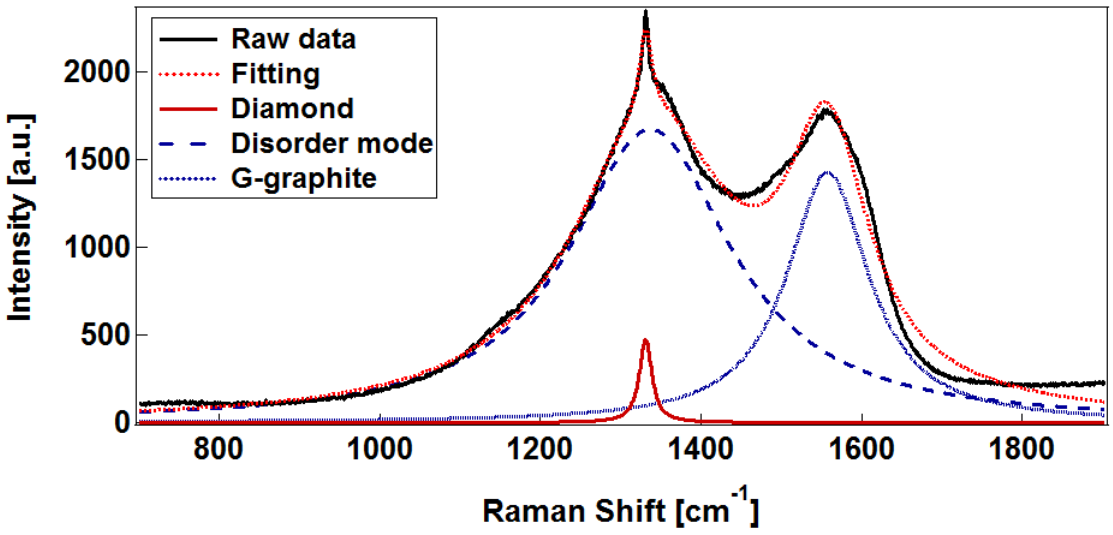

Figure 6.10: Raman spectra of the capsule fabricated by HFCVD. Each component was determined by fitting.

nanocrystalline diamond films was obtained by lowering the gas pressure or substrate temperature [91, 92]. It is considered that the synthetic condition is one of the factors that the surface gets smooth. In the previous works using HFCVD, nanocrystalline diamond films was synthesized on the synthetic condition similar to this study [93–95]. The grain size and morphology in diamond films depend on the gas pressure and the CH_4/H_2 ratio [94]. For example, nanocrystalline diamond films with surface roughness of about 16.5 nm and 8.2 nm have been obtained respectively under synthesis conditions of methane concentration 1%, gas pressure 37.5 torr and methane concentration 1%, gas pressure 0.94 torr [94]. Figure 6.11 shows dependence of CH_4/H_2 ratio and pressure on film properties for capsule surface. The particle size for 1% CH_4 concentration is larger than that of 3% concentration. Then, pyramidal morphology appears at 1% concentration, and the surface roughness increases as the grain size increases. On the other hand, the relatively flat morphology appears at 20 torr, and the crystal orientation is higher as in Fig. 6.11. The grain size at 20 torr is larger than that at 10 torr, but the surface roughness is smaller. There is a possibility that smoothness can be further improved by control of grain size, morphology, crystal orientation, and nuclear density. In addition, it has been reported that the grain size becomes smaller by

adding Ar gas [95]. To make grain size smaller and suitable morphology for realization of further smooth surfaces, the optimization of synthetic condition (gas concentration, synthetic temperature, gas pressure, and additions of Ar) is necessary.

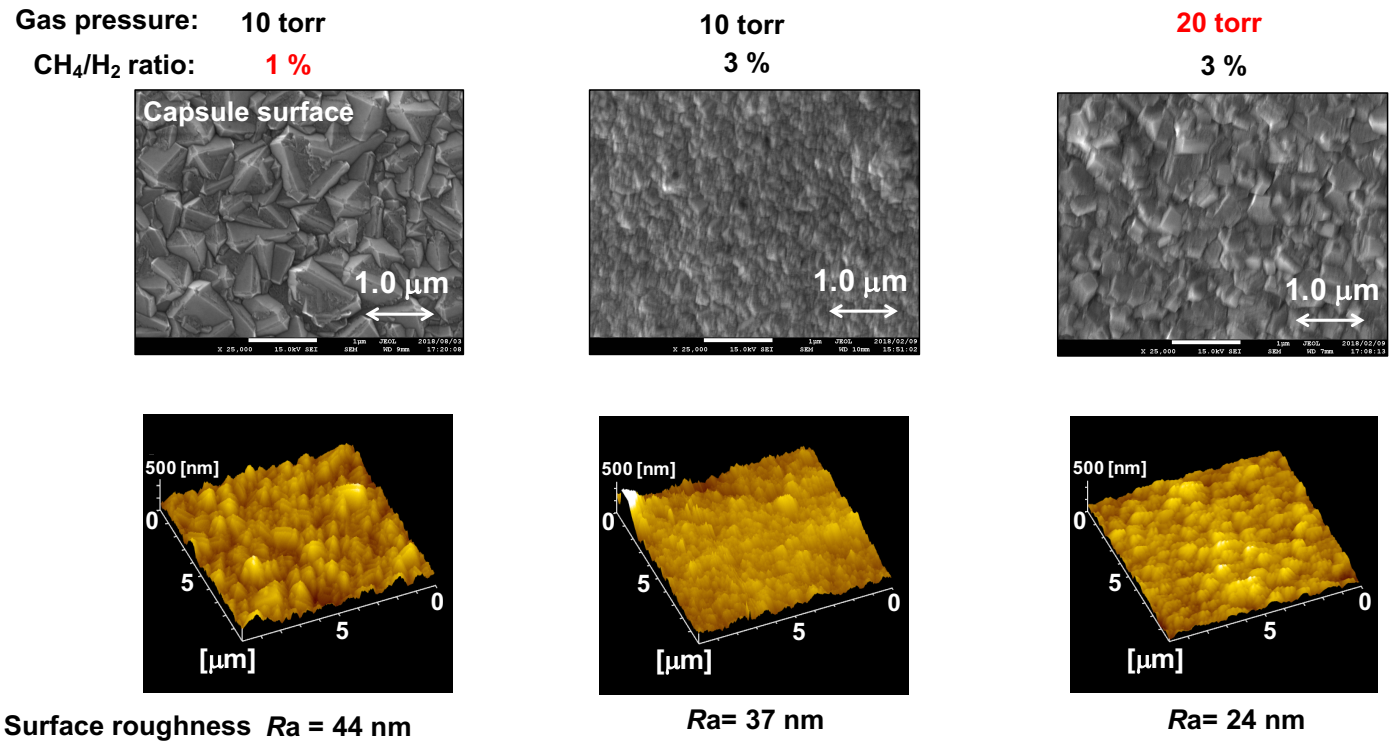

Figure 6.11: Dependence of synthesis parameters on capsule surface characteristics. Top figure shows the observation result of diamond surface with the SEM. The bottom figure shows the measurement of surface roughness (arithmetic average roughness) by AFM.

6.3 Conclusion

The synthesis and characterization of the diamond capsule as the ICF target was performed by using CVD technique. The capsule (diameter $\sim$500 μm) with the sphericity 99.7%, film thickness $\leq$ 10μm, and the surface smoothness of several nm to several tens nm level was obtained only by the HFCVD method where the vibration system was added so that Si spheres roll on the holder. Obvious (pin-) holes and voids could not be observed at least by using SEM (see Fig. 6.6). However, the leak tests have not been checked, which are left as future works. Also, it seems to be feasible to produce large quantities of diamond targets and surface roughness is reduced by controlling grain size using the HFCVD.

Chapter 7

Conclusions

In direct-drive ICF for which a spherical target capsule is irradiated directly with intense laser beams, laser imprinting due to irradiation non-uniformity on the capsule surface consequently degrades symmetry of the target implosion and reduces the fusion yield. Suppressing imprint perturbation even under nonuniform laser irradiation is the important subject for direct-drive ICF. In conclusion, this study clarify herein how density and compressibility affect laser imprinting by using diamond as a candidate stiff-ablator material for ICF targets. The effect of density and compressibility is verified both by using 2D hydrodynamic simulations and by experiments. Laser imprinting on high-foot PS is compared with the same on high-foot diamond, and the same is done for high- versus low-foot diamond. For high-foot conditions (both diamond and PS), the difference in imprinting amplitude is mainly due to the difference in density and compressibility. Conversely, the difference in imprinting amplitude for low-foot diamond is influenced by standoff distance and by the difference in material compressibility between the elastic body and the plastic body. The 2D simulation well reproduces the measurements of areal-density perturbation, which reveals the effect of density and compressibility on laser imprinting. The advantage of low-compressibility materials in ICF target design is that such a scheme may be combined with another suppression scheme by enhancing the standoff distance, as was proposed in previous works. For example, the mitigation method involving high-Z material coatings is easily coupled with

the present scheme. By combining these schemes, both short- and long-wavelength laser imprinting would be mitigated. The physics of material stiffness affecting laser irradiation is also very important, not only for ICF target design but also for general questions on laser-matter interactions for laser processing, laser peening, and other applications.

The effect of ablator strength on imprint, with low initial laser intensity in particular, is an important topic as direct-drive inertial confinement fusion (ICF). As mentioned above, diamond can be expected as a possible stiff ablator material for direct-drive ICF targets. On the other hand, little is known the phenomenon regarding solid-strength issue including fracture in laser imprinting. In this study, perturbation structure and influence of the solid strength on diamond surface due to laser irradiation nonuniformity has been also investigated. Experiments suggest that local fracture is generated by large irradiation non-uniformity, which is not reproduced by two-dimensional radiation hydrodynamic simulation PINOCO-2D. The perturbation generated by irradiation nonuniformity of single mode was observed by amplifying its perturbation with Rayleigh-Taylor instability growth. Areal-density perturbation for single-crystal diamond and diamond with thin high atomic number (high-Z) coating foils was measured. Experimental results and 2D simulations show that spatial pressure perturbations (or irradiation nonuniformity) that partially exceed the yield strength develop into solid strength issues on laser imprinting. Also, the combination of a stiff material and thin high-Z coating is effective for suppression of the solid-strength issue due to large irradiation non-uniformity.

Finally, aiming at improving performance of ICF targets, synthesis technology of diamond capsules as the ablator material of direct-drive ICF targets have been developed. In this study, polycrystalline diamond capsules were fabricated by using the HFCVD method. The capsule (diameter ~ 500 or $\sim 2000\,\mu$m) with the sphericity 99.7%, film thickness $\leq 10\mu$m, and the surface smoothness $\leq 0.1\,\mu$m was obtained without mechanical polishing. Also, it seems to be feasible to produce large quantities of diamond targets and surface roughness is reduced by controlling grain size, morphology, crystal orientation, and nuclear density using the HFCVD.

Contributions

This work was performed under a joint research project of the Institute of Laser Engineering, Osaka University. This work was also performed with the support and under the auspices of the NIFS Collaboration Research program (NIFS10KUGK044). The authors would like to acknowledge the dedicated technical support of the staff at the GEKKOXII facility for laser operation, target fabrication, and plasma diagnostics. This work was partly supported by the Japan Society for Promotion of Science, KAKENHI Grant No. 23340175. This study was carried out by collaborative investigation with National Institute of Advanced Industrial Science and Technology (AIST) and Institute of Laser Engineering, Osaka University.

Publications

Refereed papers

- H. Kato, K. Shigemori, H. Nagatomo, M. Nakai, T. Sakaiya, T. Ueda, H. Terasaki, Y. Hironaka, K. Shimizu, and H. Azechi, Effect of equation of state on laser imprinting by comparing diamond and polystyrene foils, Physics of Plasmas 25, 032706 (2018).
- H. Kato, H. Yamada, S. Ohmagari, A. Chayahara, Y. Mokuno, Y. Fukuyama, N. Fujiwara, K. Miyanishi, Y. Hironaka, and K. Shigemori, Synthesis and characterization of diamond capsules for direct-drive inertial confinement fusion, Diamond and Related Materials 86 (2018) 15-19.
- K. Shigemori, H. Kato, M. Nakai, R. Hosogi, T. Sakaiya, H. Terasaki, S. Fujioka, A. Sunahara, and H. Azechi, J. Phys. Conf. Ser. 688, 012107 (2016).
- S. Hattori, K. Shigemori, Y. Hironaka, T. Yamamoto, H. Kato, S. Fujioka, H. Shiraga, and H. Azechi, Plasma Fusion Res. 10, 1 (2015).

References

[1] S. Atzeni and J. Meyer-ter-Vehn, The Physics of Inertial Fusion (Clarendon-Press,Oxford,2004).

[2] Asher Peres, Journal of Applied Physics 50, 5569 (1979).

[3] O.Motojima,TheITERprojectconstructionstatus,Nucl.Fusion55(2015)104023.

[4] J. Nuckolls, L. Wood, A. Thiessen, and G. Zimmerman, " Laser compression of matter to super-high densities: Thermonuclear (CTR) applications, " Nature 239, 139 (1972).

[5] J. D. Lindl, " Development of the indirect-drive approach to inertial confinement fusion and the target physics basis for ignition and gain, " Phys. Plasmas 2, 3933 (1995).

[6] J. D. Lindl, Inertial Confinement Fusion: The Quest for Ignition and Energy Gain Using Indirect Drive (Springer-Verlag, New York, 1998).

[7] D. Richtmyer, "Taylor instability in shock acceleration of compressible fluids, " Commun. Pure Appl. Math. XIII, 297 (1960).

[8] E. E. Meshkov, " Instability of the interface of two gases accelerated by a shock wave, " Fluid Dyn. 4(5), 101 (1969).

[9] D. Shvarts, U. Alon, D. Ofer, R. L. McCrory, and C. P. Verdon., Phys. Plasmas 2, 2465 (1995).

[10] H. Takabe, K. Mima, L. Montierth, and R. L. Morse, Phys. Fluids 28, 3676 (1985).

[11] R. S. Craxton, K. S. Anderson, T. R. Boehly, V. N. Goncharov, D. R. Harding, J. P. Knauer, R. L. McCrory, P. W. McKenty, D. D. Meyerhofer, J. F. Myatt, A. J. Schmitt, J. D. Sethian, R. W. Short, S. Skupsky, W. Theobald, W. L. Kruer, K. Tanaka, R. Betti, T. J. B. Collins, J. A. Delettrez, S. X. Hu, J. A. Marozas, A. V. Maximov, D. T. Michel, P. B. Radha, S. P. Regan, T. C. Sangster, W. Seka, A. A. Solodov, J. M. Soures, C. Stoeckl, and J. D. Zuegel, Phys. Plasmas 22, 110501 (2015).

[12] K. S. Budil, B. A. Remington, T. A. Peyser, K. O. Mikaelian, P. L. Miller, N. C. Woolsey, W. M. Wood-Vasey, and A. M. Rubenchik., Phys. Rev. Lett. 76, 4536 (1996).

[13] T. Berger, P. Testa, A. Hillier, P. Boerner, B. C. Low, K. Shibata, C. Schrijver, T. Tarbell, and A. Title, Nature (London) 472, 197 (2011).

[14] G. Zandt, H. Gilbert, T. J. Owens, M. Ducea, J. Saleeby, and C. H. Jones, Nature (London) 431, 41 (2004).

[15] S. E. Bodner, D. G. Colombant, J. H. Gardner, R. H. Lehmberg, S. P. Obenschain, L. Phillips, A. J. Schmitt, J. D. Sethian, R. L. McCrory, W. Seka, C. P. Verdon, J. P. Knauer, B. B. Afeyan, and H. T. Powell, Phys. Plasmas 5, 1901 (1998).

[16] V. A. Smalyuk, Phys. Scr. 86, 058204 (2012). and references therein.

[17] V. N. Goncharov, S. Skupsky, T. R. Boehly, J. P. Knauer, P. McKenty, V. A. Smalyuk, R. P. J. Town, O. V. Gotchev, R. Betti, and D. D. Meyerhofer, Phys. Plasmas 7, 2062 (2000).

[18] R. J. Taylor, A. L. Velikovich, J. P. Dahlburg, and J. H. Gardner, Phys. Rev. Lett. 79, 1861 (1997).

[19] M. Nakai, H. Azechi, N. Miyanaga, K. Shigemori, T. Kawasaki, T. Nagaya, M. Nishikino, Y. Kanai, D. Ohnuki, H. Nishimura, H. Shiraga, O. Maegawa, R. Ishizaki, K. Nishihara, H. Takabe, and T. Yamanaka, Phys. Plasmas 9, 1734 (2002).

[20] T. Endo, K. Shigemori, H. Azechi, A. Nishiguchi, K. Mima, M. Sato, M. Nakai, S. Nakaji, N. Miyanaga, S. Matsuoka, A. Ando, K. A. Tanaka, and S. Nakai, Phys. Rev. Lett. 74, 3608 (1995).

[21] H. Azechi, M. Nakai, K. Shigemori, N. Miyanaga, H. Shiraga, H. Nishimura, M. Honda, R. Ishizaki, J. G. Wouchuk, H. Takabe, K. Nishihara, K. Mima, A. Nishiguchi, and T. Endo, Phys. Plasmas 4, 4079 (1997).

[22] H. Azechi, K. Shigemori, M. Nakai, N. Miyanaga, and H. Takabe, Astrophys. J. Suppl. Ser. 127, 219 (2000).

[23] K. A. Brueckner and S. Jorna, Rev. Mod. Phys. 46, 325 (1974); S. E. Bodner, J. Fusion Energy 1, 221 (1981).

[24] M. Desselberger, M. W. Jones, J. Edwards, M. Dunne, and O. Willi, Phys. Rev. Lett. 74, 2961 (1995).

[25] R. G. Watt, J. Duke, C. J. Fontes, P. L. Gobby, R. V. Hollis, R. A. Kopp, R. J. Mason, D. C. Wilson, C. P. Verdon, T. R. Boehly, J. P. Knauer, D. D. Meyerhofer, V. Smalyuk, R. P. J. Town, A. Iwase, and O. Willi, Phys. Rev. Lett. 81, 4644 (1998).

[26] R. Feynman, N. Metropolis, and E. Teller, Phys. Rev. 75, 1561(1949)

[27] S.P. Lyon and J.D.Johnson. LA − CP − 98 − 100. Technical report, Los Alamos National Laboratory, 1998.

[28] N. Metzler, A. L. Velikovich, A. J. Schmitt, and J. H. Gardner, Phys. Plasmas 9, 5050 (2002).

[29] S. Depierreux, D. T. Michel, V. Tassin, P. Loiseau, C. Stenz, and C. Labaune, Phys. Rev. Lett. 103, 115001 (2009).

[30] S. P. Obenschain, D. G. Colombant, M. Karasik, C. J. Pawley, V. Serlin, A. J. Schmitt, J. L. Weaver, J. H. Gardner, L. Phillips, Y. Aglitskiy, Y. Chan, J. P. Dahlburg, and M. Klapisch, Phys. Plasmas 9, 2234 (2002).

[31] M. Karasik, J. L. Weaver, Y. Aglitskiy, J. Oh, and S. P. Obenschain, Phys. Rev. Lett. 114, 085001 (2015).

[32] J. P. Knauer, K. Anderson, R. Betti, T. J. B. Collins, V. N. Goncharov, P. W. McKenty, D. D. Meyerhofer, P. B. Radha, S. P. Regan, T. C. Sangster, V. A. Smalyuk, J. A. Frenje, C. K. Li, R. D. Petrasso, and F. H. S eguin, Phys. Plasmas 12, 056306 (2005).

[33] M. Nishikino, H. Shiraga, N. Miyanaga, N. Ohnishi, K. Shigemori, S. Fujioka, M. Nakai, H. Nishimura, H. Azechi, K. Mima, H. Takabe, S. Nakai, and T. Yamanaka, Phys. Plasmas 9, 1381 (2002).

[34] W. M. Manheimer, D. G. Colombant, and J. H. Gardner, Phys. Fluids. 25, 1644 (1982).

[35] D. G. Hicks, T. R. Boehly, P. M. Celliers, D. K. Bradley, J. H. Eggert, R. S. McWilliams, R. Jeanloz, and G. W. Collins, Phys. Rev. B 78, 174102 (2008).

[36] J. H. Eggert, D. G. Hicks, P. M. Celliers, D. K. Bradley, R. S. McWilliams, R. Jeanloz, J. E. Miller, T. R. Boehly, and G. W. Collins, Nat. Phys. 6, 40 (2010).

[37] R. S. McWilliams, J. H. Eggert, D. G. Hicks, D. K. Bradley, P. M. Celliers, D. K. Spaulding, T. R. Boehly, G. W. Collins, and R. Jeanloz, Phys. Rev. B 81, 014111 (2010).

[38] M. D. Knudson, M. P. Desjarlais, and D. H. Dolan, Science 322, 1822 (2008).

[39] C. Yamanaka, Y. Kato, Y. Izawa, K. Yoshida, T. Yamanaka, T. Sasaki, M. Nakatsuka, T. Mochizuki, J. Kuroda, and S. Nakai, IEEE J. Quantum Electron. 17, 1639 (1981).

[40] Y. Kato, K. Mima, N. Miyanaga, S. Arinaga, Y. Kitagawa, M. Nakatsuka, and C. Yamanaka, Phys. Rev. Lett. 53, 1057 (1984).

[41] T. Sakaiya, H. Azechi, M. Matsuoka, N. Izumi, M. Nakai, K. Shigemori, H. Shiraga, A. Sunahara, H. Takabe, and T. Yamanaka, Phys. Rev. Lett. 88, 145003 (2002).

[42] H. Azechi, T. Sakaiya, S. Fujioka, Y. Tamari, K. Otani, K. Shigemori, M. Nakai, H. Shiraga, N. Miyanaga, and K. Mima, Phys. Rev. Lett. 98, 045002 (2007).

[43] K. Shigemori, H. Azechi, M. Nakai, M. Honda, K. Meguro, N. Miyanaga, H. Takabe, and K. Mima, Phys. Rev. Lett. 78, 250 (1997).

[44] N. Ozaki, T. Sano, M. Ikoma, K. Shigemori, T. Kimura, K. Miyanishi, T. Vinci, F. H. Ree, H. Azechi, T. Endo, Y. Hironaka, Y. Hori, A. Iwamoto, T. Kadono, H. Nagatomo, M. Nakai, T. Norimatsu, T. Okuchi, K. Otani, T. Sakaiya, K. Shimizu, A. Shiroshita, A. Sunahara, H. Takahashi, and R. Kodama, Phys. Plasmas 16, 062702 (2009); M. A. Barrios, D. G. Hicks, T. R. Boehly, D. E. Fratanduono, J. H. Eggert, P. M. Celliers, G. W. Collins, and D. D. Meyerhofer, ibid. 17, 056307 (2010).

[45] H. Takabe, M. Yamanaka, K. Mima, C. Yamanaka, H. Azechi, N. Miyanaga, M. Nakatsuka, T. Jitsuno, T. Norimatsu, M. Takagi, H. Nishimura, M. Nakai, T. Yabe, T. Sasaki, K. Yoshida, K. Nishihara, Y. Kato, Y. Izawa, T. Yamanaka, and S. Nakai, Phys. Fluids 31, 2884 (1988).

[46] H. Nagatomo, T. Johzaki, T. Nakamura, H. Sakagami, A. Sunahara, and K. Mima, Phys. Plasmas 14, 056303 (2007).

[47] L. Spitzer and R. Harm, Phys. Rev. 89, 977 (1953).

[48] R. M. More, K. H. Warren, D. A. Young, and G. B. Zimmerman, Phys. Fluids. 31, 3059 (1988).

[49] Ya. B. Zel ' dovich and Yu. B. Raizer. Physics of Shock Waves and High-Temperature Hydrodynamic Phenomena. Dover Publications, 2002.

[50] M. A. Barrios, D. G. Hicks, T. R. Boehly, D. E. Fratanduono, J. H. Eggert, P. M. Celliers, G. W. Collins, and D. D. Meyerhofer

[51] L. X. Benedict, K. P. Driver, S. Hamel, B. Militzer, T. Qi, A. A. Correa, A. Saul, and E. Schwegler, Phys. Rev. B 89, 224109 (2014).

[52] X. Wang, S. Scandolo, and R. Car, Phys. Rev. Lett. 95, 185701 (2005).

[53] S. G. Glendinning, S. N. Dixit, B. A. Hammel, D. H. Kalantar, M. H. Key, J. D. Kilkenny, J. P. Knauer, D. M. Pennington, B. A. Remington, R. J. Wallace, and S. V. Weber, Phys. Rev. Lett. 78, 3318 (1997).

[54] A. J. MacKinnon, N. B. Meezan, J. S. Ross, S. Le Pape, L. Berzak Hopkins, L. Divol, D. Ho, J. Milovich, A. Pak, J. Ralph, T. Doppner, P. K. Patel, C. Thomas, R. Tommasini, S. Haan, A. G. MacPhee, J. McNaney, J. Caggiano, R. Hatarik, R. Bionta, T. Ma, B. Spears, J. R. Rygg, L. R. Benedetti, R. P. J. Town, D. K. Bradley, E. L. Dewald, D. Fittinghoff, O. S. Jones, H. R. Robey, J. D. Moody, S. Khan, D. A. Callahan, A. Hamza, J. Biener, P. M. Celliers, D. G. Braun, D. J. Erskine, S. T. Prisbrey, R. J. Wallace, B. Kozioziemski, R. Dylla-Spears, J. Sater, G. Collins, E. Storm, W. Hsing, O. Landen, J. L. Atherton, J. D. Lindl, M. J. Edwards, J. A. Frenje, M. Gatu-Johnson, C. K. Li, R. Petrasso, H. Rinderknecht, M. Rosenberg, F. H. Seguin, A. Zylstra, J. P. Knauer, G. Grim, N. Guler, F. Merrill, R. Olson, G. A. Kyrala, J. D. Kilkenny, A. Nikroo, K. Moreno, D. E. Hoover, C. Wild, and E. Werner, Phys. Plasmas 21, 056318 (2014).

[55] P. M. Celliers, D. J. Erskine, C. M. Sorce, D. G. Braun, O. L. Landen, and G. W. Collins, Rev. Sci. Instrum. 81, 035101 (2010).

[56] L. F. Berzak Hopkins, N. B. Meezan, S. Le Pape, L. Divol, A. J. Mackinnon, D. D. Ho, M. Hohenberger, O. S. Jones, G. Kyrala, J. L. Milovich, A. Pak, J. E. Ralph, J. S. Ross, L. R. Benedetti, J. Biener, R. Bionta, E. Bond, D. Bradley, J. Caggiano, D. Callahan, C. Cerjan, J. Church, D. Clark, T. Doppner, R. Dylla-Spears, M. Eckart, D. Edgell, J. Field, D. N. Fittinghoff,

M. Gatu Johnson, G. Grim, N. Guler, S. Haan, A. Hamza, E. P. Hartouni, R. Hatarik, H. W. Herrmann, D. Hinkel, D. Hoover, H. Huang, N. Izumi, S. Khan, B. Kozioziemski, J. Kroll, T. Ma, A. MacPhee, J. McNaney, F. Merrill, J. Moody, A. Nikroo, P. Patel, H. F. Robey, J. R. Rygg, J. Sater, D. Sayre, M. Schneider, S. Sepke, M. Stadermann, W. Stoeffl, C. Thomas, R. P. J. Town, P. L. Volegov, C. Wild, C. Wilde, E. Woerner, C. Yeamans, B. Yoxall, J. Kilkenny, O. L. Landen, W. Hsing, and M. J. Edwards, Phys. Rev. Lett. 114, 175001 (2015).

[57] Correa A.A. *etal* 2006 Proc. Natl Acad. Sci. 103 1204.

[58] Johnston R.L. and Hoffmann R. 1989 J. Am. Chem. Soc. 111 810.

[59] T. R. Boehly, Y. Fisher, D. D. Meyerhofer, W. Seka, J. M. Soures, and D. K. Bradley, Phys. Plasmas 8, 231 (2001).

[60] D. K. Bradley, J. H. Eggert, R. F. Smith, S. T. Prisbrey, D. G. Hicks, D. G. Braun, J. Biener, A. V. Hamza, R. E. Rudd, and G. W. Collins, Phys. Rev. Lett. 102, 075503 (2009).

[61] J. H. Eggert, D. G. Hicks, P. M. Celliers, D. K. Bradley, J. E. Cox, W. G. Unites, G. W. Collins, R. S. McWilliams, R. Jeanloz, S. Brygoo, and P. Loubeyre, in Proceedings of Joint 20th AIRAPT-43th EHPRG International Conference on High Pres- sure Science and Technology, Karlsruhe, 2005.

[62] R. Nora, R. Betti, K.S. Anderson, A. Shvydky, A. Bose, K.M. Woo, A.R. Christopherson, J.A. Marozas, T.J.B. Collins, P.B. Radha, S.X. Hu, R. Epstein, F.J. Marshall, R.L. McCrory, T.C. Sangster, D.D. Meyerhofer, Theory of hydro- equivalent ignition for inertial fusion and its applications to OMEGA and the National Ignition Facility, Phys. Plasmas 21 (2016) 056316.

[63] K. Mima, Y. Kato, H. Azechi, K. Shigemori, H. Takabe, N. Miyanaga, T. Kanabe, T. Norimatsu, H. Nishimura, H. Shiraga, M. Nakai, R. Kodama, K.A. Tanaka, M. Takagi, M. Natatsuka, K. Nishihara, T. Yamanaka, S. Nakai, Recent progress of implosion experiments with uniformity-improved

GEKKO XII laser facility at the Institute of Laser Engineering, Osaka University, Phys. Plasmas 3 (1996) 2077.

[64] H. Kato, K. Shigemori, H. Nagatomo, M. Nakai, T. Sakaiya, T. Ueda, H. Terasaki, Y. Hironaka, K. Shimizu, H. Azechi, Effect of equation of state on laser imprinting by comparing diamond and polystyrene foils, Phys. Plasmas 25 (2018) 032706.

[65] S.W. Haan, T. Dittrich, G. Strobel, S. Hatchett, D. Hinkel, M. Marinak, D. Munro, O. Jones, S. Pollaine, L. Suter, Update on ignition target fabrication specifications, Fusion Sci. Technol. 41 (2002) 164.

[66] F.P. Bundy, H.T. Hall, H.M. Strong, R.H. Wentorf, Man-made Diamonds, Nature (4471) (1955) 51.

[67] M. Kamo, Y. Sato, S. Matsumoto, N. Setaka, J. Cryst, Diamond synthesis from gas phase in microwave plasma, Growth 62 (1983) 642.

[68] H. Yamada, A. Chayahara, S. Ohmagari, Y. Mokuno, Factors to control uniformity of single crystal diamond growth by using microwave plasma CVD, Diam. Relat. Mater. 63 (2016) 17.

[69] J. Biener, D.D. Ho, C. Wild, E. Woerner, M.M. Biener, B.S. El-dasher, D.G. Hicks, J.H. Eggert, P.M. Celliers, G.W. Collins, Diamond spheres for inertial confinement fusion, Nucl. Fusion 49 (2009) 112001.

[70] H. Huang, L.C. Carlson, W. Requieron, N. Rice, D. Hoover, M. Farrell, D. Goodin, A. Nikroo, J. Biener, M. Stadernann, S.W. Haan, D. Ho, C. Wild, Quantitative defect analysis of ablator capsule surfaces using a Leica confocal microscope and a high- density atomic force microscope, Fusion Sci. Technol. 70 (2016) 141.

[71] Christoph Dawedeit, Sergei O. Kucheyev, Swanee J. Shin, Trevor M. Willey, Michael Bagge-Hansen, Tom Braun, Y. Morris Wang, Bassem S. El-Dasher, Nick E. Teslich, Monika M. Biener, Jianchao Ye, Lutz Kirste, Claus-C.

Roehlig, Marco Wolfer, Eckhard Woerner, Anthony W. van Buuren, Alex V. Hamza, Christoph Wild, Juergen Biener, Grain size dependent physical and chemical properties of thick CVD diamond films for high energy density physics experiments, Diam. Relat. Mater. 40 (2013) 75-81.

[72] M. Wiora, K. Bruhne, A. Floter, P. Gluche, T.M. Willey, S.O. Kucheyev, A.W. Van Buuren, A.V. Hamza, J. Biener, H.-J. Fecht, Grain size dependent mechanical properties of nanocrystalline diamond films grown by hot-filament CVD, Diam. Relat. Mater. 18 (2009) 927-930.

[73] T. Schuelke, T.A. Grotjohn, Diamond polishing, Diam. Relat. Mater. 32 (2013) 17.

[74] R. Haubner, B. Lux, Diamond growth by hot-filament chemical vapor deposition: state of the art, Diam. Relat. Mater. 2 (1993) 1277.

[75] Shinya Ohmagari, Hideaki Yamada, Hitoshi Umezawa, Nobuteru Tsubouchi, Akiyoshi Chayahara, Yoshiaki Mokuno, Growth and characterization of free-standing p+ diamond (100) substrates prepared by hot-filament chemical vapor deposition, Diam. Relat. Mater. 81 (2018) 33-37.

[76] JamesHerlinger,sp3'sexperienceusinghotfilamentCVDreactorstogrowdiamond for an expanding set of applications, Thin Solid Films 501 (2006) 65-69.

[77] L.F. Berzak Hopkins, N.B. Meezan, S. Le Pape, L. Divol, A.J. Mackinnon, D.D. Ho, M. Hohenberger, O.S. Jones, G. Kyrala, J.L. Milovich, A. Pak, J.E. Ralph, J.S. Ross, L.R. Benedetti, J. Biener, R. Bionta, E. Bond, D. Bradley, J. Caggiano, D. Callahan, C. Cerjan, J. Church, D. Clark, T. Doppner, R. Dylla-Spears, M. Eckart, D. Edgell, J. Field, D.N. Fittinghoff, M. Gatu Johnson, G. Grim, N. Guler, S. Haan, A. Hamza, E.P. Hartouni, R. Hatarik, H.W. Herrmann, D. Hinkel, D. Hoover, H. Huang, N. Izumi, S. Khan, B. Kozioziemski, J. Kroll, T. Ma, A. MacPhee, J. McNaney, F. Merrill, J. Moody, A. Nikroo, P. Patel, H.F. Robey, J.R. Rygg, J. Sater, D. Sayre, M. Schneider, S. Sepke, M. Stadermann, W. Stoeffl, C. Thomas, R.P.J. Town,

P.L. Volegov, C. Wild, C. Wilde, E. Woerner, C. Yeamans, B. Yoxall, J. Kilkenny, O.L. Landen, W. Hsing, M.J. Edwards, First high-convergence cryogenic implosion in a near-vacuum hohlraum, Phys. Rev. Lett. 114 (2015) 175001.

[78] R. Ishizaki and K. Nishihara, Phys. Rev. Lett. 78, 1920 (1997).

[79] S. E. Bodner, Phys. Rev. Lett. 33, 761 (1974).

[80] Andrew N. Mostovych, Denis G. Colombant, Max Karasik, James P. Knauer, Andrew J. Schmitt, and James L. Weaver, Phys. Rev. Lett. 100, 075002 (2008).

[81] S. X. Hu, G. Fiksel, V. N. Goncharov, S. Skupsky, D. D. Meyerhofer, and V. A. Smalyuk, Phys. Rev. Lett. 108, 195003 (2012).

[82] J. S. Ross, D. Ho, J. Milovich, T. Doppner, J. McNaney, A. G. MacPhee, A. Hamza, J. Biener, H. F. Robey, E. L. Dewald, R. Tommasini, L. Divol, S. Le Pape, L. Berzak Hopkins, P. M. Celliers, O. Landen, N. B. Meezan, and A. J. Mackinnon, Phys. Rev. E 91, 021101 (2015).

[83] N. B. Meezan, L. F. Berzak Hopkins, S. Le Pape, L. Divol, A. J. MacKinnon, T. Doppner, D. D. Ho, O. S. Jones, S. F. Khan, T. Ma, J. L. Milovich, A. E. Pak, J. S. Ross, C. A. Thomas, L. R. Benedetti, D. K. Bradley, P. M. Celliers, D. S. Clark, J. E. Field, S. W. Haan, N. Izumi, G. A. Kyrala, J. D. Moody, P. K. Patel, J. E. Ralph, J.R. Rygg, S. M. Sepke, B. K. Spears, R. Tommasini, R. P. J. Town, J. Biener, R. M. Bionta, E. J. Bond, J. A. Caggiano, M. J. Eckart, M. Gatu Johnson, G. P. Grim, A. V. Hamza, E. P. Hartouni, R. Hatarik, D. E. Hoover, J. D. Kilkenny, B. J. Kozioziemski, J. J. Kroll, J. M. McNaney, A. Nikroo, D. B. Sayre, M. Stadermann, C. Wild, B. E. Yoxall, O. L. Landen, W. W. Hsing, and M. J. Edwards, Phys. Plasmas 22, 062703 (2015).

[84] L. F. Berzak Hopkins, N. B. Meezan, S. Le Pape, L. Divol, A. J. Mackinnon, D. D. Ho, M. Hohenberger, O. S. Jones, G. Kyrala, J. L. Milovich, A. Pak,

J. E. Ralph, J. S. Ross, L. R. Benedetti, J. Biener, R. Bionta, E. Bond, D. Bradley, J. Caggiano, D. Callahan, C. Cerjan, J. Church, D. Clark, T. Doppner, R. Dylla-Spears, M. Eckart, D. Edgell, J. Field, D. N. Fittinghoff, M. Gatu Johnson, G. Grim, N. Guler, S. Haan, A. Hamza, E. P. Hartouni, R. Hatarik, Phys. Rev. Lett. 114, 175001 (2015).

[85] R. E. Olson, R. J. Leeper, J. L. Kline, A. B. Zylstra, S. A. Yi, J. Biener, T. Braun, B. J. Kozioziemski, J. D. Sater, P. A. Bradley, R. R. Peterson, B. M. Haines, L. Yin, L. F. Berzak Hopkins, N. B. Meezan, C. Walters, M. M. Biener, C. Kong, J. W. Crippen, G. A. Kyrala, R. C. Shah, H. W. Herrmann, D. C. Wilson, A. V. Hamza, A. Nikroo, and S. H. Batha, Phys. Rev. Lett. 117, 245001 (2016).

[86] S. Le Pape, L. F. Berzak Hopkins, L. Divol, A. Pak, E. L. Dewald, S. Bhandarkar, L. R. Bennedetti, T. Bunn, J. Biener, J. Crippen, D. Casey, D. Edgell, D. N. Fittinghoff, M. Gatu-Johnson, C. Goyon, S. Haan, R. Hatarik, M. Havre, D. D-M. Ho, N. Izumi, J. Jaquez, S. F. Khan, G. A. Kyrala, T. Ma, A. J. Mackinnon, A. G. MacPhee, B. J. MacGowan, N. B. Meezan, J. Milovich, M. Millot, P. Michel, S. R. Nagel, A. Nikroo, P. Patel, J. Ralph, J. S. Ross, N. G. Rice, D. Strozzi, M. Stadermann, P. Volegov, C. Yeamans, C. Weber, C. Wild, D. Callahan, and O. A. Hurricane, Phys. Rev. Lett. 120, 245003 (2018).

[87] P. M. Celliers, D. J. Erskine, C. M. Sorce, D. G. Braun, O. L. Landen, and G. W. Collins, Rev. Sci. Instrum. 81, 035101 (2010).

[88] O. L. Landen, D. K. Bradley, D. G. Braun, V. A. Smalyuk, D. G. Hicks, P. M. Celliers, S. Prisbrey, R. Page, T. R. Boehly, S. W. Haan, D. H. Munro, R. G. Wallace, A. Nikroo, A. Hamza, J. Biener, C. Wild, E. Woerner, R. E. Olson, G. A. Rochau, M. Knudson, D. C. Wilson, H. F. Robey, G. W. Collins, D. Ho, J. Edwards, M. M. Marinak, B. A. Hammel, D. D. Meyerhofer, and B. J. MacGowan, J. Phys.: Conf. Ser. 112, 022004 (2008).

[89] Field, J. E. The Properties of Natural and Synthetic Diamond. (Academic, London, 1997).

[90] Telling, R. H., Pickard, C. J, Payne, M. C, and Field, J. E., Phys. Rev. Lett. 84, 5160-5163 (2000).

[91] B. Baudrillart, A.S.C. Nave, S. Hamann, F. Benedic, G. Lombardi, J.H. van Helden, J. Ropcke, J. Achard, Growth processes of nanocrystalline diamond films in microwave cavity and distributed antenna array systems: a comparative study, Diam. Relat. Mater. 71 (2017) 53-62.

[92] B. Baudrillart, F. Benedic, Th. Chauveau, A. Bartholomot, J. Achard, Nanocrystalline diamond films grown at very low substrate temperature using a distributed antenna array microwave process: towards polymeric substrate coating, Diam. Relat. Mater. 75 (2017) 44-51.

[93] Sh. Michaelson, Y. Lifshitz, O. Ternyak, R. Akhvlediani, A. Hoffman, Hydrogen incorporation in diamond films, Diam. Relat. Mater. 16 (2007) 845-850.

[94] Xingbo Liang, Lei Wang, Hongliang Zhu, Deren Yang, Effect of pressure on nano- crystalline diamond films deposition by hot filament CVD technique from CH4/H2 gas mixture, Surf. Coat. Technol. 202 (2007) 261-267.

[95] Markus Mohr, Layal Daccache, Sebastian Horvat, Kai Bruhne, Timo Jacob, Hans-Jorg Fecht, Influence of grain boundaries on elasticity and thermal conductivity of nanocrystalline diamond films, Acta Mater. 122 (2017) 92-98.

Appendix A

A.1 Conservation laws on shock wave in solids

The Rankine-Hugoniot equations relate the pre- and post-shock conditions via the particle velocity(U_{p}) and shock velocity (U_{s}) [49]. These relations are derived from the conservation of mass, momentum, and energy across the shock wave discontinuity. The particle velocity describes the fluid velocity, or the velocity of the piston. The fluid state is determined by giving variables of pressure P, density ρ, temperature T, and velocity $\boldsymbol{v}$ as a function of position coordinates $\boldsymbol{x}$ and time t. The conservation laws of mass, momentum, and energy for the fluid element are expressed as follows:

$$\frac{\partial \rho}{\partial t} + \nabla \cdot (\rho \boldsymbol{v}) = 0 \tag{A.1}$$

$$\frac{\partial \rho \boldsymbol{v}}{\partial t} + \nabla \cdot (\rho \boldsymbol{v}\boldsymbol{v}) = -\nabla p \tag{A.2}$$

$$\frac{\partial}{\partial t}\left[\rho\left(\epsilon + \frac{\boldsymbol{v}^2}{2}\right)\right] + \nabla \cdot \rho \boldsymbol{v}\left[\rho\frac{v^2}{2} + \epsilon + \frac{P}{\rho}\right] = -\nabla \boldsymbol{q}, \tag{A.3}$$

where $\boldsymbol{q}$ is the vector describing the conductive heat flux and ϵ is the internal energy per unit mass. Consider that a fluid or solid medium with a steady density ρ_0 and pressure P_0 is one-dimensionally compressed from right to left by the piston (as in Fig. A.1(a)). Piston drives a shock wave starting from the right. In the laboratory reference frame, the shock discontinuity transits the medium with shock velocity, U_{s}, and the fluid velocity behind the shock front, described by the particle

velocity is given by U_{p}.

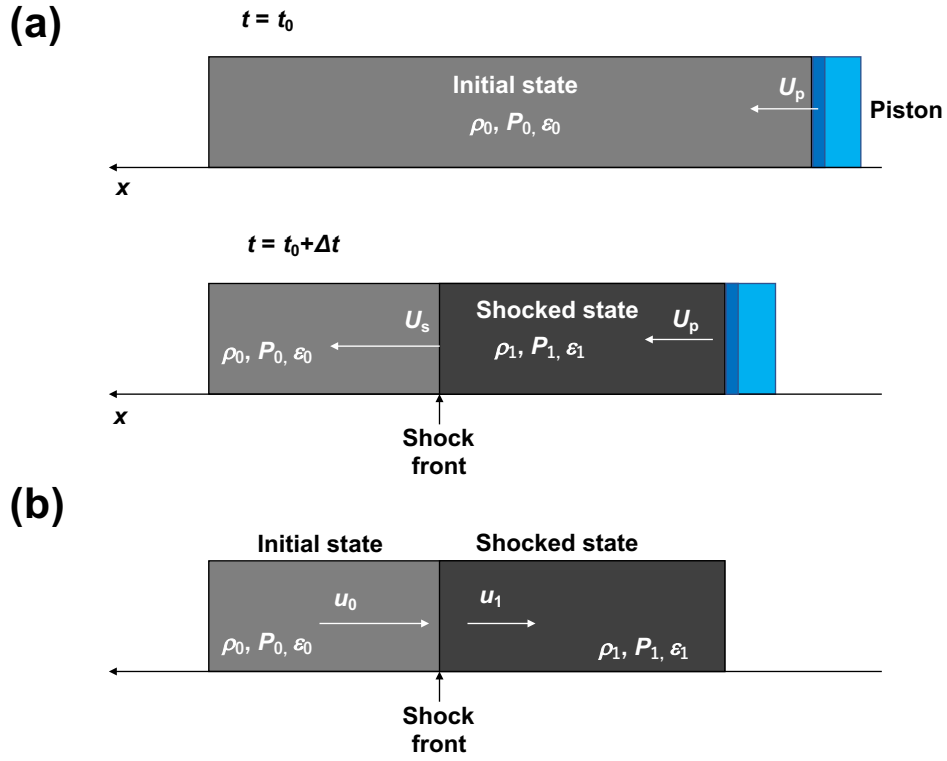

Figure A.1: (a) One dimensional compression by propagating of plane shock wave in the laboratory reference frame. t_0 is initial time. At $t = t_0 + \Delta t$, the shock propagates at the shock velocity U_{s}, while the fluid velocity is represented by u_{p}. (b) In the stationary shock reference frame, the fluid moves into and out of the shock discontinuity at velocity u_0 and u_1.

In a reference frame where the shock is stationary, the shocked medium lies on the right of the shock front, as shown in Fig. A.1(b), and unperturbed medium, with initial density ρ_0, pressure P_0, and mass velocity u_0, lies on the left of the shock front and flows into the shock discontinuity with velocity $u_0 = -U_{\mathrm{s}}$. Assuming steady shock conditions, the shock front is a discontinuity between two states. In the reference frame of the stationary shock, the density does not change with respect to time ($\frac{\partial}{\partial t} = 0$). Let subscripts 0 and 1 describe the unshocked and shocked medium. When these conservation laws, Equations (A.1), (A.2), and (A.3), are integrated in intervals before and after the shock front,

$$\rho_0 u_0 = \rho_1 u_1 \tag{A.4}$$

$$P_1 - P_0 = \rho_0 u_0^2 - \rho u_1^2 \tag{A.5}$$

$$P_0 u_0 - P_1 u_1 = \rho_0 u_0 \left[\left(\epsilon_1 + \frac{u_1^2}{2} \right) - \left(\epsilon_0 + \frac{u_0^2}{2} \right) \right] \tag{A.6}$$

are obtained. Given that U_s is the propagation velocity of the shock front through the unperturbed fluid, $u_0 = -U_\mathrm{s}$. The velocity u_1 of mass leaving the discontinuity (or shock front), can be expressed as $u_1 = -(U_\mathrm{s} - U_\mathrm{p})$. Equations (A.4), (A.5), and (A.6) can be rewritten by using U_p and U_s:

$$\rho_0 U_\mathrm{s} = \rho_1 (U_\mathrm{s} - U_\mathrm{p}) \tag{A.7}$$

$$P_1 - P_0 = \rho_0 U_\mathrm{s} U_\mathrm{p} \tag{A.8}$$

$$\epsilon_1 - \epsilon_0 = \frac{1}{2}(P_0 + P_1)(V_0 - V_1). \tag{A.9}$$

These equations are called Rankin-Hugonio relations. The Rankine-Hugoniot relations result in the Rankine-Hugoniot curve, or shock compression curve, describing the locus of achievable final shock states. Shock compression curves are obtained from the Rankine-Hugoniot relations and knowledge of the equation of state of the material: the relationship between thermodynamic variables such as pressure, density and temperature (as in Section 3.3, Fig. 3.2).